Graduate Theses, Dissertations, and Problem Reports

2003

Design considerations for longwall yield pillar stability

Khaled Morsy Mohamed
West Virginia University

DESIGN CONSIDERATIONS FOR LONGWALL YIELD PILLAR STABILITY

Khaled Morsy Mohamed

Dissertation submitted to the
College of Engineering and Mineral Resources
at West Virginia University
in partial fulfillment of the requirements
for the degree of

Doctor of Philosophy
in
Mining Engineering

S. Peng, Ph.D., Chair
A. Khair, Ph. D.
K. Heasley, Ph. D.
Y. Luo, Ph.D.
Department of Mining Engineering

E. Barbero, Ph.D.
Department of Mechanical and Aerospace Engineering
Morgantown, West Virginia
2003

Keywords: Yield pillar design, ground control, deep mines, coal bumps, finite element
modeling

ABSTRACT

Design Considerations for Longwall Yield Pillar Stability

Khaled Morsy Mohamed

Coal mine bumps have presented serious mining problems in the United States throughout the 20th century. Persistent bump problems not only threaten the safety of miners, but also have caused the abandonment of large coal reserves and have led to premature mine closures. Current application of yield pillars shows that it can prevent coal bumps in some longwall mines. In this dissertation, the need for a new method to design yield pillars in bump prone conditions is established. In order to fulfill this need, a PC-design program based on finite element modeling was developed. This program can design stable yield pillar systems for most of bump prone conditions. The preliminary applications of this program illustrated its ability to evaluate the stability of yield pillars with respect to coal bumps.

To achieve a realistic longwall panel simulation, coal and gob property models were developed. In this study, a yield pillar was divided into three zones; namely core, transition and rib zones. An appropriate stability criterion was assigned for each zone. A number of stability measures were introduced to evaluate the yield pillar stability, namely; yield pillar ratio (YPR), rib zone ratio (RZR), pillar bump index (PBI) and roof-to-floor convergence (C). An interpolation model correlating the pillar stability measures and the geological and geometrical factors was developed. In this study, a yield pillar was designed to yield with acceptable levels of bump index (PBI) and roof-to-floor convergence (C).

Finally, a PC- program to evaluate the longwall yield pillar stability (ELYPS-model), was developed based on the developed interpolation model. The ELYPS-model can be used to design and to evaluate 2-entry yield pillar systems for wide ranges of geological and geometrical factors.

ACKNOWLEDGEMENTS

TABLE OF CONTENTS

Contents   **Pages**

LIST OF TABLES

LIST OF FIGURES

NOMENCLATURES

BI   Bump Index

C   Roof-to-floor Convergence

C_a   Allowable roof-to-floor Convergence

CSF   Core Stability Factor

EBI   Element Bump Index

EIF   Element Stability Factor

ELYPS-model   Evaluation of Longwall Yield pillar Stability model

ESF   Element Stability Factor

LMS   Local Mine Stiffness

PBI   Pillar Bump Index

PBI_a   Allowable Pillar Bump Index

PSF   Pillar Stability Factor

PYR   Pillar Yield Ratio

RIF   Rib Instability Factor

RZR   Rib Zone Ratio

CHAPTER 1

INTRODUCTION

1.1 General

Coal bumps refers to a sudden and violent failure of in situ coal [Holland, 1954]. The intensity of coal bumps ranges from minor thumping of coal pillars to large quantities of coal being suddenly ejected into the mine. Persistent bump problems not only threaten the safety of miners, but also have caused the abandonment of large coal reserves and have led to premature mine closures. Several hypotheses have been introduced to explain the mechanism of coal bumps; e.g. pressure bumps theory and shock bumps theory [Rice, 1934]. The factors that promote coal bumps have been investigated by many researchers [Babcok, 1984, DeMarco, 1995, Maleki, 1995]. These factors cab be classified into two groups: factors related to the natural conditions, and factors related to the gateroad design.

Several techniques, such as yield pillars, were developed to reduce the occurrence of coal bumps. Current practice of yield pillar application shows that it can prevent coal bumps in some longwall mines and safe significant amounts of coal reserves for deep mines. To deal with these problems, yield pillar design was adopted in the western coal mines in the 1960's, e.g. Sunnyside Mine [Iannacchione, 1995]. The yield pillar design allows the gateroad system to deform under the weight of the approaching panel abutment thereby diverting substantial amount of load to the nearby solid coal. Although many definitions have been proposed, there is no standard one for the yield pillar design [Gauna 1985, Mark, 1990, Tadolini, 1992, Pen, 1994, DeMarco, 1994]. The common definition for the yield pillar is that one which is designed to yield at the development load.

The current practice of yield pillar sizing is based upon two principles:

1. Theoretical- based upon analytical or numerical methods. Carr and Wilson's method [1982] is the first analytical method for yield pillar design. Chen's method [1989] for yield pillar design is a combination of numerical modeling and the Wilson's confined core concept [Wilson, 1977]. Tsang's method [1992] for the yield pillar design consists of a number of regression equations. These regression equations were developed by combining the results of numerical modeling with fractional factorial experiment design.

2. Historical – experience gained by trial and error.

1.2 Statement of the Problem

Yield pillar design has been used in US longwall coal mines to prevent coal bumps and floor heave. As promising as yield pillar-based gateroads appear to be, the acceptance of this design option continues to be hindered by the somewhat frequent occurrence and severity of failed applications, coupled with the lack of a proven design methodology that quantifies the performance potential of the entire yielding gateroad system [Mark, 1988].

When compared with conventional stiff pillar design, the yield pillar design is more complicated and involved. This in part is due to consideration of the post-peak properties of coal and complex interactions with roof and floor. Because of this, there are no available analytical models that can fully describe the behavior of yield pillar. However, numerical methods such as the finite element method can provide acceptance solutions to problems of this kind. The success of numerical methods to a large extent depends on the reliability of their material models and the simulation procedure adopted.

The available general purpose finite element codes, e.g. ABAQUS, when used to design yield pillars pose special problems. The built-in material models in those codes can not accurately model the post-peak behavior of coal pillar or the load-deformation characteristics of gob, which are vital for yield pillar design. Therefore, one of the

important objectives of this work is to develop realistic procedures that can overcome these problems. This can be achieved by adapting the available material models to match the laboratory and field observations.

The theoretical yield pillar design methods for longwall mining described before do not adequately address the pillar behavior in the post-peak region though most of sudden pillar failures, i.e. coal bumps, in this region. Hence, another objective of this work is to comprehensively investigate and develop the design parameters that can describe the pillar behavior in the post-peak region and provide guidelines to estimate the pillar stability or instability. Finally, a user friendly PC-based program which can design stable yield pillar systems for most common geological and geometrical conditions would be extremely useful.

1.3 Scope of Work

The objectives of this work are as follows:

- Development of a realistic numerical simulation procedure for longwall workings.

- Development of a method to evaluate yield pillar stability with regard to coal bumps.

- Development of a PC-program to design gateroads that employ yield pillars.

A comprehensive literature review was carried out in this research. This review covered different aspects of coal bump phenomenon and yield pillar design methods. Following the literature review, a rational simulation for longwall panel was established. By adopting the available modeling capabilities of ABAQUS program, new material property models for coal and gob were developed.

A critical review for yield pillar design methods was conducted. This review illustrated the need for a new yield pillar design method that can evaluate the stability of yield pillars in the post-peak region. Unless the post-peak behavior of the yield pillars is included in the pillar design process, the risks of coal bumps still possible.

A new method for evaluating the stability of yield pillars was proposed. The key issue of the newly developed method, it considered the non-uniform stress distribution of yield pillars by dividing the yield pillar into three zones; namely core, transition and rib zones. Clear definitions of these zones were provided. An appropriate stability criterion was assigned for each zone. A case study of unsuccessful yield pillar design associated with coal bumps and another case of stable design were used to assess the proposed method. The proposed method was able to evaluate the stability of yield pillar systems in both designs.

The development of a method for yield pillar design was achieved in the following steps:

1. Performing a screening analysis for the effects of geological and geometrical factors on the yield pillar stability.

2. Development of interpolation model for the pillar stability measures based on a full factorial analysis for the most important factors. These stability measures are defined as: yield pillar ratio (YPR), rib zone ratio (RZR), pillar bump index (PBI) and roof-to-floor convergence (C).

3. In this study, a yield pillar was designed to yield with acceptable levels of pillar bump index (PBI) and roof-to-floor convergence (C).

4. A windows-based computer program, ELYPS-model, was established based on a proposed design algorithm and a developed interpolation model. The ELYPS-model was used to evaluate three cases of stable yield and unstable pillar designs. Based on these evaluations, preliminary threshold values for the allowable pillar bump index and roof-to-floor convergence, 4 and 3-inches, respectively, were proposed.

CHAPTER 2

LITERATURE REVIEW

Longwall mining is one of the principal underground coal mining methods in the United States. Although basic longwall mining techniques were developed in England in the 17th century, there was little interest in longwall mining in the United States until the 1950's, when new German technology was introduced. As the technology was developed further in the United States, longwall production grew steadily. Productivity is now higher for longwall mining than for other underground production methods, and productivity is expected to keep growing as new technological improvements [DOE/EIA, 1995].

Today's highly competitive coal industry requires that mine operators employ a longwall gateroad design that maintains good ground control and high worker safety standards, and requires less development time. Gateroads are lifelines through which mine workers, supplies, and ventilating air reach the longwall working face, and they are the escape routes needed by miners in case of an emergency. They must remain operational despite the heavy abutment loads resulting from longwall mining. A gateroad blocked by a roof fall, floor heave, or pillar bump constitutes a major safety hazard to miners, as well as a substantial expense for the mine operator.

Coal mine bumps have presented serious mining problems in the United States throughout the 20th century. Fatalities and injuries have resulted when these destructive events occurred at the working faces of the mines. Persistent bump problems not only threaten the safety of miners, but also have caused the abandonment of large coal reserves and have led to premature mine closures.

2.1 Typical Longwall Layout

In longwall mines, two sets of entries called "gateroads", one on each side of the coal panel to be mined, are driven from the main mine entries to the end of the panel They are then connected at the back of the panel by another set of entries (Figures 2-1) [Peng, 1986]. The entries that are used to transport miners, coal, and supplies are called the "headgate" entries. On the opposite side of the panel, there are "tailgate" entries that are used mainly as an airway in ventilating the mine. Due to the parallel layout of longwall panels, the headgate entries become the tailgate entries of the next panel to be mined. The entries at the back of the panel, where extraction begins, are called the "bleeder entries" that provide continuity in the mine ventilation system. The unmined parts of the coalbed that are left within the gateroad entries are called "pillars". After the longwall panel has been blocked out by entries, it is mined on "retreat."
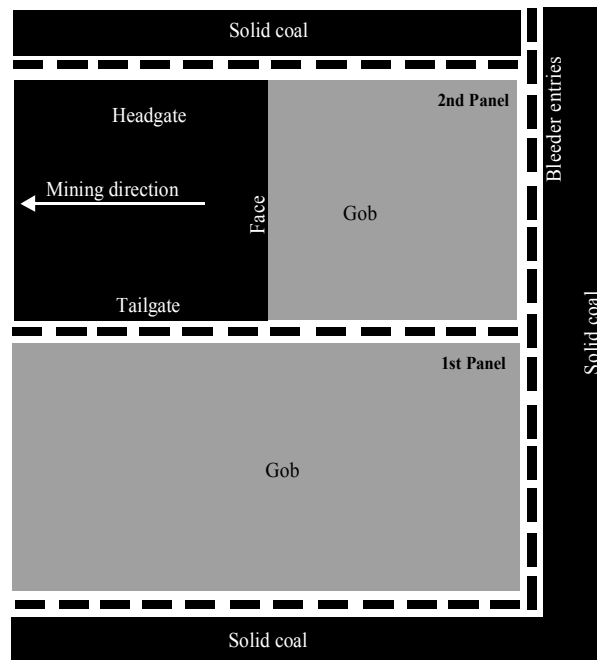
Figure 2-1 Typical longwall retreating panel layout employing 2-entry gateroad system

Two basic approaches are available to guide longwall pillar design. A conventional, or stiff, pillar design is based on the strength of materials approach and has the objective of maintaining pillar loads less than pillar strength. In contrast, the yield pillar is designed to deform progressively during its service life, thereby transferring its load to adjacent stiffer pillars or abutment and controlling the stress distribution around the openings. In fact, the failure of yield pillar design to provide adequate ground control performance is primarily due to a lack of a proven design methodology that quantifies the performance potential of the entire yielding gateroad system [Koehler, 1995].

2.2 Coal Bumps

The general tem "coal mine bump" refers to the sudden and violent failure of in situ coal. A number of terms are often used interchangeably to describe the coal mine bumps, or simply coal bumps: burst, rock burst, bounce, pillar burst and pressure burst [Holland, 1954].

Coal bumps can be characterized as the unstable release of energy associated with the post-peak stage of pillar loading that occurs with the progression of mining. Unstable releases of energy occur when the coal is able to absorb less energy than is released by the surrounding rock mass during the failure process. At any stage of mining, the mining geometry, the overburden stress, the elastic properties of rock mass, and stress-strain characteristics of the seam material govern the amount of excess energy so released [Crouch, 1973].

The intensity of coal bumps ranges from minor thumping of coal pillars to large quantities of coal being suddenly ejected into the mine workings where men and machinery are present. MSHA statistics from 1970 through 1996 shows that a significant decrease in the number of fatalities related to coal bumps (Figure 2-2), but the injuries rates still high for the same interval, Figure 2-3. It is anticipated that as the easily recoverable reserves are depleting, the trend will be toward deeper mines and those in less stable geological settings. Therefore more coal bumps are likely to occur in the

future and practical and economical methods of controlling or preventing coal bumps must be available to insure miner's safety [Maleki, 1999].

Fatalities distribution
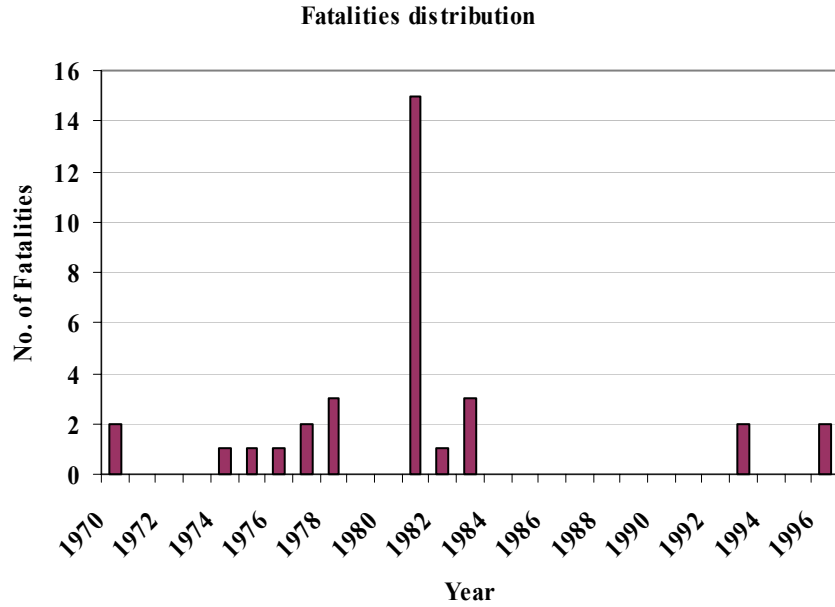
Figure 2-2 Coal bumps fatalities distribution

Injuries distribution
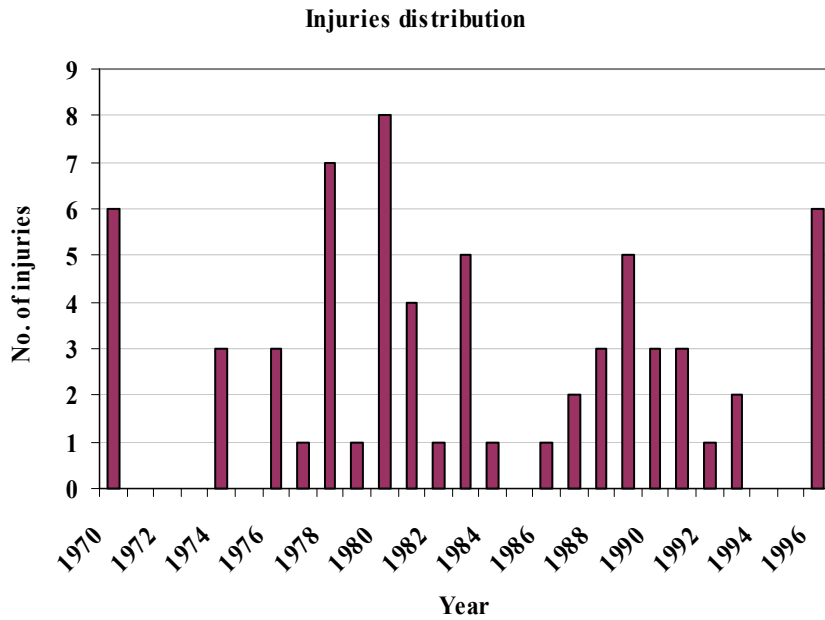
Figure 2-3 Coal bumps injuries distribution

2.2.1 Parameters Affecting Coal Bumps

Several hypotheses have been introduced to explain the mechanism of coal bumps. Usually these hypotheses were proposed to fit particular conditions. According to Rice [1934] coal bump can be classified as either "pressure bumps" or "shock bumps". A pressure bump is due to the violent failure of a pillar when its maximum load-bearing capacity is reached. A shock bump is due to the breakage of a thick, rigid stratum at a considerable distance above the coal seam causing a great hammer-like blow to the immediate roof, resulting in a shock wave being transmitted to the coal pillars.

The essential difference between the two types of coal bumps is a matter of loading rate: it is quasi-static in the case of a pressure bump as opposed to dynamic for a shock bump. In practice, it is difficult to determine which type of coal bump has occurred. Most investigators explain the coal bump mechanism as more closely related to a pressure bump rather than a shock bump.

Coal bumps can be attributed to several factors that may act independently or jointly to cause bumps. Generally these factors can be classified into two groups: factors related to the natural conditions, and factors related to the gateroad design.

♦ **Natural conditions promoting coal bumps** – These conditions can be summarized in the followings:

1. *High mining depth* - in most bump cases, the onset of bump problems occurred around a depth of 1500 ft or more but in some cases bumps occurred at depths as shallow as 750 ft [DeMarco, 1995].

2. *Strong overlying rock* stratum within a distance of 10 to 15 times the thickness of the coal seam [Rice, 1934]. One of the leading contributors to coal bumps in many cases is the massive sandstone unit that commonly makes up the main roof. This roof is able to span the gobs of several panels before they fail and reach a state of maximum subsidence

[DeMarco, 1995]. The sudden failure of these units is also a contributing factor in the initiation of coal bumps [Maleki, 1995].

3. *A strong floor* that is not subjected to heaving.

4. *A structurally strong coal* – several researchers believed that strong, brittle coal with a high compressive strength was necessary for bumps. However, Babcock analyzed this concept in the laboratory and concluded that coal bumps could occur regardless of the strength of coal [Babcok, 1984]. He hypothesized that pillar bumps are caused by the sudden release of end constraint at the roof and floor.

5. *Sandstone channels in immediate roof* – sandstone channels are stress-concentrating structures that are directly related to bumping along longwall panels. The massive nature of these units is the major factor affecting bump initiation.

♦ **Unsuccessful Gateroad Design promoting coal bumps** – It is believed that the use of pillars with width-to-height ratios of 4 to 5 can promote bumps. Based on a linear relationship between the pillar width-to-height ratio and its post-peak stiffness, Ozbay [1989] concluded that a pillar with width-to-height ratio grater than 5 could not bump because its post-peak stiffness should be zero or above. However, it has been reported that even the pillars with width-to-height ratios greater than 8 have experienced bump failures [Babcock, 1984 and Campoli, 1990]. To explain the failure of yield pillar system to provide an adequate ground control, the critical pillar concept has been introduced. A "critical pillar" is simply defined as one that is too large to yield either nonviolently or to yield before the roof and floor sustain permanent damages and is too small to support the full abutment loads [DeMarco, 1996]. The relationship between critical-pillar designs, and yield and abutment pillar design is presented in Figure 2-4. The horizontal axis represents the minimum performance separating stable from unstable gateroad configurations. A pillar design whose performance falls above the

horizontal axis is considered successful (stable), while a design whose performance falls below the horizontal axis is considered unsuccessful (unstable). An important aspect of the critical pillar concept is the abrupt transition between the fully successful yielding gateroad and the worst possible critical pillar conditions.

Figure 2-4 is a useful graphic representation of the critical pillar concept; however, it should not be used to suggest that pillar width alone can completely determine whether a pillar design falls in the critical range. Other mining parameters, such as the overburden depth, and the geo-mechanical properties of the roof and floor strata, can have profound effects on the final disposition of a specific geometry. In practice in order to determine the width of critical pillar, a tapering pillar experiment has to be conducted [Serata, 1985].
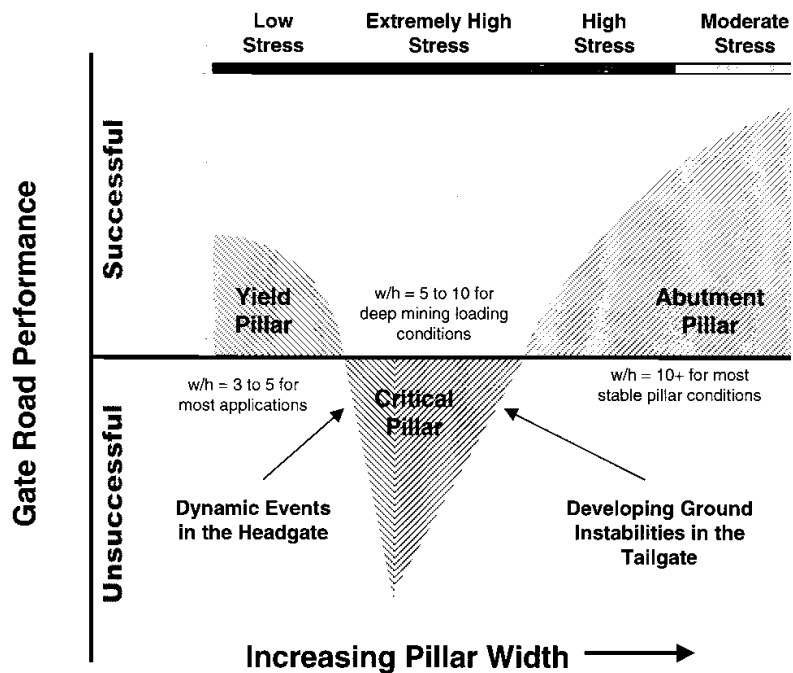
Figure 2-4 Conceptual diagram of the critical pillar [DeMarco, 1996]

2.2.2 Coal Bumps Detection Methods

Many attempts have been made to detect coal bumps ahead of mining. A summary of some of these detection methods will be presented.

♦ **Micro-gravity Method** [Haramy, 1985] - the micro-gravity method uses the changes in density distribution of rock mass due to mining activity to predict coal bumps. An increase in volume and a decrease in rock density cause a negative gravity anomaly. Coal bumps could be predicted depending on the recorded sign of the gravity anomaly; a negative gravity anomaly occurs shortly before a bump, while a positive gravity anomaly indicate bump is not likely to occur.

♦ **Micro-seismic Method** [Haramy, 1985] - the micro-seismic method, also known as Acoustic Emissions (AE) method, is a geophysical approach that detects sub-audible rock noise associated with rock yielding. Geophones translate the rock noises to electric analog signals. As the rock approaches failure, the AE noise count increases rapidly. If the geophone average noise count exceeds a threshold level, bump is likely to occur.

♦ **Shield Monitoring Technique** [Cox, 1995] – this technique depends on the GCMS developed by the U.S. Bureau of Mines. The computerized GCMS can be used to monitor shield-loading behavior. The correlation between variations in shield pressure and ground failure offers mining engineers the first real possibility of developing a real-time alarm system to anticipate impending ground failures associated with high-speed mechanized longwall mining system.

2.2.3 Control of Coal Bumps

Coal bump prevention can be achieved through two courses of action. The most desirable means is mine design and planning. The other option is to initiate an active stress relief program incorporated into the mining cycle.

♦ **Stress Relief (De-stressing)** – The objective of stress relief is to destroy the structure integrity of the coal so that it cannot store enough energy to bump. Several methods of de-stressing have been used in the US coal mines. A brief summary of some of these methods will be given.

1. **Shot Firing** [Innacchione, 1995] - shot firing fractures coal, thereby extending the yielded coal zone. This process injects energy into stressed coal, causing seismic shock. The shock waves temporarily release confinement, initiating violent failure under a controlled condition.

2. **Auger Drilling** [Varley, 1986] – this method is used successfully in Europe but proved unreliable and time consuming in the US coal mines. In this method, the stress is relieved through drilling large diameter, 100 mm, holes into the critical zone. By drilling into the critical zone, fracturing and stress relief are achieved by removing large amounts of coal, creating a weakened zone around the drill stem and initiating bumps.

3. **Water Infusion**– Water lubricates fracture surfaces within rock mass; therefore, water infused into coalbed can initiate slippage between rock surfaces, thus lowering the state of confinement on the surface and amount of energy stored within the rock [Iannacchione, 1995]. In this method, several 100 ft long holes are drilled on approximately 75ft centers along the tailgate road. Hydraulic hoses are inserted in those holes and pressured to about 4000 psi; small to moderate bumping occurs [Varley, 1986]. The disadvantage of using this method is floor heave problems.

♦ **Yielding Design**- Yield pillar designs allow the gateroad system to deform under the weight of the approaching panel abutment, thereby diverting substantial load to the nearby solid coal panel. This method of stress control for gateroads was applied in western coal mines in the 1960's in Sunnyside Mine in Utah Basin [Innacchione, 1995]. Not all mines have experienced Sunnyside's success with a yield pillar design. A nearby mine attempting to emulate this very profitable

design had difficulties in developing small pillars without generating serious bumps and routinely lost significant portions of tailgate entries to large bumps. It soon became evident that the successful application of yielding designs depends on the geology surrounding the pillar system.

2.2.4   Coal bump prediction

Natural coal's ability to store and rapidly release elastic strain energy seams to be a fundamental condition for the occurrence of coal bumps in deep underground coal mines [Kidybinski, 1981]. Coal bump indices and the local mine stiffness criterion are used to predict the risk of coal bump.

2.2.4.1 Coal bump index

Several bump indices have been proposed and their numerical values have to be determined by experiment. Three of these indices are most popular, namely the strain storage index (W_{ET}), the bursting efficiency ratio (η), and the rheologic ratio (θ). The first is defined as the proportion of strain energy retained to that dissipated during a single loading-unloading cycle of uniaxial compression. The second is the ratio of the kinetic energy of chips thrown out on failure to the maximum elastic strain energy. The rheologic ratio is calculated as a dynamic resistance stress rate (failure velocity) divided by an average stress relaxation rate.

The Strain Energy Storage Index, W_{ET}, is the simplest coal bump liability indicator. It assumed that the kinetic energy released rapidly during a coal bump is proportional to the elastic strain energy accumulated in a unit volume of coal. The dimensionless value of this index is calculated as

$$W_{ET} = \frac{We}{Wp} \qquad\qquad \textbf{Equation 2-1}$$

where W_e is the stored elastic strain energy; and W_p is the dissipated strain energy.

To estimate the strain energy storage index for any coal seam, the stored elastic strain energy and dissipated strain energy are determined from elastic hysteresis loop parameters found in uniaxial compression loading and unloading tests performed on cubic coal specimens, Figure 2-5. W_{ET} values less than 2 are considered characteristics of nonbursting coal and values over 5 of highly bump-prone coal [Brauner, 1994].
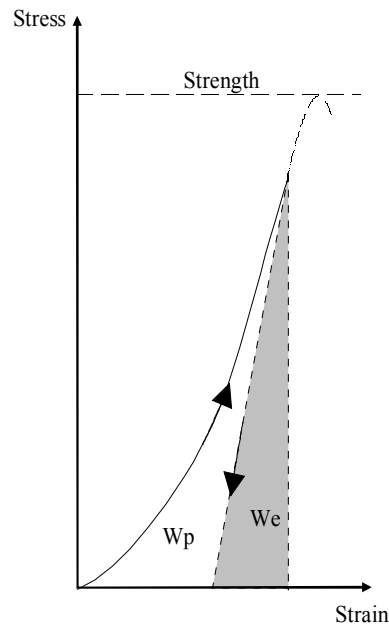
Figure 2-5 Determination of the strain energy storage index

2.2.4.2 Local mine stiffness criterion

The local mine stiffness criterion is able to evaluate stability of yielded parts of the pillar. A simple explanation of the local mine stiffness criterion can be provided by understanding the mechanism of crushing a rock specimen in a compression testing machine, Figure 2-6. Over the region AB in which the load is increasing, the machine-specimen system is "unconditionally stable" [Salamon, 1974] where the applied load is increasing with increasing deformation. Energy is being stored in the machine (i.e., in the frame, pressurizing fluid, hoses, etc.) and in the rock specimen.

In the unloading region BD, the system is "conditionally stable" where the unloading paths for the rock specimen and the machine are independent. A machine with a loading characteristic BC' will release more energy (shaded area BCC') than the rock can absorb by quasi-static deformation for a given strain ε_C beyond the peak value ε_B. The excess energy (area BCC') will be transformed into kinetic energy, i.e., accelerating the rock to violent disintegration. The combination of soft machine characteristic BC', and the specimen characteristic BD, results in unstable violent post-peak deformation.
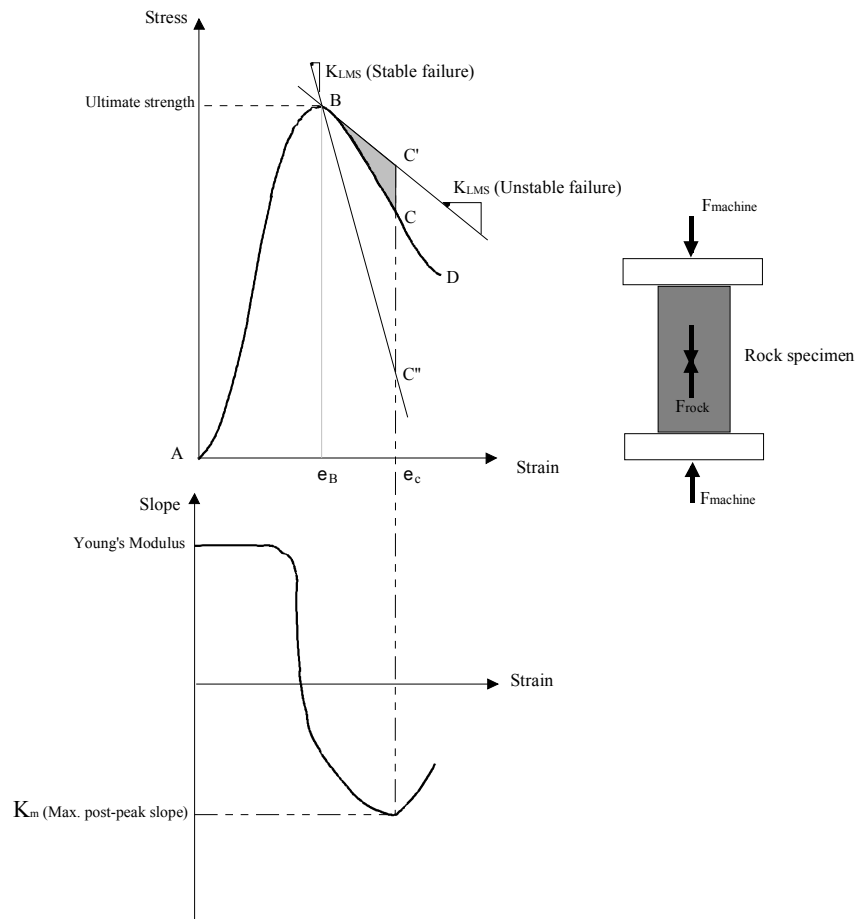
Figure 2-6 Criterion for stable and unstable failure for laboratory specimen

Conversely a "stiffer" machine with unloading characteristic BC'', the machine-specimen system will be stable, since energy must be continuously added from an external source, i.e. increased pump pressure, in order to supply the deficiency between

the energy required for quasi-static deformation along BC, and the characteristic BC''.
The energy deficiency at strain ε_C is represented by the area BCC''.

The mathematical relationship for stable specimen failure is

$$k + \lambda > 0 \qquad\qquad\qquad \textbf{Equation 2-2}$$

where k is the stiffness of the loading machine, which will always be positive; and λ is the gradient of the stress-strain curve of the specimen.

Based on the analogy between laboratory test specimens and mine pillars, Salamon [1974] developed a criterion to predict controlled or uncontrolled collapse of mine pillars. Controlled collapse is defined as the process of pillar failure, which proceeds gradually. On the other hand, uncontrolled collapse is the result of instability and takes place suddenly with or without prior deterioration of the pillars.

Uncontrolled, violent failure occurs when

$$\frac{|K_p|}{|K_{LMS}|} \geq 1 \qquad\qquad\qquad \textbf{Equation 2-3}$$

and controlled, nonviolent failure occurs when

$$\frac{|K_p|}{|K_{LMS}|} < 1 \qquad\qquad\qquad \textbf{Equation 2-4}$$

where $|K_{LMS}|$ is the absolute value of the local mine stiffness; and $|K_p|$ is the absolute value of pillar post-peak stiffness.

2.3 Application of Yield Pillars in U.S. Coal Mines

Tadolini [1992] defined the yield pillar as a pillar that yields or fails upon isolation from the coal seam during the longwall development stage. Mark [1990] recommended that the yield pillars should be designed to yield at the development load. Pen [1994] defined the yielding pillar as a pillar that yields completely before the

maximum load arrives. DeMarco [1994] recommended that the timing of pillar yielding should be designed according to the immediate rock quality. Gauna [1985] defined a yield pillar as one which yields upon isolation from coal seam; i.e. during development.

Yield pillar design has been used in US longwall coal mines to prevent coal bumps and floor heave. As promising as yield pillar-based gateroads appear to be, the acceptance of this design option continues to be hindered by the somewhat frequent occurrence and severity of failed applications, coupled with a lack of a proven design methodology that quantifies the performance potential of the entire yielding gateroad system [Mark, 1988].

Different yield pillar deigns have been tried in US coal mines. These trials include 2-entry, 3-entry, 4-entry, and 5-entry system as shown in Figure (2-7). Western longwall mines have used two-entry yielding pillar systems extensively. Many eastern mines must use multiple-entry gateroads because of high methane inflows [Ray, 1987]. When the number of entries in a yielding pillar system is increased to four, or more, ground conditions can get worse [Martin, 1988]. Table 2-1 shows some of the Western coal mines that have adopted 2-entry yield pillar systems. The majority of these mines have a strong roof and floor. A 30 ft wide pillar was used extensively in these mines irrespective of the mining depth. Some of the cases were successfully eliminated pillar bumps. A wide range of overburden depth (1000 ft - 2800 ft) was used. The pillar length is determined mainly by mining operation. The longer the pillars the less of cross-cuts required, meanwhile ventilation requirements limit the length of the pillars. Hence; a narrow range of pillar lengths was used (80 ft – 105 ft). Also, a narrow range of pillar height was observed (6.5 ft – 9.84 ft).

A comparative study between three different pillar designs, three-entry Yield-Stiff, four-entry Yield-Yield-Stiff, and five-entry all Yield has been conducted in a 1200 ft long experimental headgate section [Mark, 1988]. It was concluded that the five-entry yield design apparently was more successful than the four-entry Y-Y-S and three-entry Y-S designs in protecting the future tailgate entry. Another field study was conducted in JWR No. 4 mine [Gauna, 1985]. This study concluded that a 4-entry system utilizing

yield pillars in conjunction with an adequate design abutment pillar significantly improved roadway conditions when compared to equal-sized pillars. At a southwestern PA coal mine the application of three-entry Y-S and four-entry Y-S-Y designs were successful in reducing roof cutters in longwall development sections [Mucho, 1968].

2- Entry Yield-design

3- Entry Yield-Stiff design

(YS)

4- Entry Yield-Yield-Stiff design

(YYS)

5- Entry all Yield design
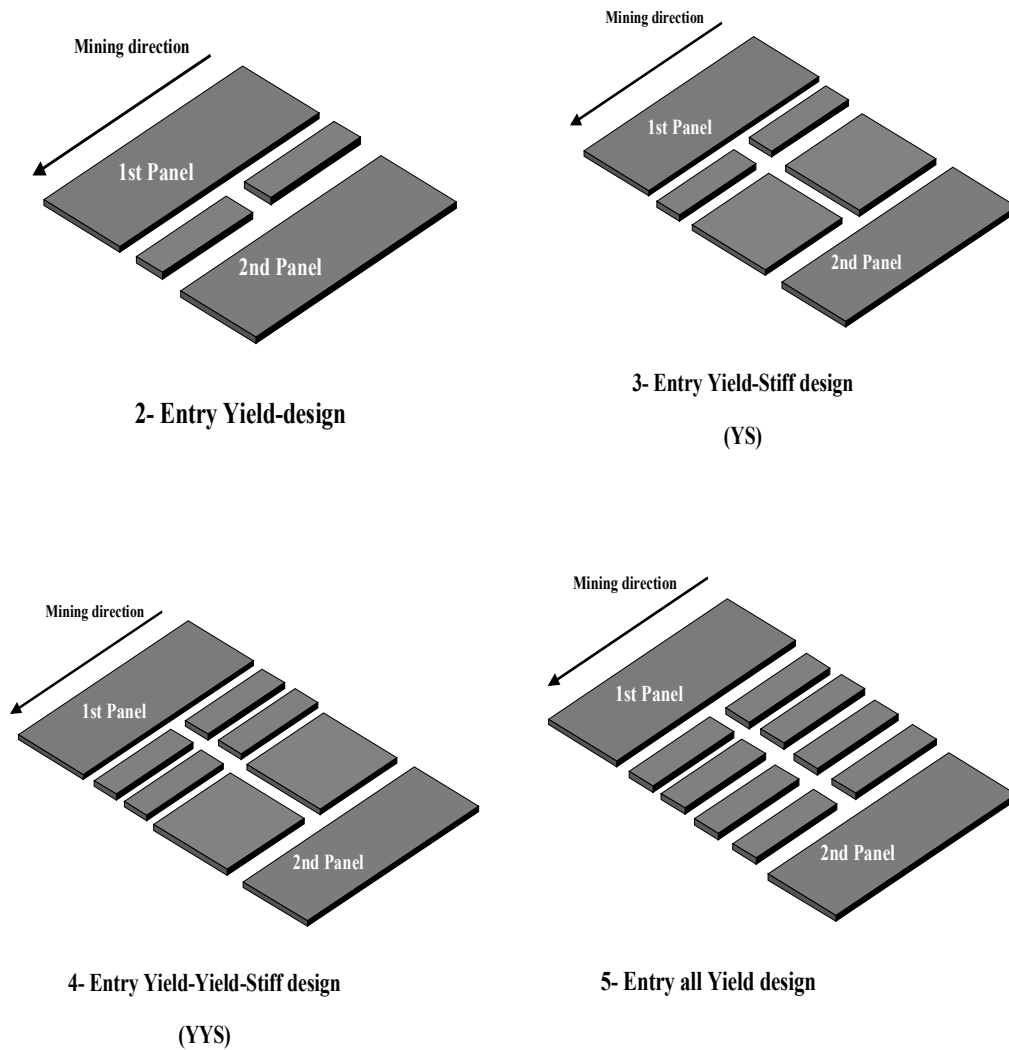
Figure 2-7 Yield pillar design layouts

Table 2-1 Two-entry yield pillar gateroad system

Mine Name and Location	Mining Depth, ft	Pillar Width, ft	Pillar Length, ft	Mining Height, ft	Ground Condition	Comments	Reference
Grandall Canyon Mine Genwall Resources, Inc, UT	2000	29	100	8 - 8.5	Strong roof & floor	No pillar bumping	
Cottonwood Mine Energy West Mining, UT	1600-2000	30	80	6.5 - 9.5	Strong roof & floor	No pillar bumping	
West Ridge Mine Genwall Resources, Inc, UT	1000 - 2200	30	100	6.5 - 9	Strong roof & floor	No pillar bumping	
Willow Creek Mine RAG American Coal Co., UT	1700	26	85	9.84	Weak roof & strong floor	No pillar bumping	
Castle Gate No. 3 Amax Coal Company,UT	1180	30		7	Strong roof	Critical pillar	DeMarco, 1994
Startpoint No. 2 mine Cyprus Plateau Corp., UT	1500	30	85	8	Moderate roof	No pillar bumping	Koehler 1988
Sunnyside No.1 mine Sunnyside Coal Comp., East, UT	2800	35	105	7	Strong roof	No pillar bumping	DeMarco, 1995
Sunnyside No.1 mine Sunnyside Coal Comp., East, UT	2500	55	105	7	Strong roof	HG pillar bumping	DeMarco, 1995
Sunnyside No.1 mine Sunnyside Coal Comp., East, UT	1900	40	105	7	Strong roof	No pillar bumping	Koehler, 1995
Wilberg Mine Utah Power & Light Comp., UT	1600	30		7	Strong roof	TG closure	DeMarco, 1994
Wilberg Mine Utah Power & Light Comp., UT	1600	30		7	Weak roof	TG pillar bumping	DeMarco, 1994

TG = Tailgate,
HG = Headgate

2.4 Effects of Geological and Geometrical Conditions on Yield Pillar

The stress distributions in the yield pillars and around longwall panels are often so complex that the application of yield pillars becomes rather limited without a full understanding of the characteristics of the interaction of surrounding strata and coal. The geometrical and geological factors that could affect the behavior of the longwall structure will be discussed in this section.

2.4.1 Mechanical Properties of Coal Seam

♦ **Uniaxial Compressive Strength-** The in-situ coal strength is defined as the strength of a full-scale cube of coal measuring 36 in on a side, [Hustrulid, 1976]. In-situ coal strength is generally much lower than the compressive strength of a laboratory-scale specimen of the same coal. Mark [1990] has found that meaningful results can usually be achieved for coal pillar strength if an average value of the in-situ strength, taken as 900 psi, is used. Several researchers believed that strong, brittle coal with a high compressive strength was necessary for bumps, [Holland, 1941]. However, Babcock [1984] analyzed this concept in laboratory and concluded that coal bumps could occur regardless of the strength of coal.

♦ **Poisson's ratio -** The rock mechanics database collected by the mining engineering department at West Virginia University for different coal seams shows an average Poisson's ratio of 0.228 ± 0.093, [Tsang, 1992]. Chen [1989] investigated the effect of Poisson's ratio on the stress distribution in yield pillars. He concluded that the stress distribution in the yield zone of coal pillars was significantly influenced by Poisson's ratio. Tsang [1992] found that the effect of Poisson's ratio was insignificant on the stress distribution in the pillar.

♦ **Angle of internal friction-** The rock mechanics database collected by the mining engineering department at West Virginia University for different coal seams shows an average angle of internal friction of $29.6^{o} \pm 7.7^{o}$, Tsang [1992]. The angle of internal friction is an important factor in determining the stress distribution in the yield pillar. The range of angle of internal friction investigated by Tsang [1992] was 17° to 33°. A higher value of angle of internal of friction, 33.7^{o} to 40°, was studied by Chen [1989].

♦ **Time-dependent (Creep) property-** Chen [1997] simulated the viscoplastic pillar deformation in potash mine implementing yield pillar systems. The creep properties of potash were assigned for the pillars in a 2D FEM study. It was found

that the vertical stress at most locations near the openings are stabilized with time or continued to decrease, while the stress continued to increase in the interior abutments. This signifies the progressive extension of yielding, and de-stressing around the openings and gradual transfer of load from yield pillar to the surrounding rock. Tsang [1992] found that the effect of coal creep was insignificant on the stress distribution within the pillar. The literature on mechanical characterization of coal offers only scattered information on creep properties. The available test results refer in all cases to one particular coal type, without any attempts to generalization or systematization, [Ko, 1978].

2.4.2   Mechanical Properties of Coal-Measure Rocks

♦ **Strength and Young's Modulus-** Based on uniaxial compressive testing data collected from 12 mines (Figure 2-8), Maleki [1995] indicated that the ratios of roof/floor strength-to-coal strength and Young's modulus are not enough to assess coal bumps. Although most coal bumps have occurred in mines where roof/coal Young's modulus ratio was greater than 8 and the roof/coal strength ratio was greater than 4, there are severe coal bumps occurred where Young's modulus and strength ratio as low as 5 and 3, respectively. One of the leading contributors to coal bumps in many cases is the massive sandstone unit that commonly makes up the main roof. This roof is able to span the gobs of several panels before they fail and reach a state of maximum subsidence. The sudden failure of these units is also a contributing factor in the initiation of coal bumps [DeMarco, 1995].

For conventional pillar design, Hsiung [1984] found that for a strong roof and coal, the maximum front and side abutment pressures are more sensitive to the Young's Modulus of the main roof than that of the immediate roof. If the roof and coal are relatively weak, the Young's Modulus of the immediate roof greatly controls the magnitude and distribution of the front abutment pressure. Chen [1989] showed that no significant effect was found for the Young's Modulus of coal-measures rock on the stress distribution within yield pillar.
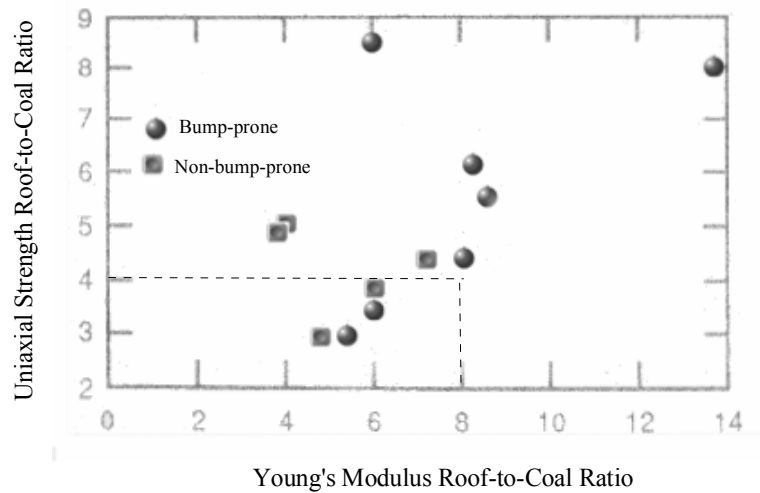
Figure 2-8 Strength ratio versus Young's modulus for roof and coal [after Malaki, 1995]

♦ **Interfacial Properties-** Although there are no direct measurements of the material properties of coalbed interfaces, Iannacchione [1990] indicated that the angle of internal friction could range from 10° to 20° and the cohesion could range from 0 psi for wet polished contacts to 200 psi for unpolished surfaces. There exists a considerable amount of information concerning the properties of other discontinuities. Barton [1976] indicated that the majority of un-weathered rock surfaces have an angle of internal friction ranging from 25° to 35° at medium stress levels, while Farmer [1983] reported an angle of internal friction of 10° to 20° for typical discontinuity with clay infill.

Babcock and Bickel [1984] used sample pillars with a width-to-height ratio of 8.5 from 15 mines and 11 seams. They concluded that the sudden release in constraint between the coal pillar and the surrounding strata could lead to coal bumps. The coal/rock confinement could be lost due to slippage between the coalbed and the surrounding rock.

A laboratory examination has been made on the effect of the condition of friction upon the ultimate compressive strength of coal specimens. A reduction of 50-60

percent have been verified in the ultimate strength of these model coal pillars when lubricants are applied between the faces as contrasted to non-lubricated faces, Khair [1968]. Patrick [1982] conducted a series of direct shear tests to determine the shear strength of pre-determined shear planes oriented to parallel the bedding planes of five coal seams. He showed that a nonlinear relationship exists between the contact pressure and the interfacial shear stress for different coal seams (Figure 2-9).
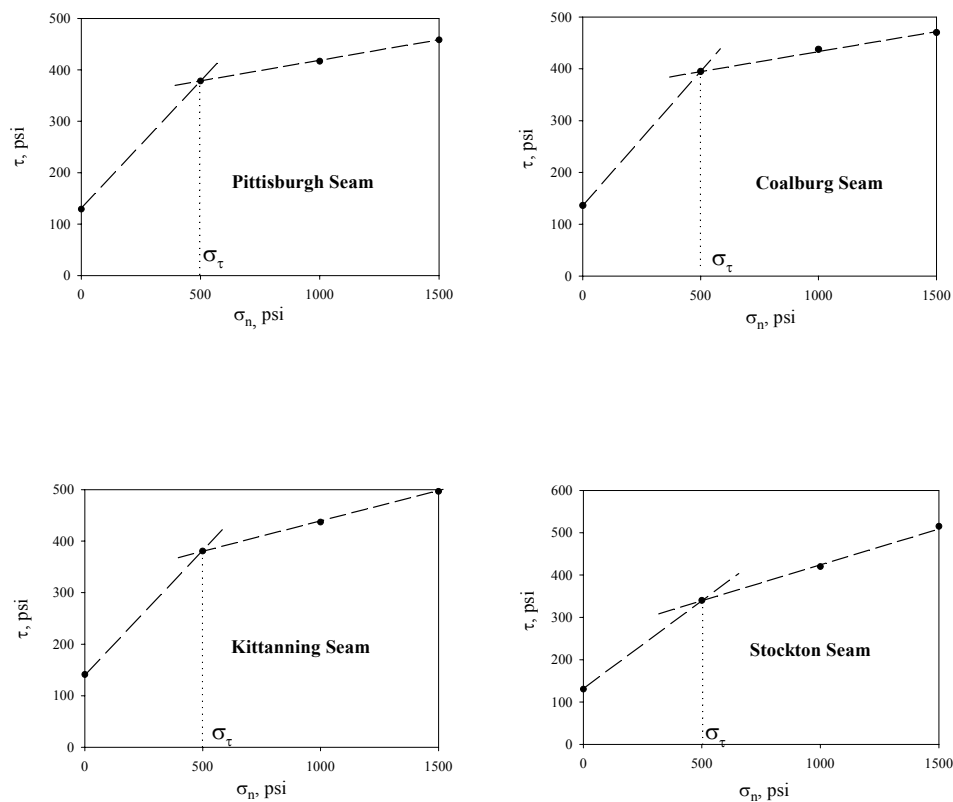
Figure 2-9 Shear strength as a function of normal stress, [after, Patrick, 1982]

2.4.3   Geometric Conditions

♦   **Overburden Depth-** The overburden depth is a major factor affecting the size of yield zone for 2-entry yield pillar system, Chen [1989]. To date, a correlation between gateroad performance and mining depth has been inconclusive, DeMarco

[1994]. This correlation does not appear to be of immediate concern in today's longwall industry, but it will certainly impact the future operations as the mining proceeds to greater depths in search of quality of deposits. DeMarco [1995] studied the western coal mine susceptible to bump-prone conditions. He found that in most coal bump conditions, the onset of bump problems has occurred around a depth of 1500 ft; however, there are exceptions to this rule of thumb.

Innacchione [1995] studied 50 mines that have experienced bumps. He found that the overburden thickness at these sites ranges from 470 ft to 2500 ft, but at most sites, overburden ranges from 1300 ft to 1800 ft. Only 10 mines experienced bumps where overburden thickness was less than 1000 ft. while 9 were operating under more than 2000 ft when bumps occurred.

Figure 2-9 shows a histogram for the mining depths associated with coal bumps in 39 mines in Colorado and Utah, [Heasley, 1999]. Figure 2-10 shows a wide range of overburden depths associated with coal bumps (650 – 2500 ft). The majority of bump cases occurred at overburden depths between 1575 ft and 2500 ft.

♦ **Panel width -** For conventional pillar design study, Hsiung [1984] found that the maximum front and side abutment pressures would increase continuously with the panel width if no yield zone developed in either the roof or coal. In the typical case, however, the yield zone starts to develop in the main roof above the pillar and above the center area of the face when the panel width exceeds a critical width.

♦ **Pillar width -** Yield pillars are generally 20 to 30 ft wide in a 6 to 8 ft seam (w/h ratio 3 to 5) and are typically intend to yield shortly after development or with the approach of the first panel face at a depth averaging around 1,500 ft. Larger pillars up to 45 ft wide have been used with intention of early yielding, but significant problems have been reported owing to inconsistent pillar yielding along the gate road length, [DeMarco, 1994].
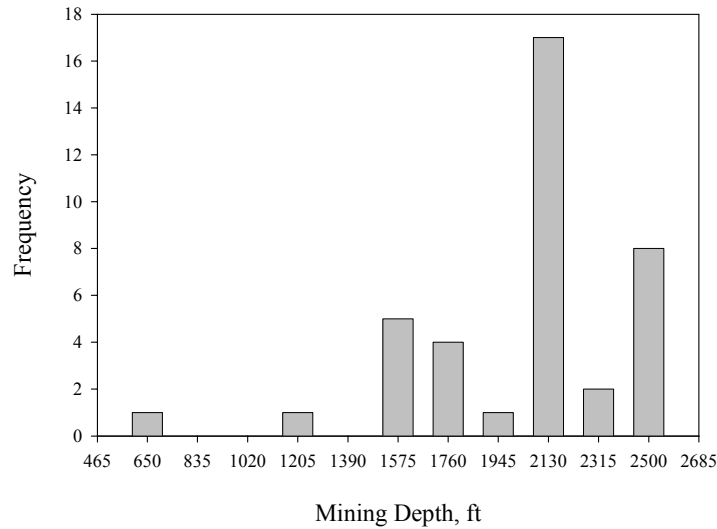
Figure 2-10 Frequency distribution of mining depths associated with coal bumps, [Heasley, 1999]

♦ **Entry width-** As a result of increasing the opening width, it was noted that the peak vertical stress in the stiff pillar increased, while the stress in the yield pillar did not change significantly [Haramy, 1988]. Chen [1989] tested the effect of entry width on the stress distribution in the yield pillar. The width of entry was tested from 10 to 28 ft. He concluded that the stress in the yield pillar did not change. However, the yield zone in the abutment and face did change considerably.

2.5 Longwall yield pillar design

Ground control problems associated with deep coal mines have increased interest in the design of longwall gateroads using yielding pillars. The current yield pillar design methodology is based on the traditional ultimate strength concept. This methodology estimates the probability of pillar stability as a ratio of the estimated in-situ pillar strength to the calculated pillar load. This design methodology is not satisfactory when the bump prone coal beds are encountered. The current yield pillar design methods tried to consider

the confinement effects of roof and floor on pillars and the bearing capacities of roof and floor.

The currently used yield pillar design methods could be classified into two types:

♦ Analytical such as Carr and Wilson's method.

♦ Numerical such as Chen's method and Tsang's method.

2.5.1 Carr and Wilson's method

Wilson's method [1977] is considered the first attempt for rational design of longwall chain pillars. His approach provides a mechanistic explanation of the effect of the pillar's width-height ratio on its strength, which is usually called the "confined core" concept. Carr and Wilson [1992] developed a modified version of the Wilson's method by introducing a new approach for estimating the abutment load distribution across a multi-entry gateroads. To use Carr and Wilson's method it is necessary to estimate the pillar strength using Wilson's progressive failure theory [Wilson, 1977]. Carr and Wilson [1992] method has been used extensively by Jim Walter Resources (JWR) Mining Division to size pillars at its longwall panels.

Wilson [1977] proposed an analytical solution for pillar stability based on the progressive failure theory. Wilson's theory can be summarized as follows. When the coal pillar is isolated from the surroundings, i.e. during development, the pillar may go through the following loading conditions, Figure 2-11:-

♦ **Initial Loading Stage** - During this stage, the pillar ribs lose their confinement and start to yield. This yield zone can not take more load, but it provides a constraint for the elastic pillar core due to the frictional resistance between the yielded pillar edges and the roof-and-floor of the excavation. The peak stress in the pillar is found at the boundary between the yield zone and the core.

♦ **Limit Roadway Stability (LRS) Stage** - As additional longwall loadings are applied, the average stress in the pillar core increases until it equals the peak stress at the yield zone boundary. During this stage, both the pillar and entries adjacent to it are expected to be stable.

♦ **Ultimate Limit (UL) of Resistance Stage** - Further loading of the pillar causes the yield zone to expand. Finally, the maximum bearing capacity of the pillar is reached when the entire core has yielded. Wilson assumed that the pillar maintains its ultimate loading capacity, UL, even after it has been exceeded. If the applied load is greater than the UL of the chain pillar, the additional load, called the transferred remnant load (TRL), is carried over to the adjacent pillar row.

For a wide pillar of width W that contains both yield and elastic zones, consider an element slice, of width *dx,* in the yield zone of that pillar (Figure 2-12). H is the pillar height. τ and μ are the shear stress and the coefficient of internal friction across the ends of the element, respectively. σ_z is the vertical stress acting on the element, σ_x is the horizontal confining stress on one side of the element with $\sigma_x + d\sigma_x$ on the other side. Ignoring the weight of the element, the equilibrium equation of that element is given by:

$$Hd\sigma_x = 2\mu\sigma_y dx \qquad\qquad \textbf{Equation 2-5}$$

$$\frac{d\sigma_x}{dx} = \frac{2\mu}{H}\sigma_z \qquad\qquad \textbf{Equation 2-6}$$

Wilson solved Equation 2-6, by making the following assumptions:-

1. The horizontal stress is equal to apparent cohesion of broken coal at rib side

$$\sigma_x = p = 14.5\,psi, \quad \text{at x} = 0 \qquad\qquad \textbf{Equation 2-7}$$
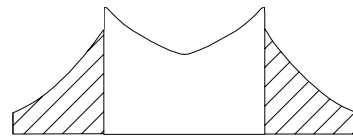
(A) Initial Pillar Stress Profile
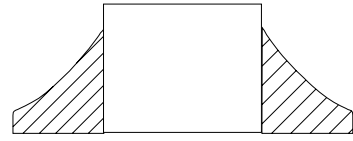
(B) Limit of Roadway Stability Stress Profile
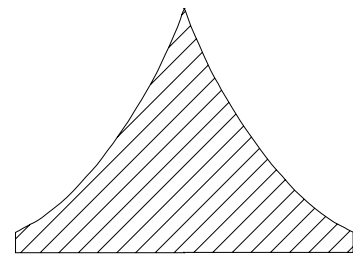
(C) Ultimate Limit of Resistance Stress Profile

☐ Elastic Solid Coal   ⧄ Yielded Coal

Figure 2-11 Vertical stress distributions profiles in coal pillars, after Wilson 1982
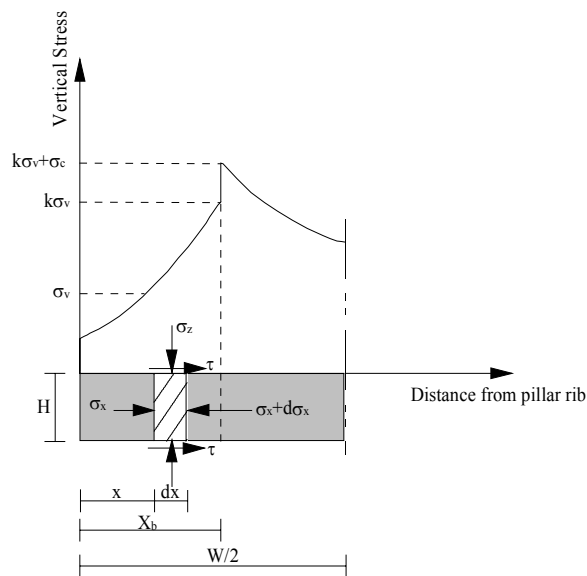
Figure 2-12 Forces acting on an element strip in wide pillar

2. The horizontal stress reaches the original horizontal stress level at the yield-elastic boundary. In his derivation he assumed the virgin horizontal stress is equal to the overburden stress, σ_v.

$$\sigma_x = \sigma_v = \gamma Z , \qquad \text{at } x = X_b \qquad\qquad \textbf{Equation 2-8}$$

where γ and Z are the rock specific weight and overburden depth, respectively.

3. The stress in the yield zone is governed by Mohr-Coulomb's failure criterion and the uniaxial compressive strength abruptly drop to zero at yield:

$$\sigma_z = k\sigma_x , \qquad k = \frac{1+\sin\phi}{1-\sin\phi} \qquad\qquad \textbf{Equation 2-9}$$

where σ_z is the confined strength of the material; σ_x is confinement stress; k is the triaxial stress constant; and ϕ is the angle of internal friction.

Therefore, the vertical stresses at the yield-elastic boundary are given by:

$$\sigma_z = k\sigma_v \qquad \text{(Yield side of boundary)} \qquad \textbf{Equation 2-10}$$

$$\sigma_z' = k\sigma_v + \sigma_c \qquad \text{(Elastic side of boundary)} \qquad \textbf{Equation 2-11}$$

where σ_c is the in-situ uniaxial compressive strength of coal.

Wilson assumed two possible boundary conditions at the coal pillar/rock interfaces:-

♦ Rigid Roof and Floor (RRF) – in which the yielding only takes place in coal pillar.

♦ Yield Roof and Floor (YRF) - in which yielding takes place all around the entry.

Wilson provided equations to determine the width of yield zone and the distributions of vertical and horizontal stresses in that zone during the LRS loading stage for the proposed boundary conditions, as follows:

For RRF boundary condition – the vertical and horizontal stresses at a distance x from the pillar rib are given by:

$$\text{Vertical Stress, } \sigma_z = pke^{\frac{x}{H}F} \qquad \text{Equation 2-12}$$

$$\text{Horizontal Stress, } \sigma_x = pe^{\frac{x}{H}F} \qquad \text{Equation 2-13}$$

where,

$$F = \frac{k-1}{\sqrt{k}} + \frac{(k-1)^2}{k}\tan^{-1}\sqrt{k}$$

Equating the horizontal stress in Equation 2-13 to the virgin horizontal stress in Equation 2-8, the width of yield zone, X_b for RRF condition can be calculated by

$$X_b = \frac{H}{F}\ln\left(\frac{\gamma Z}{p}\right) \qquad \text{Equation 2-14}$$

For YRF boundary condition – the vertical and horizontal stresses at a distance x from the pillar rib are given by:

$$\text{Vertical Stress, } \sigma_z = pk\left(\frac{2x}{H}+1\right)^{k-1} \qquad \text{Equation 2-15}$$

$$\text{Horizontal Stress, } \sigma_x = p\left(\frac{2x}{H}+1\right)^{k-1} \qquad \text{Equation 2-16}$$

Equating the horizontal stress in Equation 2-16 to the virgin horizontal stress in Equation 2-8, the width of yield zone, X_b for RRF condition can be calculated by

$$X_b = \frac{H}{2}\left(\left(\frac{\gamma Z}{p}\right)^{\frac{1}{k-1}}-1\right) \qquad \text{Equation 2-17}$$

The load bearing capacity, P of a square pillar of width, W can be determined by integrating the pillar vertical stress over the pillar area as follows:

$$P = \sigma_y \left(W - 2X_b\right)^2 + 4\int_0^{X_b} \sigma_y \left(W - X_b\right)dx \qquad \text{Equation 2-18}$$

For RRF boundary condition – the pillar bearing capacities for LRS and UL stages are given by:

$$P(LRS) = \frac{4Hpk\left(W - X_b\right)}{F}\left(e^{\left(\frac{FX_b}{H}\right)} - 1\right) + \left(k\gamma Z + \sigma_c\right)\left(W - 2X_b\right)^2$$

Equation 2-19

$$P(UL) = \frac{2HpkW}{F}\left(e^{\left(\frac{FW}{2H}\right)} - 1\right) \qquad \text{Equation 2-20}$$

For YRF boundary condition – the pillar bearing capacity for LRS and UL boundary conditions is given by:

$$P(LRS) = \frac{4pX_b^k\left(W - X_b\right)}{\left(H/2\right)^{k-1}} + \left(k\gamma Z + \sigma_c\right)\left(W - 2X_b\right)^2 \quad P(UL) = \frac{2p\left(W/2\right)^{k+1}}{\left(H/2\right)^{k-1}}$$

Equation 2-21

2.5.2   Chen's Method

Chen [1989] developed a method for yield pillar design. The method is a combination of numerical modeling and the Wilson's confined core concept. Chen used an elastic-plastic model to describe the pillar yielding. The basis of this model is

Drucker-Prager yield criterion. Chen assumed a simplified stress-strain curve, (Figure 2-13) to simulate coal material.
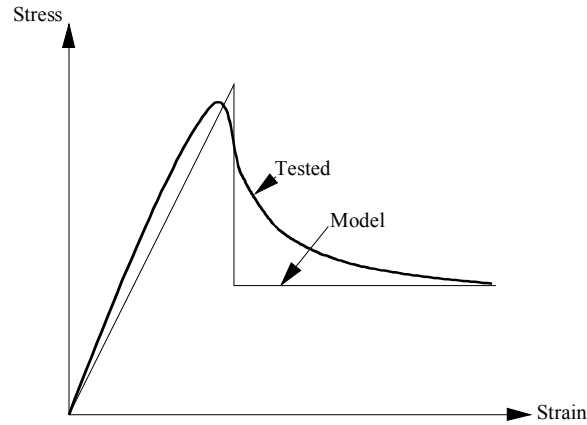
Figure 2-13 Stress-strain curve for coal, [Chen, 1988]

Chen conducted a parametric study using 2D finite element models to define the stress distribution in the pillar yield zone. Based on the statistical analysis for the results of finite element simulations, Chen developed a mathematical model concerning the stress distribution in the yield zone. Furthermore, he established the formulae to determine the pillar bearing capacity and the width of yield zone. Finally, based on the method of estimating pillar loading, Chen proposed three possible yield pillar sizes; namely the maximum, the recommended, and the minimum.

Chen studied the behavior of yield zone using 2D finite element model. In the simulation, a range of values was used for the input parameters. The triaxial stress factor, k covered a range from 3.5 to 4.5 and Poisson's ratio from 0.3 to 0.4. The virgin horizontal stress, σ_h is assumed to be:

$$\sigma_h = \frac{v}{1-v}\sigma_v \qquad\qquad \textbf{Equation 2-22}$$

where σ_v is the virgin vertical stress; and v is the Poisson's ratio of coal.

The simulations results were statistically analyzed to develop a simple formula describing the horizontal stress distribution σ_x in the yield zone, (Equation 4-23).

$$\sigma_x = k^{1.7}\left(0.17v^2 + 0.057v - 0.028\right)\left[454\left(\frac{x}{H}\right)^3 + 6545\left(\frac{x}{H}\right)^2\right]$$

<div align="right">**Equation 2-23**</div>

where x is the distance from the pillar rib side into the yield zone; H is the pillar height; and k is the triaxial stress factor.

Similar to Wilson's method (Equation 2-9), Chen assumed that the linear relationship between coal strength and the confining pressure is still valid in the yield zone. Hence; the vertical stress, σ_z at any distance x from pillar's rib, is determined by:

$$\sigma_z = k^{2.7}\left(0.17v^2 + 0.057v - 0.028\right)\left[454\left(\frac{x}{H}\right)^3 + 6545\left(\frac{x}{H}\right)^2\right]$$

<div align="right">**Equation 2-24**</div>

Using the same assumption as in Wilson's method, Chen assumed that the horizontal stress at the inner boundary of the yield zone is equal to the virgin horizontal stress. But instead of using the virgin value obtained from Equation 2-22, Chen assumed the same value used by Wilson, i.e., $\sigma_x = \gamma Z$, where Z and γ are the depth and unit weight of the overburden, respectively. The width of yield zone as estimated by Chen is given by:

$$X_b = H\left(9.61 \times \cos\left[\frac{1}{3}\cos^{-1}\left(\frac{\gamma Z \times 10^{-5}}{k^{1.7}\left(0.17v^2 + 0.057v - 0.028\right)} - 1\right)\right] - 4.8\right)$$

<div align="right">**Equation 2-25**</div>

Following a similar derivation as in Wilson's method, the equations for estimating the load bearing capacity of square pillar are as follows:

Pillar has no elastic core

$$P = k^{2.7} \left(0.17v^2 + 0.057v - 0.028 \right) \left(273 \frac{W^4}{H^2} + 5.68 \frac{W^5}{H^3} \right)$$

Equation 2-26

Pillar has an elastic core

$$P = k^{2.7} \left(0.17v^2 + 0.057v - 0.028 \right)$$
$$\left(273 \frac{X_b^4}{H^2} + 5.68 \frac{X_b^5}{H^3} + \left(W - 2X_b \right) \left(1090 \frac{X_b^3}{H^2} + 28.4 \frac{X_b^4}{H^3} \right) \right)$$
$$+ \left(W - 2X_b \right)^2 \left(\sigma_c + k\gamma Z \right)$$

Equation 2-27

where W is the pillar width; (σc +kγZ) is the strength of the elastic core; and σc is the in-situ uniaxial compressive strength of coal;

Chen defined the yield pillar as a pillar without an elastic core. Based on the stress level that developed in the yield zone, Chen defined three types of yield pillar width.

The maximum (critical) yield pillar width is considered to be twice the width of the yield zone predicted by Equation 2-25.

$$W = 2X_b$$

The recommended yield pillar is defined as the pillar width that satisfies the following condition: the peak vertical stress at the center of a completely yielded pillar equals the average tributary stress.

$$\frac{\gamma Z \left(W + W_o \right)^2}{W^2} = k^{2.7} \left(0.17v^2 + 0.057v - 0.028 \right)$$
$$\left[454 \left(\frac{W}{2H} \right)^3 + 6545 \left(\frac{W}{2H} \right)^2 \right]$$

Equation 2-28

where W_o is the entry width.

The above equation can be solved with respect to pillar width, W with a few simple iterations.

The minimum pillar width is the width of yielded pillar that support the roof strata below the pressure arch.

$$\frac{2}{3}\gamma D W_T \left(W + W_o\right) = k^{2.7} \left(0.17v^2 + 0.057v - 0.028\right)$$
$$\left(273\frac{W^4}{H^2} + 5.68\frac{W^5}{H^3}\right) \qquad \textbf{Equation 2-29}$$

where W_T is the width of pressure arch, $W_T = W + 2W_o$; and D is the height of pressure arch, $D = 2W_T$.

2.5.3 Tsang's method

Tsang [1992] developed a method for yield pillar design in three-entry gateroad systems. Tsang developed regression equations to present the relationships between the stability conditions of entry system; i.e. roof, pillar and floor, and the studied variable for different roof and floor conditions (Table 2-2). To develop the regression equations, Tsang used two-dimensions finite element models combined with fractional factorial experiment design. A three-level orthogonal design for the most significant variables was used to minimize the number of FE models.

Based on the recommended pillar safety factor (Table 2-3), Tsang method can be used to design different types of three-entry system; i.e. Stiff-Stiff (S-S), Yield-Stiff (Y-S) and Yield-Yield (Y-Y). Tsang assumed that the pillar widths estimated by the regression equations in Table 2-3, are initial pillar widths. These initial pillar widths should be increased in the followings cases:

♦ If the roof tensile strength was less than the estimated maximum tensile stress.

♦ If the floor and/or roof safety factors, were less than 1.3.

Table 2-2 Regression equations for different roof/floor conditions [after Tsang, 1993]

	Regression Equations
Strong Roof and Strong Floor	$W_1 = \left(\dfrac{C}{Z}\right)^{-0.4048}\left(52.7884SF_1 - 15.4181SF_2 + 0.0005HW_p\right)$ $W_2 = \left(\dfrac{C}{Z}\right)^{-0.5581}\left(44.9214SF_2 - 23.1242SF_1 + 0.0005HW_p\right)$ $T_r = Z^{0.7454}\left(\dfrac{2.9877}{\sqrt{W_1}} + \dfrac{1.0168}{\sqrt{W_2}} + 2.8\times10^{-9}W_eE_r\right)$
Strong Roof and Weak Floor	$W_1 = \left(\dfrac{C}{Z}\right)^{-0.4162}\left(57.1280SF_1 - 24.9814SF_2 + 1.03\times10^3\dfrac{HW_p}{E_f}\right)$ $W_2 = \left(\dfrac{C}{Z}\right)^{-0.4931}\left(52.9712SF_2 - 30.3162SF_1 + 1.03\times10^3\dfrac{HW_p}{E_f}\right)$ $T_r = Z^{0.6775}\left(\dfrac{3.7869}{\sqrt{W_1}} + \dfrac{1.2029}{\sqrt{W_2}} + 9.7\times10^{-9}W_eE_r\right)$ $SF_f = 2.162\times10^{-3}\left(\dfrac{E_f}{Z}\right)^{0.4442}\left(0.2548W_1 + 0.1403W_2 + 6.4\dfrac{\sigma_h}{W_p}\right)$
Weak Roof and Strong Floor	$W_1 = \left(\dfrac{C}{Z}\right)^{-0.4135}\left(62.7666SF_1 - 22.8459SF_2 + 8.15\dfrac{HW_P}{E_r}\right)$ $W_2 = \left(\dfrac{C}{Z}\right)^{-4616}\left(62.8519F_1 - 29.7170SF_2 + 1.8\times10^2\dfrac{HW_P}{E_r}\right)$ $SFr = 2.398\times10^{-3}\left(\dfrac{E_r}{Z}\right)^{0.4367}\left(0.2384W_1 + 0.1217W_2 + 4.5\dfrac{\sigma_h}{W_p}\right)$ $T_f = Z^{0.8759}\left(\dfrac{1.3043}{\sqrt{W_1}} + \dfrac{0.4907}{\sqrt{W_2}} + 3.4\times10^{-4}W_eE_r + \dfrac{0.9236}{\sigma_h}\right)$
Weak Roof and Weak Floor	$W_1 = \left(\dfrac{C}{Z}\right)^{-0.5235}\left(52.7862SF_1 - 15.2109SF_2 + 1.17\times10^7\dfrac{HW_p}{E_rE_f}\right)$ $W_2 = \left(\dfrac{C}{Z}\right)^{-0.5341}\left(53.7009SF_2 - 23.4415SF_1 + 2.02\times10^3\dfrac{HW_p}{E_rE_f}\right)$ $SF_r = 4.521\times10^{-3}\left(\dfrac{E_r}{Z}\right)^{0.3908}\left(0.1339W_1 + 0.1532W_2 + 6.5989\dfrac{\sigma_h}{W_p}\right)$ $SF_f = 2.4\times10^{-4}\left(\dfrac{E_f}{Z}\right)^{0.6032}\left(0.5568W_1 + 0.8454W_2 + 53.8824\dfrac{\sigma_h}{W_p}\right)$

where:

   W_1 and W_2 are pillar widths for pillar 1 and pillar 2, respectively, ft;

SF_1 and SF_2 are the safety factors for pillar 1 and pillar 2, respectively;

SF_r and SF_f are the safety factors for immediate roof and floor, respectively;

C is the cohesion strength of the coal, psi;

Z is the overburden depth, ft;

H is the pillar height, ft;

W_e is the entry width, ft;

W_p is the panel width, ft;

E_r and E_f are the Young's module of the immediate roof and floor, respectively, psi;
σ_h is the virgin horizontal stress, psi; and

T_r is maximum tensile stress in the roof, psi.

Table 2-3 Recommended pillar safety factors for Tsang's method

Design Layout	SF (Stiff Pillar)	SF (Yield Pillar)
Stiff-Stiff (S-S)	1.3	1.3
Yield-Yield (Y-Y)	0.9	0.9
Stiff-Yield (S-Y)	1.5	0.9

CHAPTER 3

LONGWALL MODELING

In recent years, a variety of numerical modeling procedures have been developed to determine the design requirements and stability conditions of underground excavations. These methods include both 2-D and 3-D applications of finite element, finite difference, discrete element, and boundary-element codes. In this study a commercial finite element code, ABAQUS/standard [ABAQUS, 1998], was used to model the longwall panel. A method for yield pillar design was developed by combining the FE modeling with a full factorial design for the factors that affect the yield pillar stability. As shown in Figure 2-1, the longwall panel is a complex structure because of the following reasons:

- ♦ It is a relatively large three-dimensional problem;

- ♦ It consists of a number of non-classical materials: such as roof and floor rocks, coalbed, and gob;

- ♦ It involves a sequence of panel retreating and gob formation.

It is well known that the results of computer modeling cannot be any better than the accuracy of the input parameters. These parameters include the constitutive equations of the model materials, e.g. rocks, coal and gob, and the variations of geological conditions. Through this chapter a rational modeling for longwall panel is presented by adopting the available modeling capabilities of ABAQUS program.

3.1 Finite element code - ABAQUS/standard

ABAQUS/Standard is a general-purpose finite element program. ABAQUS version 5.8 is used in this study. Unfortunately, most of commercial finite element codes,

e.g. ABAQUS do not have a ready-made model for underground mining applications. However, these codes usually provide the user with an interface to define new material models or to interact with the default ones. FORTRAN user subroutines can be included in the ABAQUS finite element models to customize the behavior of the model materials.

3.1.1   Material yield model

The linear Drucker-Prager plasticity model is one of the inelastic models provided by ABAQUS. The main characteristics of the Drucker-Prager yield criterion are summarized below: -

- ♦ It can be used to model frictional materials, which are typically granular-like soils and rocks.
- ♦ It can be used to model materials in which the tensile and compressive yield strength are significantly different.
- ♦ The yield behavior depends on the hydrostatic pressure. One of the consequences of this is that the material becomes stronger as the confining pressure increases.
- ♦ The material may harden or soften isotropically.
- ♦ The inelastic behavior will generally be accompanied by some volume change: the flow rule may include inelastic dilation as well as inelastic shearing.
- ♦ The yield behavior may be influenced by the magnitude of the intermediate principal stress.

The classical Drucker-Prager yield condition [Desai et al., 1984] is expressed as follows: -

$$f \equiv \alpha J_1 + \sqrt{J_{2D}} - k = 0$$
<div style="text-align:right">**Equation 3-1**</div>

where α and k are the material property constants related to cohesion and angle of internal friction; J_1 is first invariant of stress tensor; and J_{2D} is the second invariant of the deviator stress tensor.

$$J_1 = \sigma_1 + \sigma_2 + \sigma_3 \qquad\qquad\qquad \textbf{Equation 3-2}$$

$$J_{2D} = \frac{1}{6}\left[(\sigma_1 - \sigma_2)^2 + (\sigma_2 - \sigma_3)^2 + (\sigma_1 - \sigma_3)^2\right] \qquad \textbf{Equation 3-3}$$

where σ_1, σ_2, and σ_3 are the major, the intermediate, and the minor principal stresses, respectively.

Equation 3-1 represents a straight line on a J_1 versus J_{2D} plot (Figure 3-1). In the three-dimensional stress space, the criterion is expressed by a right circular cone, and the projection on the Π plane is a circle, as shown in Figure 3-1. Different material constants will produce different shapes of cones and circles. As shown in Figure 3-1, the intermediate circle represents the yield surface at peak strength of the material. Prior to yielding, all stress conditions inside that circle are in the elastic state. When the point representing the stress condition reaches the surface of the yield circle, the coal begins to yield. Depending on the state of stress, with further plastic deformation the material may experience strain hardening and the yield surface expands outward. On the other hand, if the material falls in the range of strain softening, plastic deformation causes the yield surface to contract or move inward.
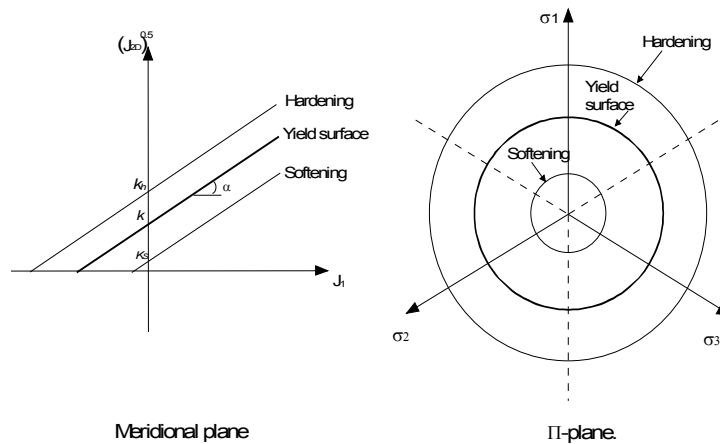
Figure 3-1 Linear Drucker-Prager criterion on Meridional and Π planes

The elastic-plastic form of the Drucker-Prager criterion, Equation 3-1, was used to model the immediate roof and floor rocks. As will be illustrated in section 3-2-1, an adapted version for Drucker-Prager model was used to simulate the coal pillars.

3.1.2   Local instability analysis

Some types of analyses may develop local instabilities such as material softening. In such cases the structure must release strain energy to remain in equilibrium. One approach to stabilize such a structure is to use dashpots during a static analysis. ABAQUS offers an automated version of this approach through artificial damping. Automatic volume proportional damping is applied to the model in such a way that the viscous forces introduced are small enough not to perturb the solution too much. ABAQUS generates an artificial mass matrix M by using a unit density and a damping coefficient c such that during the first increment the dissipated energy is a small fraction of the incremental strain energy. Therefore, the global equilibrium equation is given by

$$P - I - F_v = 0 \hspace{4cm} \textbf{Equation 3-4}$$

where P is the external forces; I is internal (nodal) forces; F_v is the viscous forces of the form $F_v = cMv$; $v = \dfrac{\Delta u}{\Delta t}$ is the vector of nodal velocities; and Δt is the increment of time.

It is assumed that the problem is stable at the beginning of the step and that instabilities may develop in the course of the step. While the model is stable, viscous forces and, therefore, the viscous energy dissipated are very small. If a local region goes unstable, the local velocities increase and, consequently, part of the strain energy then released is dissipated by the applied damping. ABAQUS calculates the damping coefficient, c, based on the solution of the first increment of a step. Increments in strain energy and in viscous dissipated energy are calculated and extrapolated to the total step time. The damping coefficient is then determined in such a way that the dissipated energy is a small fraction of the strain energy. This fraction, the damping intensity, is controlled by the user and has a default value of $2*10^{-4}$.

3.1.3   Contact model

ABAQUS can simulate different types of contacts. In this study, the surface-based contact will be used to simulate the contact between rock strata. ABAQUS defines the contact between two strata in terms of two surfaces that may interact; these surfaces are called "slave" and "master". When the surfaces are in contact they usually transmit shear as well as normal forces across their interface. The relationship between the normal and shear forces at the interface of the bodies is known as the friction model. The default friction model in ABAQUS is the classical isotropic Coulomb friction model, (Figure 3-2).

In classical Coulomb friction model, two contacting surfaces can carry shear stresses up to a certain magnitude across their interface before they start sliding relative to one another; this state is known as sticking. The Coulomb friction model defines this critical shear stress, τ_{crit}, at which sliding of the surfaces starts as a fraction of the contact pressure, σ_n, between the surfaces, as follows:

$$\tau_{crit} = \mu \sigma_n \qquad\qquad \textbf{Equation 3-5}$$
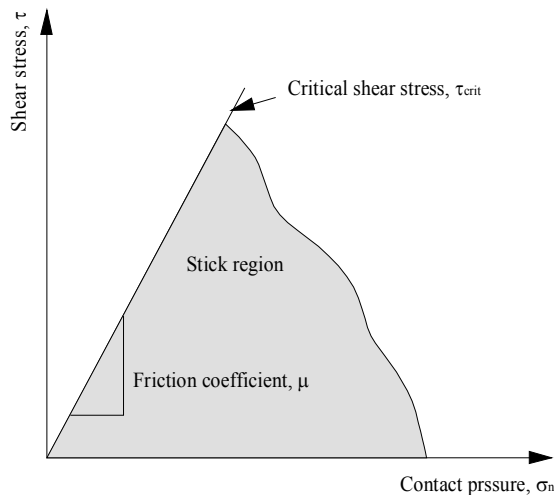
Figure 3-2 Linear Coulomb friction model

Iannacchione [1990] concluded that a friction coefficient, μ of 0.25 is suitable to simulate the roof/pillar and floor/pillar interfaces. Figure 2-9 illustrated that the relationship between the contact pressure and critical shear stress is bi-linear. The intercept of the two linear segments occurs at the transition stress (σ_τ) between modes of failure represented by asperity override and the shearing of the asperities [Barton, 1976].

ABAQUS provides an upper bound for the shear stress across the interface, (Figure 3-3). Figure 3-3 shows that, regardless of the magnitude of the contact pressure stress, sliding will occur if the magnitude of the interfacial shear stress reaches certain limit, τ_{max}.
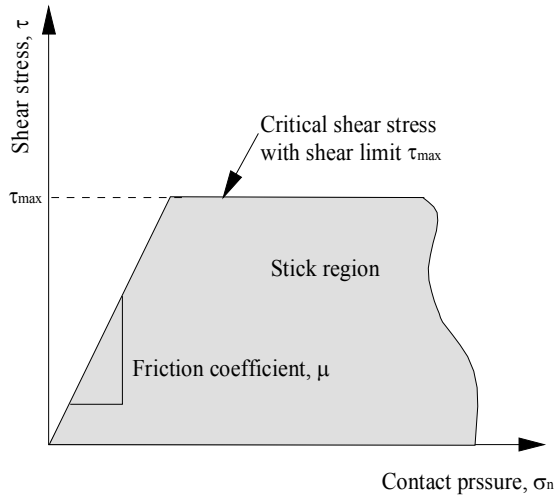
Figure 3-3   Coulomb friction model with a limit on the critical shear stress

Compared with the linear Coulomb friction model, it is obvious that the Coulomb friction model with a limit on the critical shear stress is more representative to the laboratory results presented in Figure 2-9. Figure 2-9 shows that the slope of the second linear segment is relatively much smaller than the slope of the first linear segment. Therefore, shear stress corresponding to the intersection of the bi-linear model could be used as an upper shear stress limit for Coulomb friction model. This limit will be called the shear limit of the coal/rock interface.

3.2 Materials models for longwall modeling

The in-situ coal and rocks are inhomogeneous and contain numerous discontinuities which affect their mechanical properties. The specimen tested in the laboratory only represents the intact portions of the tested rock. To consider the size effect of the tested specimen, a reduction factor of 1/5 could be applicable to the uniaxial compressive strength determined by laboratory tests [Van Dillen, 1978]. Unlike the uniaxial compressive strength, the Young's modulus and Poisson's ratio are independent of the specimen size and shape [Skelly, 1977 and Van Dillen, 1978]. Hence; through this study no reduction will be done to the material Young's modulus and Poisson's ratio. Only the reduction will be done for the uniaxial compressive strength.

3.2.1   Coal pillar model

Because of non-uniform stress distribution in the coal mine structures, some parts of coal pillar are subjected to yielding while other parts are still in the elastic range. Consequently, in order to simulate these structures with confidence, the complete stress-strain relationship of the model materials must be considered.

3.2.1.1 Coal model characteristics

The complete load-deformation characteristics of coal pillar can be described by the modulus of elasticity, strength and post-peak stiffness. In addition, the complete stress-strain curves are highly dependent on the width-to-height ratio of the test specimens and the confining pressure.

♦ **Modulus of Elasticity**

In-situ measurements illustrated that the modulus of elasticity of coal pillar is a true material property and independent of the geometrical dimensions of the pillar, such as size, height, and width-to-height ratio, Figure 3-4. Wagner [1974] and Van Heerden [1975] found that the average modulus of elasticity of coal pillar is approximately 5.8 x

10^5 psi. Laboratory tests illustrated that the modulus of elasticity of the specimen is not influenced by its width-to-height ratio. The values between 3.5 x 10^5 and 8 x 10^5 psi were measured for different Indian coal seams [Das, 1986]. The modulus of elasticity for laboratory specimens shows no clear dependence on confining pressure (Figure 3-4). The values between 3.16 x 10^5 and 6.2 x 10^5 psi were measured for different Australian coal seams by Medhurst and Brown [1998].

♦ **Post-Peak Stiffness**

For small width-to-height pillar ratios, less than 4, the post-peak pillar stress is continuously decreased as the deformation increases and sometimes reaches zero (Figure 3-4). This behavior is explained by low triaxial confinement at the specimen of small width-to-height ratio [Das, 1986; Wagner, 1974; Van Heerden, 1975]. For the pillars of width-to-height ratio greater than 4 or 6, the post-peak curves begin to fall initially followed by rising up to regain strength (Figure 3-4). This could be explained by the reconsolidation of the broken mass, which is due to high lateral constraints provided at the center of the specimen [Das, 1986]. Unlike the modulus of elasticity the width-to-height ratio has a marked effect on the post-peak stiffness (i.e. maximum slope after failure strength) of coal pillars. Generally speaking, the post-peak stiffness decreases with increasing width-to-height ratio (Figure 3-4). This indicates that the post-peak behavior of a pillar is a structural property rather than an inherent material property.
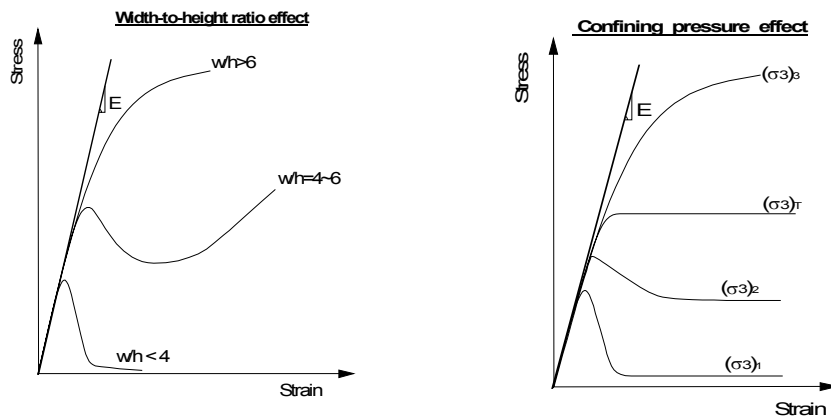
Figure 3-4 Conceptual stress-strain curves for coal material

Van Heerden [1975] concluded that the post-peak stiffness reaches a constant value of 7.25×10^4 psi at a small width-to-height ratio of 3. Das [1986] concluded that the post-peak stiffness become zero at higher width-to-height ratio of 10 and becomes positive with further increases in width-to-height ratio. Ozbay [1989] concluded that a pillar with width-to-height ratio of 5 has a zero post-peak stiffness. Babcock and Bickel [1984] and Campoli et al., [1990] reported that even pillars with width-to-height ratio grater than 8 were subjected to bump failures. Barron [1992] illustrated that the post-peak stiffness of coal specimen decreases with the increase in confining pressure and becomes positive at high confining pressures. Pen and Barron [1994] fitted a large number of in-situ and laboratory data to determine the relationship between the width-to-height ratio and the normalized post peak stiffness. Their relationship lies in the upper bound of the post-peak stiffness of pillar estimated from the available data.

$$\frac{K_p}{E} = 5.98243 \left(\frac{W}{H}\right)^{-1.1976}$$ **Equation 3-6**

where *Kp* is the post peak stiffness of the pillar; *E* is the Young's modulus of the pillar, *W* is the width of the pillar; and *H* is the height of the pillar.

♦ **Strength**

To describe the complete stress-strain behavior of coal pillars, two types of strengths have to be defined, namely; peak strength and residual strength. The *peak strength* is defined by a stress value at which the slope of the stress-strain curve changes from the positive value to zero or negative value. The *residual strength* is defined by a stress level at which the slope of the stress-strain curve holds constant at approximately zero value while the pillar deforms.

According to the experience gained from the laboratory and in-situ experiments conducted on coal, the peak strength of large coal mass is lower than the peak strength determined by laboratory testing on small specimens. For South African coal seams, Bieniawski [1968] concluded that 5 ft cubic specimens represent the critical size beyond which the peak strength of the coal block remains constant with increasing specimen size.

Bieniawski [1992] estimated the critical size for US coal seams to be 36 in. Mark [1990] assumed an in-situ compressive strength of 900 psi for US coal fields. Many researchers [Holland-Gady, 1957; Holland, 1964; Obert and Duvall, 1967; Salamon and Munro, 1967; Bieniawski, 1968; Wagner, 1974; Van Heerden, 1975; and Das, 1986] studied the effect of width-to-height ratio on the peak strength of coal pillars. Generally speaking, in spite of the form of the developed relationships between the width-to-height ratio and the peak strength, the peak strength increases with increasing width-to-height ratio (Figure 3-4).

Figure 3-5 shows the results of triaxial tests conducted on six US coal seams, namely; Wabash seam No. 5 (C1), Blue Creek (C2), Mary Lee (C3), Pittsburgh seam (C4), Castlegate No. 3 (C5), and Castlegate No (C6). It is obvious that the coal peak strength is linearly proportional to the confining pressure [Sun and Peng, 1993]. The correlation coefficients for different coal seams range from 0.79 to 0.99.
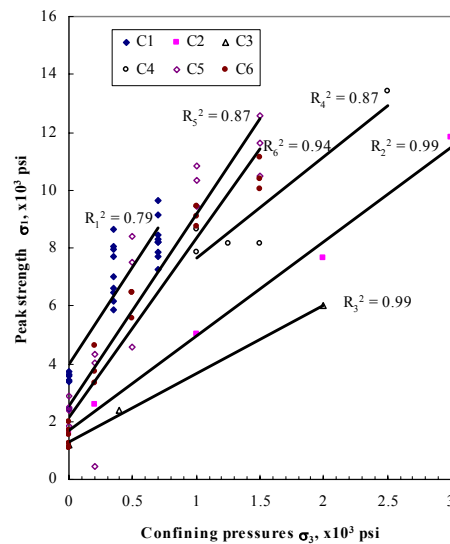
Figure 3-5 Peak strength curves for coal samples of different coal seams

Unlike the peak strength, only a few researchers have studied the effect of pillar width-to-height ratio and the confining pressure on the residual strength. Das [1986] concluded that the pillar residual strength is increased exponentially with increasing

width-to-height ratio. Figure 3-6a shows that the relationship between the coal residual strength and confining pressure for some UK coal seams is linear [Medhurst and Brown, 1998]. The same relationship is obtained for some Brazilin coal seam (Figure 3-6b) [Zingano, 2001].
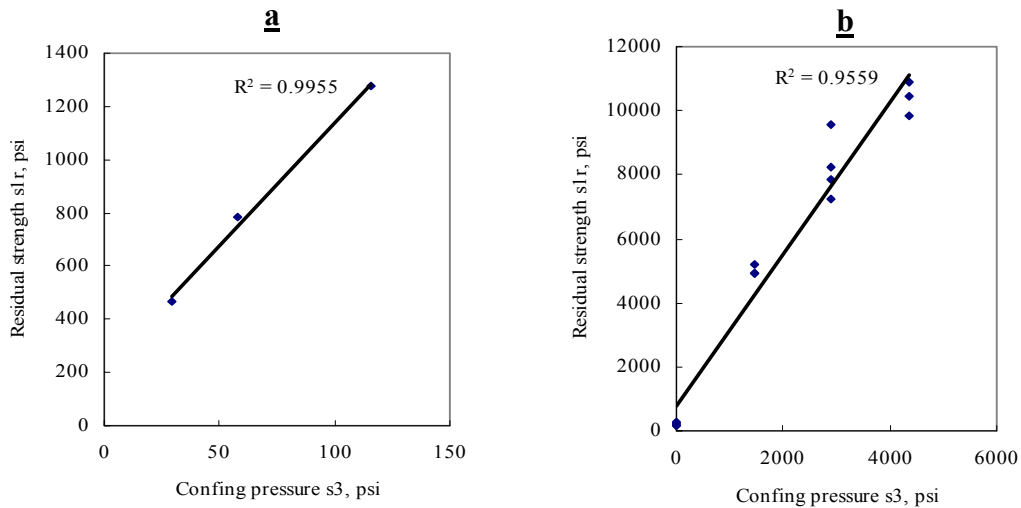
Figure 3-6 Coal residual strength vs. confining pressure

♦ Brittle-Ductile Transition

The behavior of most rocks change from brittle to ductile at some elevated confining pressure $(\sigma_3)_T$ (Figure 3-7). It is postulated that such transition can occur in coal in the range of confining pressure normally encountered in mining. The brittle-ductile transition point is defined by Barron [1992] as the point of intersection between the peak stress failure criterion and the residual strength criterion (Figure 3-7). Mogi [1971] defined the residual strength criterion for many rocks as linear relationship between the residual strength, σ_{r1} and the confining pressure, σ_3, Equation 3-7:

$$\sigma_{r1} = 3.4\sigma_3 \hspace{4cm} \textbf{Equation 3-7}$$
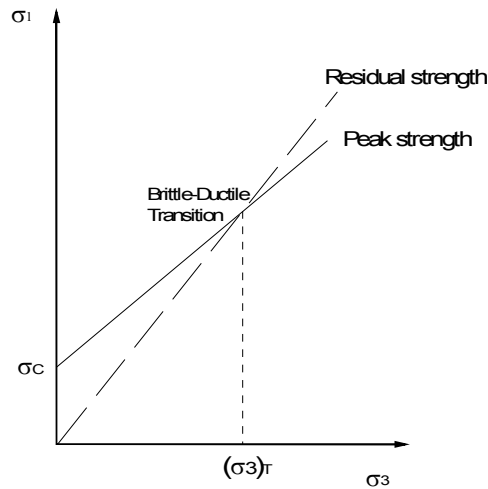
Figure 3-7 Typical peak strength and residual strength curves for coal material

♦ **Isotropic strain hardening-softening model for coal material**

An elastic-plastic material model with no hardening/softening has been used frequently in numerical modeling to simulate the behavior of coal pillars. However as explained above, the in-situ stress-strain curve for coal pillar exhibits both hardening and softening behavior depending on the state of stress. The extended Drucker-Prager model, available in ABAQUS, describes the behavior of rock-like materials in which the yield behavior depends on the equivalent pressure stress. It allows a material to harden and/or soften isotropically.

The hardening or softening behavior is achieved by making the parameter k dependent on the applied plastic deformation (e.g. plastic strain), while the other parameter α holds constant [Maier and Hueckel, 1979]. Therefore, the classical Drucker-Prager criterion (Equation 3-1) for isotropic hardening/softening can be rewritten as (Equation 3-8):

$$f \equiv \alpha J_1 + \sqrt{J_{2D}} - k^* = 0 \qquad \qquad \textbf{Equation 3-8}$$

where k^* is a mobilized cohesion parameter.

♦ **Friction Hardening**

To illustrate the friction hardening, consider the strain softening model in Figure 3-8. The deviator stress q increases in the early stage of loading until it reaches the peak strength and then decreases and finally reaches the residual strength. On the other hand, the frictional component increases during the whole deformation process up to and remain at residual strength state [Adachi et al., 1991]. Adachi and Oka [1985] defined the rapid increase of frictional component during loading process as stress history tensor. The difference between applied stress and stress history tensor corresponds to the cohesive strength due to cementation or bonding. The cohesive strength can be destroyed by deformation.

Holding the material parameter α constant in Equation 3-8 makes the peak strength and the residual strength failure envelops parallel; i.e., the brittle-ductile transition is not possible and it leads to a constant post peak modulus at any confining pressure in triaxial tests. This result contradicts with coal behavior, as explained before.
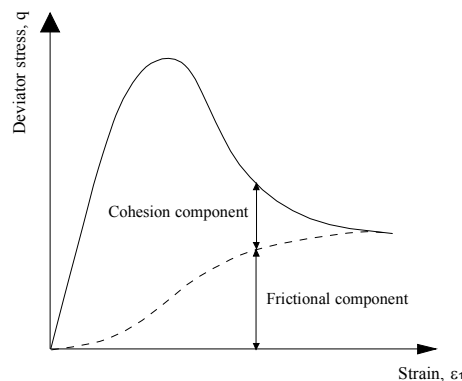
Figure 3-8 Friction hardening vs. cohesion softening for coal material

To express the increase of the frictional component during material deformation, a strain-dependent quantity α*, referred to as the mobilized angle of friction, will be used. The mobilized angle of friction gradually increases with strain. It reaches the limit angle of friction when the plastic strain has reached a constant value (Figure 3-8). Hansen [1965] developed many formulas expressing such behavior.

Introducing both of the mobilized cohesion k^* and the mobilized angle of friction α^*, the Drucker-Prager yield function can be expressed as:

$$f \equiv \alpha^* J_1 + \sqrt{J_{2D}} - k^* = 0 \qquad\qquad \textbf{Equation 3-9}$$

3.2.1.2 Coal model Verification

The linear Drucker-Prager model with the mobilized angle of internal friction Equation (3-9), was verified by conducting a number of FE models simulating the uniaxial and triaxial compression tests. The effect of confining pressure on the behavior of coal model was tested by simulating the triaxial compression test. The effect of pillar width-to-height ratio was studied by simulating the uniaxial compression tests of specimens of different width-to-height ratios.

♦ **Triaxial test for coal material**

The FE model simulated a simple triaxial test of an axisymmetric coal sample compressed between two smooth platens, one of which is held fixed and the other has prescribed vertical motion. The coal specimen is first loaded by constant pressure σ_3; e.g. 0, 200, 500, 1000, 1500, 2250, 3000, 4000, 5000 psi. Then the top platen is moved downward to compress the specimen. Figure 3-9 defines the model geometry.
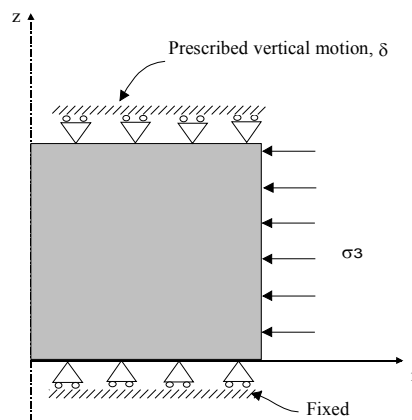
Figure 3-9 Triaxial compression test with smooth platens

Based on the above study, a rectilinear stress-strain curve (Figure 3-10) has been proposed to simulate the in-situ compression test of coal material. The typical Drucker-Prager parameters for coal material are given in Table 3-1. The coal residual strength is assumed to follow Mogi [1971] criterion given by Equation (3-7). So the residual friction angle α_r is estimated to be 53.13 degrees and the brittle-ductile transition confining pressure is 2250 psi.

Table 3-1 Typical coal properties used in FE models

Parameter	Value
Elastic modulus E, psi	$3.5*10^5$
Poisson's ratio ν	0.3
Peak strength σ_c, psi	900
Residual strength σ_r, psi	4.8
Post-peak stiffness K_p, psi	$7.0*10^5$
Initial friction angle α_i, degree	50.19
Residual Friction angle α_r, degree	53.13

For the sake of simplicity, the friction hardening is simulated by linearly increasing the friction angle with respect to the plastic strain. On the other hand the cohesion softening is obtained by linearly reducing the cohesion with respect to the plastic strain (Figure 3-11).
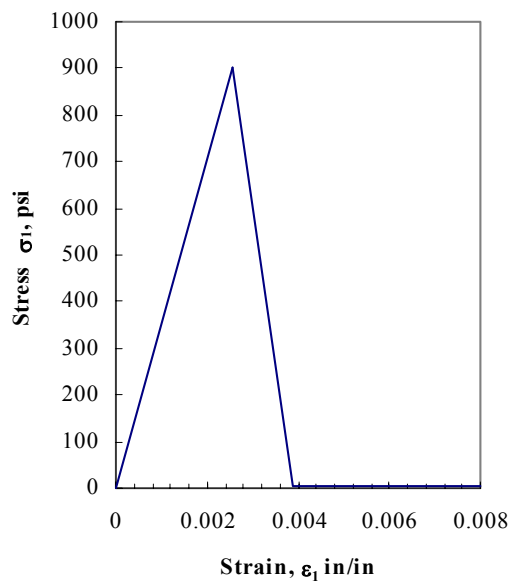
Figure 3-10 Rectilinear stress-strain curve for coal model
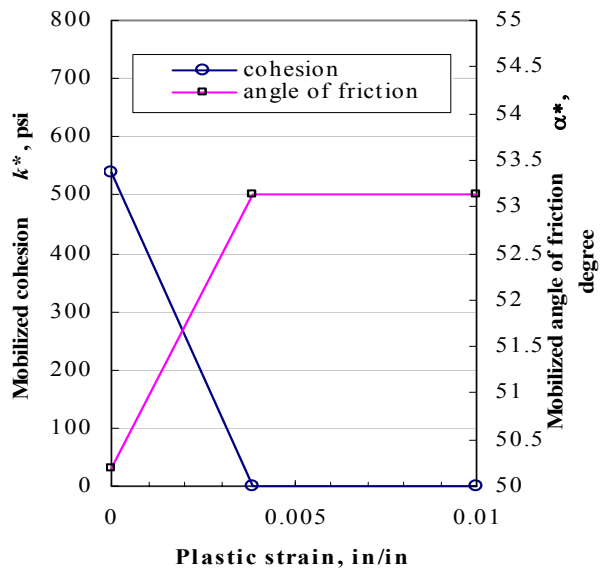
Figure 3-11 Strain softening parameters used for the simulations

To illustrate the importance of mobilizing the angle of friction in the Drucker-Prager model, two types of FE models are conducted subjected to the same boundary conditions. The first type represents the Drucker-Prager model (Equation 3-8) with constant friction angle of 50.19 degrees while the second type represents the Drucker-Prager model (Equation 3-9) with mobilized angle of friction.

Figure 3-12a shows the estimated deviator stress-stain curves of coal specimen under different confining pressures using the Drucker-Prager model with constant angle of friction. It is obvious that this model doesn't satisfy two important characteristics of typical coal model: first, the post-peak stiffness is observed to be independent of the confining pressures; second, the model doesn't show a transition from brittle to ductile behavior even at a high confining pressure of 5000 psi.

a   **b**
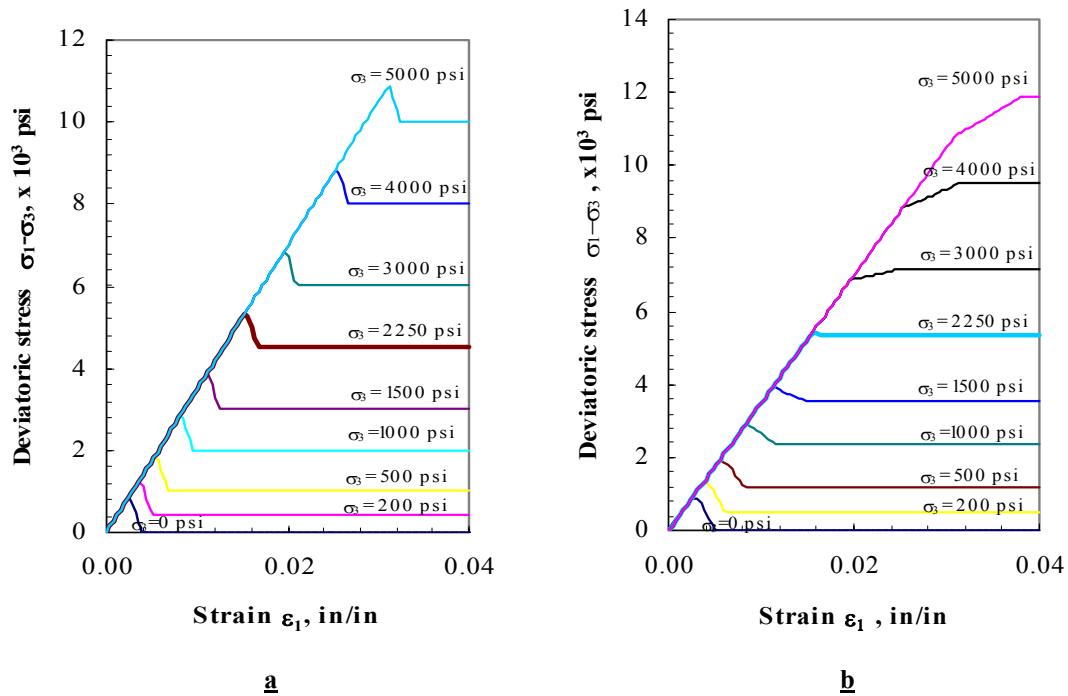
Figure 3-12 Simulation results of triaxial tests for Drucker-Prager model with
a. Constant angle of friction.
b. Mobilized angle of friction

Figure 3-12b shows the estimated deviator stress-stain curves of coal specimen under different confining pressures using Drucker-Prager model with mobilized angle of friction. Figure 3-13 shows that the Drucker-Prager model with mobilized angle of friction model was able to show both the hardening and softening behaviors of coal specimen under different confining pressures. Figure 3-12b shows that the post-peak stiffness of the specimen turned to be positive at the pre-defined brittle-ductile confining pressure of 2500 psi. Because the effect of friction angle mobilization starts once the specimen begins to yield, there are no differences between the peak strengths predicted by both types of Drucker-Prager model (Figure 3-14). On the other hand, Figure 3-14b shows that Drucker-Prager model with fixed angle of friction showed smaller residual strengths compared with the one with mobilized angle of friction.
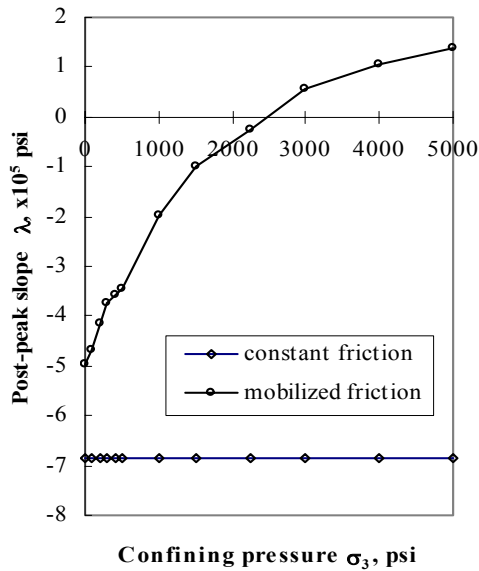
Figure 3-13 Estimated Post-peak stiffness vs. applied confining pressures
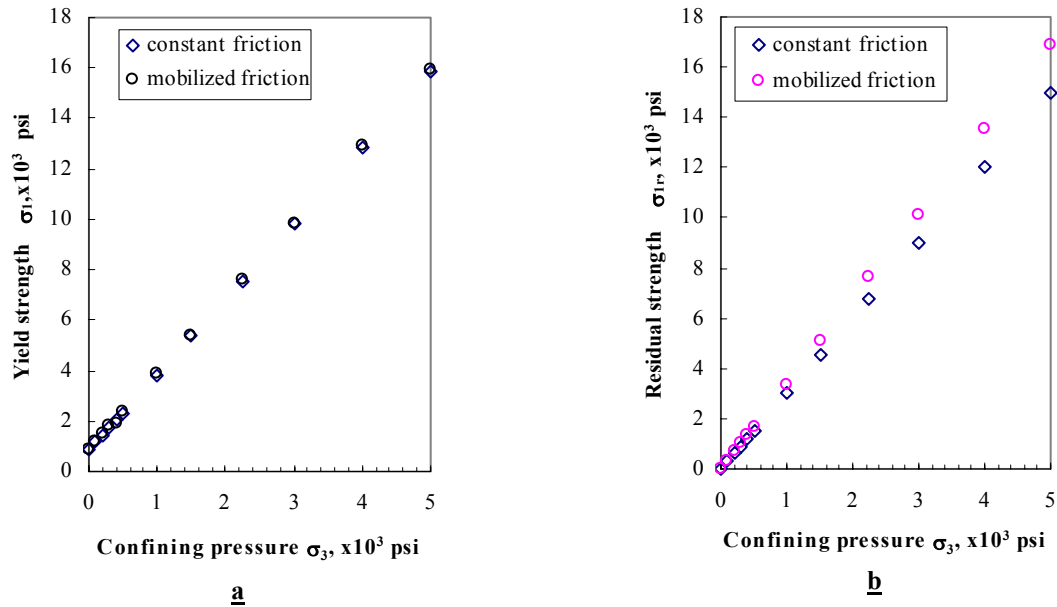
Figure 3-14 Estimated residual strength curves

a. Constant angle of friction.

b. Mobilized angle of friction

♦ **Uniaxial test for coal material**

The FE simulation of uniaxial test is used to study the effect of specimen's width-to-height ratio on its deformation characteristics. Drucker-Prager model with mobilized angle of friction was used in the simulation. The coal properties defined in Table 3-1 have been used in this study. Axisymmetric coal samples of 2 inches diameter with different heights 2, 4, 6.16, 8, 10, 13.34, 16 and 20 inches, are compressed between two steel platens, one of which is held fixed and the other is moved according to the prescribed vertical motion. A friction angle of 14° has been assigned between the coal sample and the steel platens. The specimen grid was generated with 0.05-inch square elements. The maximum loading rate during the test was .0004 inch/sec. Figure 3-15 defines the model geometry and boundary conditions.
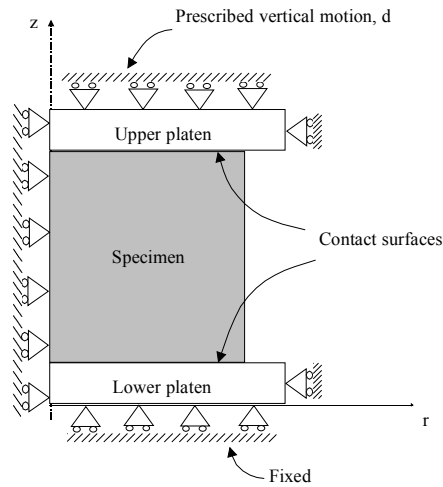
Figure 3-15 Uniaxial compression test with regular platens

Figure 3-16 shows the Von-Mises stress distribution in the modeled specimen. The figure shows that the maximum shear was concentrated along the specimen diagonals forming the typical cone failure observed in laboratory tests.
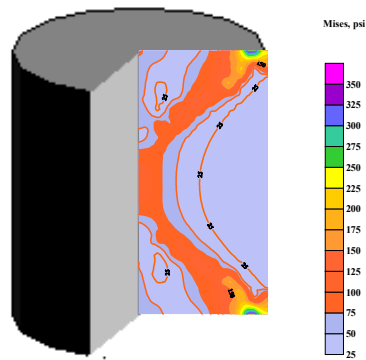
Figure 3-16 Specimen shear failure

Figure 3-17 shows the estimated stress-strain curves for coal specimens with different width-to-height ratios using the Drucker-Prager model with mobilized angle of friction. The model was able to show the coal material independency of the Elastic modulus. The specimen's softening behavior was obvious at small width-to-height ratios, up to 4, while it shows a hardening behavior at high width-to-height ratio of 10. The

model shows the reconsolidation behavior reported by Das [1986] at a width-to-height ratio of 6.67.
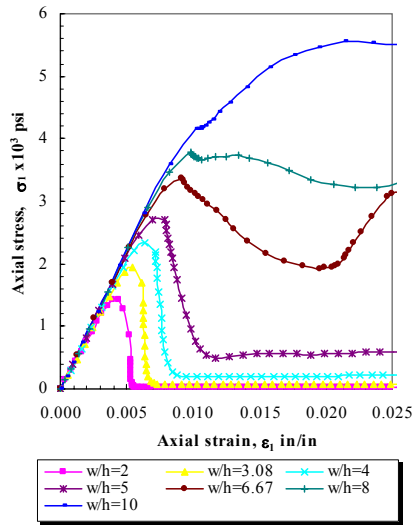
Figure 3-17 Estimated stress-strain curves at different width-to-height ratios

The post-peak stiffness (maximum slope after peak-strength) was calculated from the stress-strain curves and plotted against the width-to-height ratio as shown in Figure 3-18. The post-peak stiffness was decreasing with increasing specimen width-to-height ratio and it becomes around zero at width-to-height ratio of 10.
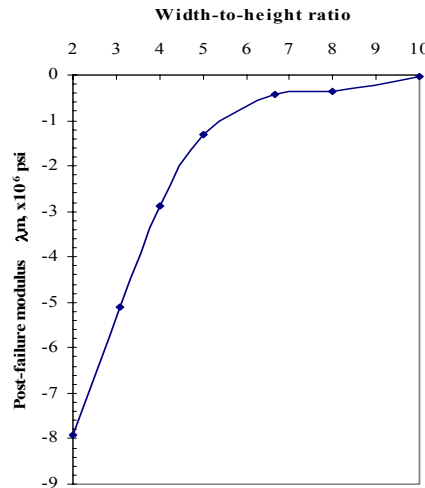
Figure 3-18 Estimated post-peak stiffness vs. the width-to-height ratio

Figure 3-19 shows the estimated peak strengths at different width-to-height ratios. The figure shows the strengthening effect of specimen width-to-height ratio, where the specimen peak strength increases with increasing specimen width-to-height ratio. The estimated peak strengths were compared with Bieniawski's strength formula. Assuming in-situ strength of 900 psi, Bieniawski strength formula predicated smaller peak strengths compared with the estimated peak strengths. The Bieniawski strength formula showed good agreement with FE prediction if the assumed value of in-situ strength increased to 1100 psi.
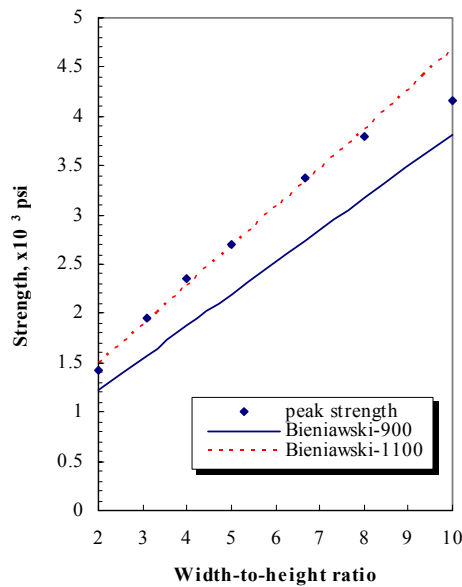
Figure 3-19 Estimated peak strength vs. width-to-height ratio

Figure 3-20 shows the estimated residual strengths at different width-to-height ratios. The figure shows the slow change of residual strength at low width-to-height ratio, less than 5, and the rapid change at higher width-to-height ratios. The observation matches to some extent with Das [1986] that the pillar residual strength increases exponentially with increasing width-to-height ratio
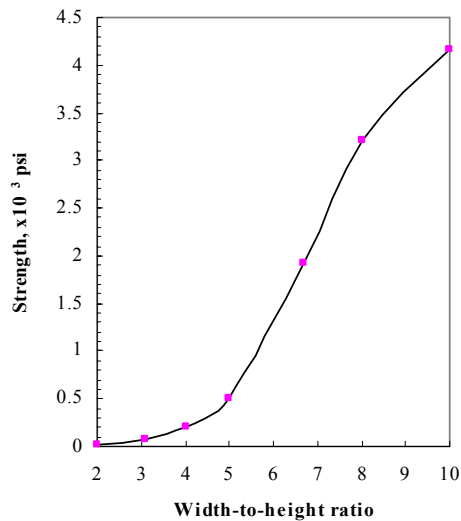
Figure 3-20 Estimated residual strength vs. width-to-height ratio

3.2.2   Gob model

The behavior of the longwall gob is very critical in the understanding of the complex ground response to longwall mining. In the limited data available, the values of gob moduli used in numerical modeling ranged from 1,000 psi to over 300,000 psi. Such a wide variation in moduli would greatly affect the results of the numerical analysis. A better understanding of the behavior of the gob will allow numerical models to be more accurate for simulating longwall mining conditions.

In this study, a gob model based on the Terzaghi's compaction model was incorporated into the comprehensive finite element package, ABAQUS, to simulate the loading behavior of longwall gob material. A case study was used to verify the proposed gob model.

As the longwall face moves forward, shields are advanced and the roof is allowed to cave behind the face. As the roof falls, the volume of caved materials or gob expands upward until it comes in contact with the sagging roof strata. As a result, the following five distinct stress zones may be defined (Figure 3-21).

Zone I -   Undisturbed area of coal seam;

Zone II -   Region of front and side abutment pressures;

Zone III- The exposed area between the face and gob;

Zone IV- The transition region in the gob area in which the broken   strata is being compressed, and the degree of compaction increases with increasing distance from the face line;

Zone V - The region where the gob is fully compacted and the gob pressure equals to the primary (virgin) stress.
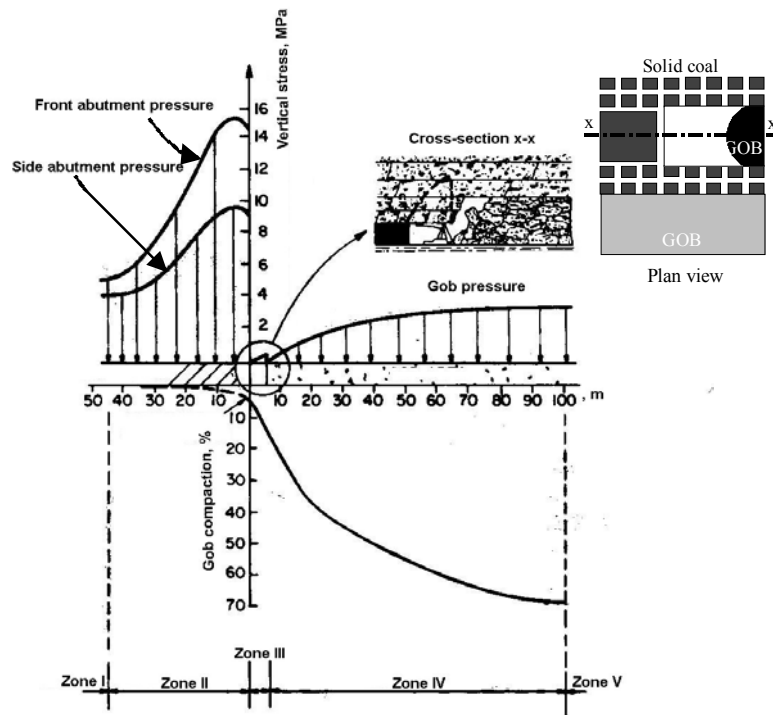
Figure 3-21 Distribution of strata pressure in the vicinity of the longwall face, (modified from Unrug et. al., 1982)

Peng et al., [1980] performed three-dimensional finite element analysis to study the supporting role of the gob materials. The materials used in these models were assumed to be isotropic, homogeneous, and elastic. They divided the gob into three major zones:

♦ Well-packed zone which is the center portion of the gob;

    ♦ Packed zone which is on both sides of the well packed zone;

    ♦ Loosely packed zone which is between the packed zone and rib sides.

They found that the front and side abutment pressures are reduced considerably due to the support offered by the gob. However they also found that the reduction of abutment pressure is not sensitive to the degree of packing of the gob material, the height of caving, and the height of the fractured zone as long as the gob materials offers support to the overlying strata. Based on these findings, they used a "rule of thumb" for estimating the gob modulus which was estimated to range from 1/100 to 1/57 of the intact roof rock modulus depending upon how well the gob was packed.

3.2.2.1 Gob Pressure

At the start of coalface retreat operation, when the roof rocks start to cave in the gob, only the weight of the caved material will form the gob pressure. Also, a pressure arch will develop across the solid coal on both sides of the panel and a de-stressed zone above the gob area will be developed. As the longwall face retreats and the caving process continues, the caved materials pile up and the dimensions of the pressure arch increase. When the width of the pressure arch reaches the "maximum width" over which the main roof load can no longer be transferred to the solid coal perimeters, the main roof breaks. After this first break, the thickness of the loose caved rocks on the floor increases with the increase in the mined-out span. Ultimately, due to the combined effect of bulking, roof sag, and floor heave, the caved material comes into contact with the roof and takes load from the upper strata. As the mining progresses further, the roof is lowered more firmly on the caved material. This roof settlement causes the gradual compaction of

the gob material. Experience shows that once the extracted span is fairly large, the caving, re-compaction and roof sagging often progresses in repeatable cycles while the longwall face retreats.

Whittaker [1974] found that the gob pressure builds up until the cover load is reached at a distance of 0.3-0.4 time the seam depth from the solid abutments. Wilson [1982] assumed that the gob pressure is redistributed linearly across the active gob with zero stress at its edge and increasing to the original cover pressure at a distance of 0.2-0.3 times the overburden depth.

Whittaker and Singh [1979] indicated that the gob pressure starts to build up at a distance of 120 ft behind the face, and that it does not reach the cover load even after the face has advanced for a distance equal to the mining depth. Whether the gob pressure reaches the overburden pressure or not depends mainly on the panel width. If the panel is too narrow, the upper unbroken strata will be bridged between side abutments on both sides of the panel resulting in gob pressure being more or less the weight of rock up to the caving height.

Trueman [1990] performed two-dimensional finite element analysis to study the behavior of longwall coal mining gob material. He concluded that at a given geologic condition, the cover load would be reached in the gob at a fixed distance irrespective of mining depth. Also, he found that this distance mainly depends on the caving height.

Field measurements of gob loading have been conducted under varying sets of geological conditions. Campoli et al., [1993] investigated the longwall gob behavior in the 2,200 ft deep Pocahontas No. 3 coal seam. The floor pressure measurements showed a return to full overburden pressure at approximately 0.2 time the overburden depth. In a South African potash mine, Oyanguren [1972] concluded that at a distance of about 0.9 time the depth of overburden behind the face, the ground above the longwall gob was stabilized and the pressure on the gob floor had reached the overburden pressure.

3.2.2.2 Terzaghi's Model of Gob Material

Although the material making up the gob is the same as the immediate roof strata, the environment is different and the gob material can be considered as a different material from the in-situ rock and acts differently. Several authors have attempted to quantify the properties of gob material [Pappas and Mark, 1993].

Generally speaking, the gob material is strain hardening, i.e. the modulus of deformation increases with increasing compaction. There are two models available that can describe the hardening behavior of the gob material, namely; Salamon's model [Salamon, 1990] and Terzaghi's model [Pappas and Mark, 1993].

Terzaghi's approach assumes that the tangent Young's modulus of the granular material is a linear function of the applied normal stress.

$$E_t = E_o + a\sigma \qquad\qquad \textbf{Equation 3-10}$$

where E_t is tangent Young's modulus; σ is the normal stress; "a" is a constant; and E_o is the initial modulus.

$$E_o = R_o E_i \qquad\qquad \textbf{Equation 3-11}$$

where, R_o is a constant.

The differential equation between normal stress σ and normal strain ε is

$$d\sigma = E_t d\varepsilon \qquad\qquad \textbf{Equation 3-12}$$

Combining Equations 3-10 and 3-12 yields

$$d\varepsilon = \frac{d\sigma}{R_o E_i + a\sigma} \qquad\qquad \textbf{Equation 3-13}$$

Integrating Equation 3-13 yields

$$\varepsilon = \frac{1}{a}\ln(R_oE_i + a\sigma) + c$$

Equation 3-14

where c is the constant of the integration and can be determined using the following initial condition:

$$\sigma = 0 \text{ at } \varepsilon = 0;$$

Equation 3-15

Hence;

$$c = -\frac{\ln(R_oE_i)}{a}$$

Equation 3-16

$$\varepsilon = \frac{1}{a}\ln\left(1 + \frac{a}{R_oE_i}\sigma\right)$$

Equation 3-17

Rearranging Equation 3-17, the following stress-strain relation for the gob material is obtained:

$$\sigma = \frac{R_oE_i}{a}\left(e^{\varepsilon a} - 1\right)$$

Equation 3-18

Pappas and Mark [1993] evaluated the behavior of gob material experimentally. Comparing Terzaghi's model (Equation 3-18) with laboratory data, they concluded that this model could fairly describe the compressive behavior of gob material.

3.2.2.3 Implementation of Terzaghi's Model in FE Models

To define the Terzaghi's model (Equation 3-18) the constant "a" should be determined. Solving Equation 3-18 in terms of the secant modulus E_s:

$$E_s = \frac{\sigma}{\varepsilon} = \frac{a\sigma}{\ln\left(1 + \frac{a}{R_oE_i}\sigma\right)}$$

Equation 3-19

It is assumed that the virgin stress σ_v could be recovered in the compacted region of the gob. Therefore the secant modulus of compacted gob $E_{s,v}$ subjected to the virgin stress σ_v, can be expressed as follows:

$$E_{s,v} = \frac{a\sigma_v}{\ln\left(1 + \frac{a}{R_o E_i}\sigma_v\right)}$$

Equation 3-20

The secant modulus $E_{s,v}$ will be estimated as follows

$$E_{s,v} = \frac{nH\sigma_v}{\delta}$$

Equation 3-21

where n is the gob height factor which is the ratio between the gob height to the mining height, H; and δ is the maximum gob compaction in unit length.

Combining Equations 3-20 and 3-21, the constant "a" can be determined iteratively from the following expression:

$$a = \frac{nH}{\delta} \times \ln\left(1 + \frac{a}{R_o E_i}\sigma_v\right)$$

Equation 3-22

In order to define the Terzaghi's model for gob elements in the finite element models, the stress-strain curve is divided into "n" points (Figure 3-22). At any point $k(\varepsilon_k, \sigma_k)$, the secant modulus $E_{s,k}$ is evaluated using Equation 3-19 and the corresponding strain energy density W_k is determined by:

$$W_k = \frac{1}{2}\varepsilon_k\sigma_k$$

Equation 3-23

The parametric relationship between the strain energy and secant modulus for gob elements (Figure 3-23) can be defined for the gob elements.
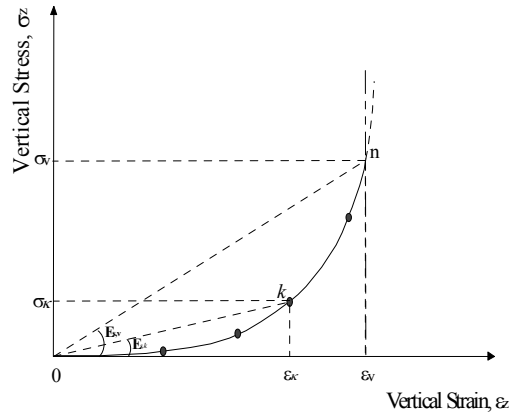
Figure 3-22 Stress-strain relationship for Terzagh's model
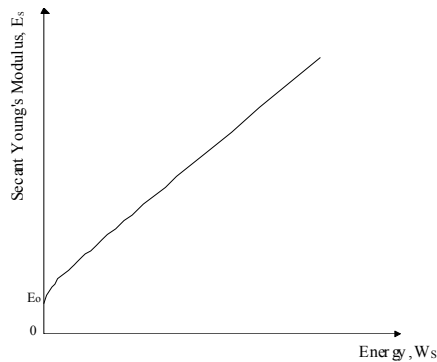
Figure 3-23 Strain energy density vs. secant Young's modulus for Terzaghi's model

Figure 3-24 shows the algorithm to update the secant modulus of gob material. An initial modulus will be assigned for the gob elements. The model will be loaded (solved) in steps. A small fraction of total load will be applied at each step. During the model solution, the parametric relationship (Figure 3-23) will be used to update the modulus of elasticity of gob elements according to their strain energies. The strain energy density of the gob elements are estimated based on the current applied stresses, as follows:

$$W = \frac{1}{2E_s}\left[\sigma_1^2 + \sigma_2^2 + \sigma_3^2 - 2\nu\left(\sigma_1\sigma_2 + \sigma_2\sigma_3 + \sigma_1\sigma_3\right)\right]$$ **Equation 3-24**

where σ_1, σ_2 and σ_3 are maximum, intermediate and minimum principal stresses, respectively
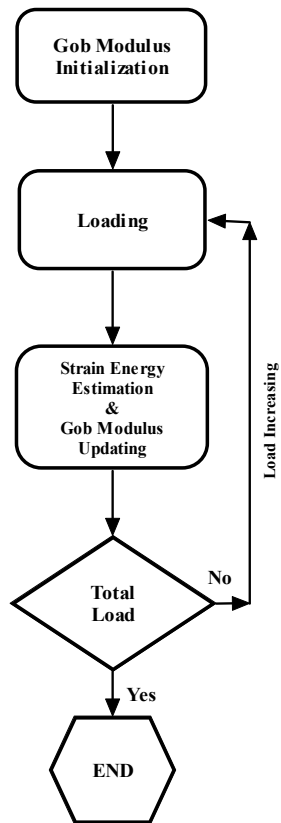
Figure 3-24   Algorithm for gob modulus updating

3.2.2.4 Case Study

A longwall mine located in Buchanan County, Virginia (Figure 3-25) was used to verify the proposed gob mode. Several panels in this mine had been extensively instrumented for bump analysis [Campoli et al., 1993]. The study area is located at the gateroad system between the 9th and 10th panels South (Figure 3-25).

The mine extracts the Pocahontas No. 3 Coalbed, which averages 5.5 ft in thickness. In the study area, the average overburden depth is 2,200 ft. The immediate roof consists of a widely jointed siltstone overlain by very stiff massive sandstone. The siltstone is 60 ft and the sandstone ranges from 210 ft to 230 ft thick. The mine floor consists of a combination of very competent siltstone and sandstone. The horizontal

principal stresses are approximately 3,400 psi and 1,500 psi in the north-south and east-west directions, respectively.
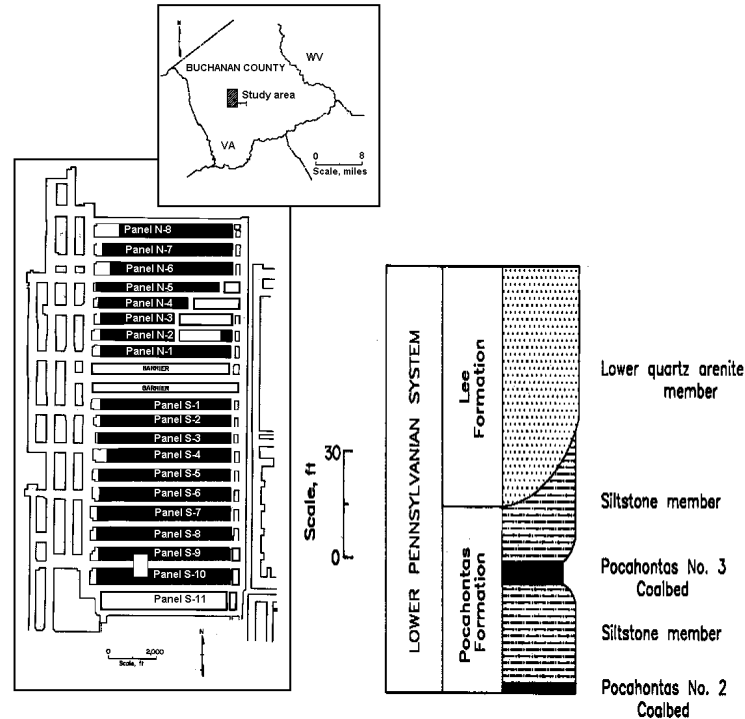
Figure 3-25 Pocahontas No. 3 mine [Campoli, et al., 1993]

The longwall panels associated with this study were 600 ft wide by 6,000 ft long, and developed using 4-entry yield-abutment-yield pillar system. The gateroad system was 238 ft wide consisting of a 20 ft x 80 ft yield pillar on either side of a 120 ft x 180 ft abutment pillar.

As part of a detailed instrumentation study in this mine [Campoli et al., 1993], a total of eighteen 3-in diameter BPF's were installed in the floor below panels S-9 and S-10. All these instruments were on a line approximately 3,800 ft from the setup rooms of panels S-9 and S-10 (Figure 3-26). The longwall gob floor loading was monitored throughout the whole panel S-9 when it was being mined and stopped after panel S-10 had passed the measuring station by 60 ft.
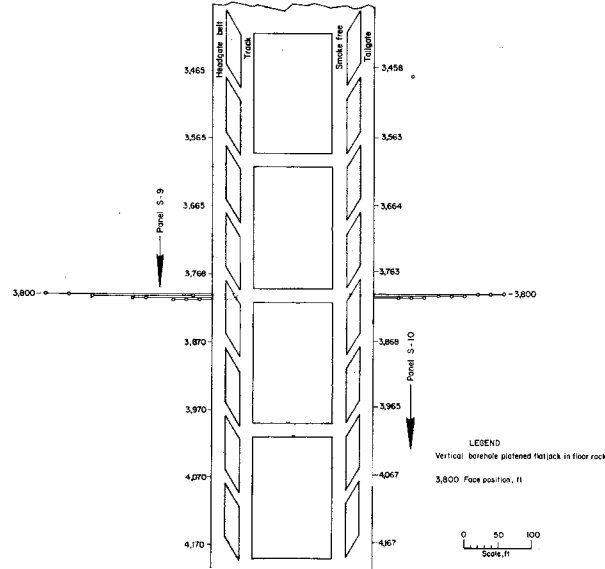
Figure 3-26 Underground study area [Campoli et al., 1993]

♦   **Finite Element Model**

Three-dimensional finite element models with 8-node brick elements and six-node tetrahedron elements were used throughout all the analysis. The FE model consisted of half of panel S-9 and S-10 and the gateroad system.

The dimension of the model was 840 ft x 930 ft x 550.5 ft (Figure 3-27). All the four side boundaries and the bottom boundary of the model were roller-constrained. A large number of elements and nodes (48,692 and 50,048, respectively) were used in the model. Linear elastic material properties have been assigned for the model except for the gob material. The gob height was predefined to be 6 times the seam thickness.

The gob model parameters (n, a, R_o and δ) are selected to ensure that the virgin stress σ_v is approximately recovered at a distance of 0.2-0.3 of the overburden depth from the panel ribs. A try and error approach was used to define the gob parameters ($n = 6$, $a = 354.57$, $R_o = 0.001$ and $\delta = 0.4884$ ft).

Thick., ft	Rock type	Young's Modulus, x 1E6 psi	Poisson's Ratio	Density lb/cu ft
200	Sandstone	7.67	0.089	162
20	Shale	6.64	0.155	168
40	Sandy shale	4.55	0.361	165
5.5	Coal	0.50	0.340	82
10	Sandy shale	4.55	0.361	165
75	Sandstone	7.21	0.170	162
200	Sandstone	7.78	0.185	162

$\sigma_x = 1.392\,\sigma_z$

$\sigma_y = 0.651\,\sigma_z$

σ_z = vertical stress
σ_x and σ_y = horizontal stresses
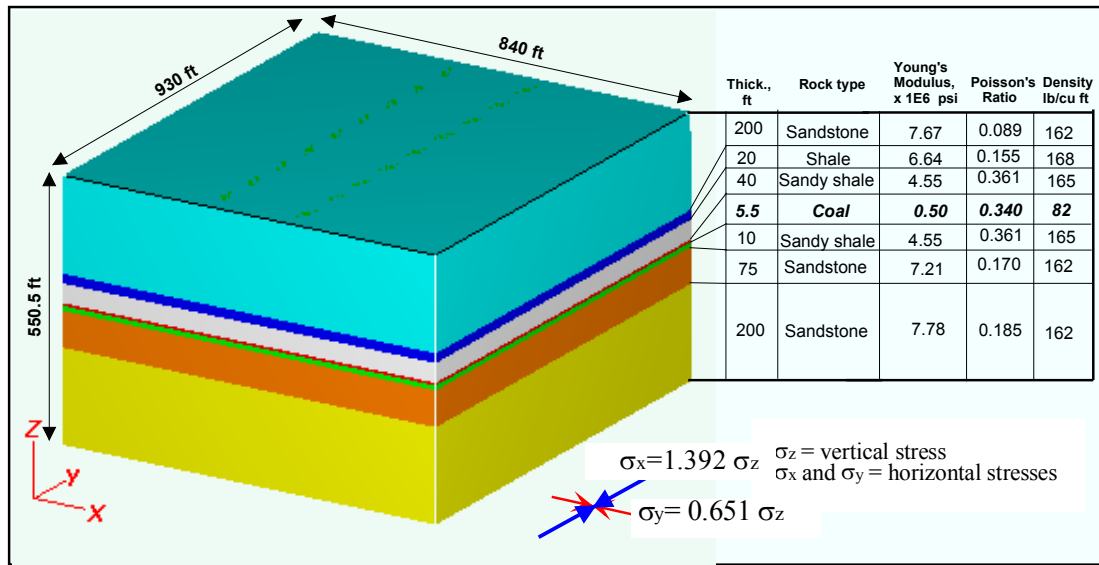
Figure 3-27 3D model with mechanical properties of the rocks

The model was solved in thirteen steps. In the first step, the gob elements were deactivated and the geostatic stress condition was applied. The gateroads were developed in the second step. Steps No. 3 to 8 and Steps No. 9 to 13 were assigned to simulate the activation of gob material and longwall retreat of panel S-9 and panel S-10, respectively. The retreat plan is shown in Figure 3-28.
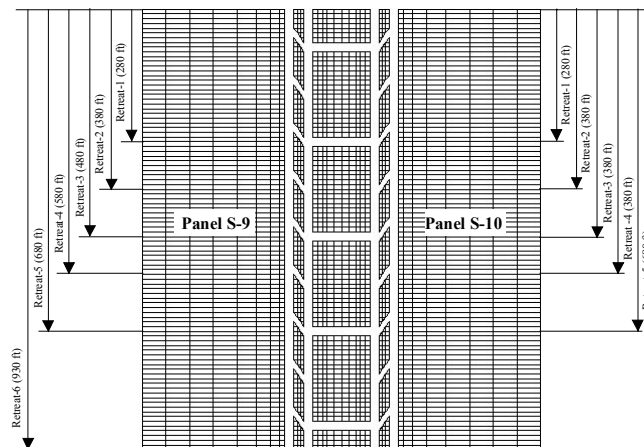
Figure 3-28   Retreat plan for longwall panels S-9 and S-10

♦ **Analysis and Discussions**

The analysis of the FE model results was conducted in three stages. In the first stage, a detailed analysis was conducted for the gob behavior at retreat step No.5 of panel S-9 (Figure 3-28). In the second stage the gob stress distribution was analyzed during the retreat of panel S-9 and panel S-10. In the last stage, a comparison between the in-situ measurements and FE model results was conducted.

.Figure 3-29 shows the stress-strain curve obtained by the ABAQUS simulation for a gob element at the center of panel S-9 at retreat No. 5. The simulated stress-strain curve shows a good agreement with the proposed gob model.
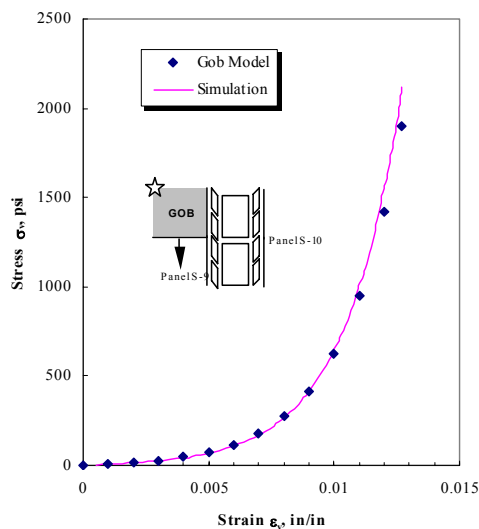
Figure 3-29   Simulated stress-strain curve and the proposed gob model

Figure 3-30 shows the distribution of the gob vertical stress along a longitudinal section x-x at the center of panel S-9 for retreat No. 5. It shows that the 80% of the virgin stress has been recovered at a distance of 400 ft from the face.
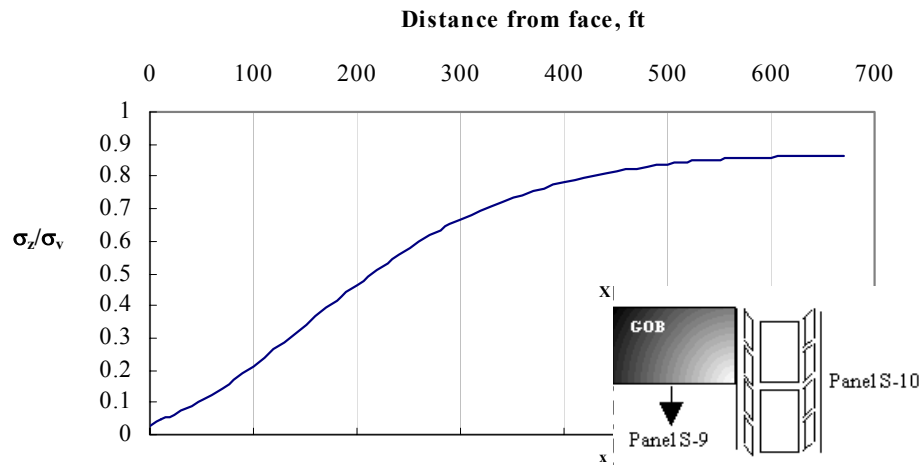
Figure 3-30 Distribution of vertical stress along cross section X-X

Figure 3-31 shows the contour lines of vertical stress in the gob area of panel S-9 at different stages of longwall retreating. It shows a rapid increase in vertical stress from the start of the longwall mining until retreat step No. 3. Thereafter, the change in gob stress was small. Also, it shows the gob stress at the face and gateroad sides is approximately zero and builds up toward the center of the gob.

Figure 3-32 shows the contour lines of vertical stress of panel S-10 at different stages of longwall retreating. The same gob behavior as that of panel S-9 was observed in panel S-10, i.e. it changed very little. No significant change in the gob loading of panel S-9 is observed during the mining of panel S-10. This could be due to the elastic behavior which was assumed for the pillar system.
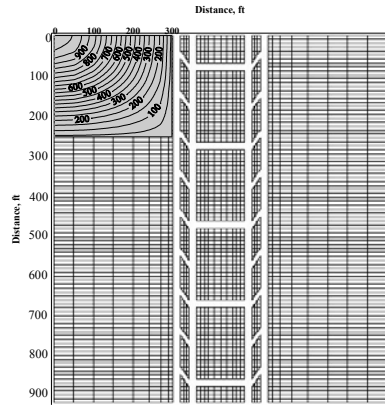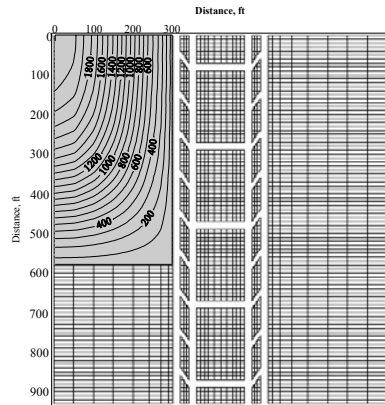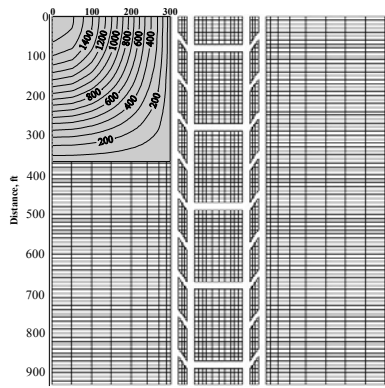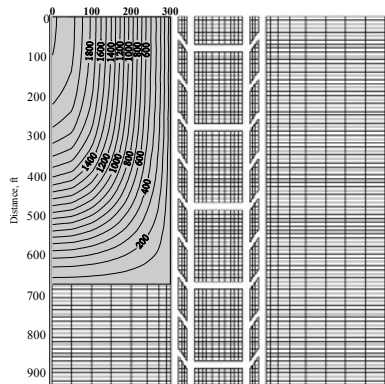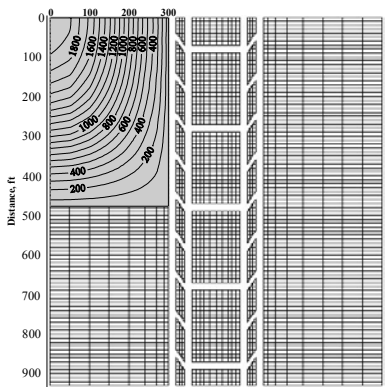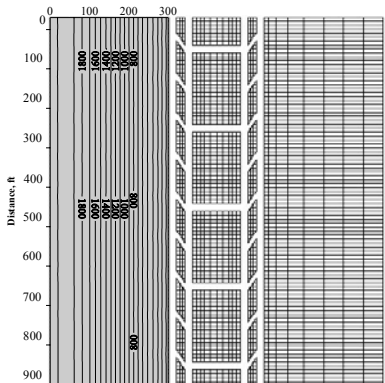
Figure 3-31 Vertical stress contours in gob area of panel S-9, (stresses are in psi)
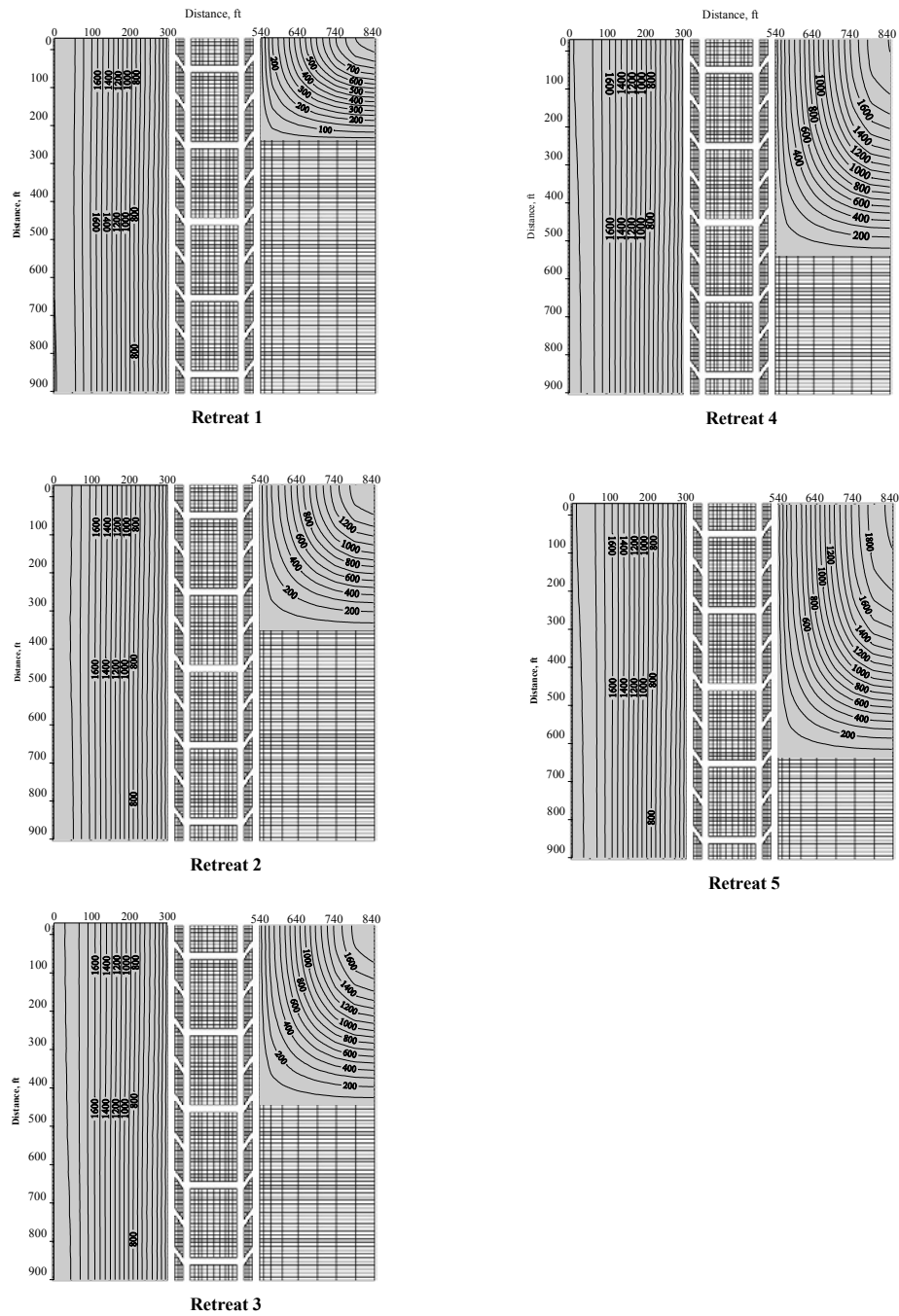
Figure 3-32   Vertical stress contours in gob area of panel S-10 (stresses are in psi)

In spite of the discrepancy existed in the monitored in-situ loading of longwall gob floor of panel S-9 and panel S-10, this was an excellent set of data for verification of the proposed gob model. Since the measured in-situ stresses were strongly affected by the orientation of BPF, the estimated values of the maximum and minimum principal stresses were used to show the upper and lower limits of the floor stress. Figure 3-33 shows a comparison between the measured and predicted floor stresses when the face of panel S-9 passes the monitoring stations. It shows a good agreement between the measured stresses and the estimated vertical stresses, except for three stations; 58 ft, 89 ft and 248 ft from the headgate. Except the station at 58 ft from the headgate, the vertical stresses at all other stations were within the limits of principal stresses.
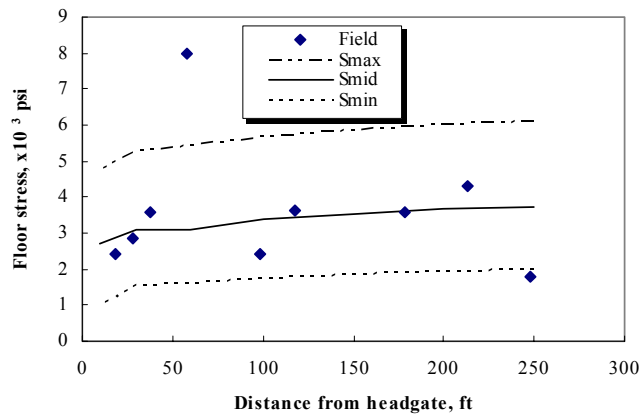
Figure 3-33 Vertical stress profiles under panel S-9

Figure 3-34 shows the peak stress recovery under panel S-9 that increases as the distance from the headgate increases. Figure 3-34 illustrates that the measured vertical stress recovery is within the limits of principal stresses. Figure 3-35 shows the floor stress at different longitudinal sections during the mining of panel S-9. It shows that the front abutment peak load did not occur at, but within 100 ft from, the face location. In Sections A and D, 28 ft and 248 ft from the headgate of panel S-9, respectively, the measured floor stresses were very close to the estimated minimum principal stresses. For Section B at 89 ft from the headgate of panel S-9, the measured floor stresses were in the range of the

estimated vertical stresses and the minimum principal stresses. Finally, in Section C the measured floor stresses at a distance of 178 ft from the headgate were within the range of the estimated vertical stresses and the maximum principal stresses.
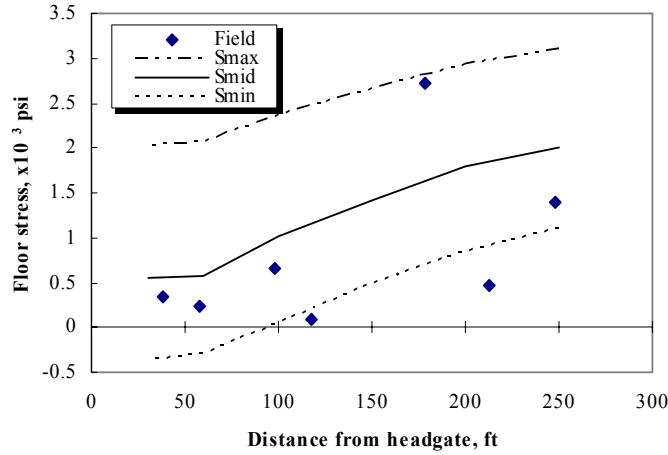
Figure 3-34 Peak stress recovery under panel S-9 during the retreat of panel S-9
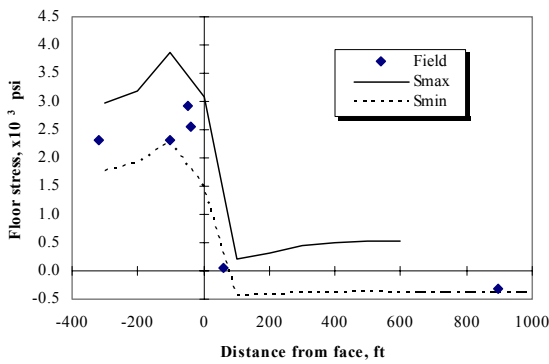
Section A (28 ft from the headgate of panel S-9)
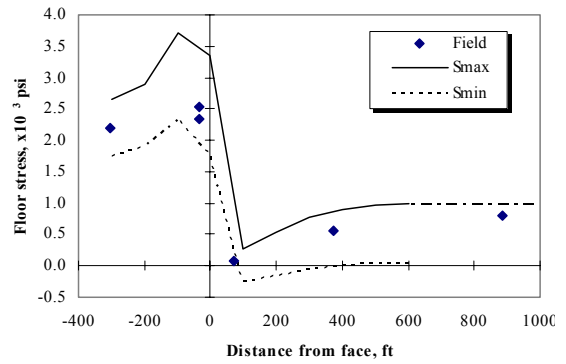
Section B (89 ft from the headgate of panel S-9)

Figure 3-35   Vertical stress under panel S-9 during the retreat of panel S-9
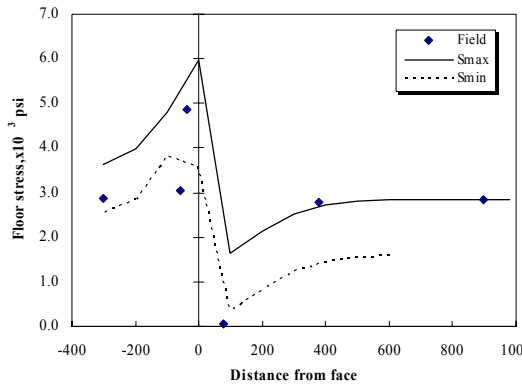
Section C (178 ft from the headgate of panel S-9)   Section D (248 ft from the headgate of panel S-9)
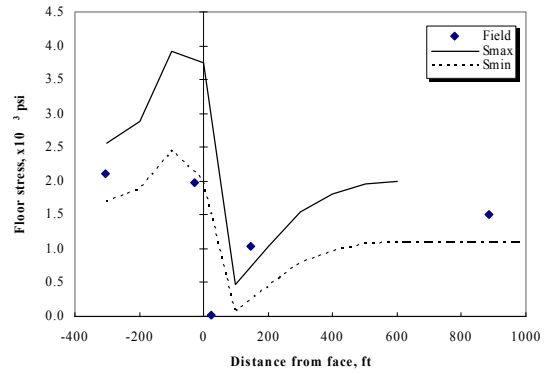
Figure 3-35   Continue

Unfortunately, the monitoring of floor stresses under panel S-10 was incomplete. Only a monitoring distance of 100 ft was recorded before the face reached the measurement stations and 30 ft of monitoring distance was recorded after the face passed the measurement stations. Figure 3-36 shows a comparison between the measured and predicted floor stresses when the face of panel S-10 passed the monitoring stations. It shows that the measured floor stress was close to the estimated vertical stresses, except for a station at a distance of 38 ft from the tailgate of panel S-10. This station showed a much higher stress than the estimated maximum principal stress.
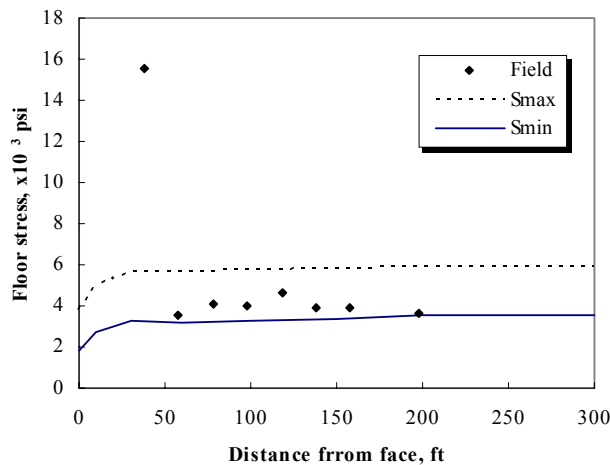
Figure 3-36 Vertical stress under panel S-10

3.3 New approach to estimate the Local Mine Stiffness

Starfield and Wawersilk [1968] introduced the Local Mine Stiffness (K_{LMS}) concept to explain the violent failure of pillars. The K_{LMS} concept can be explained by considering a hypothetical situation (Figure 3-38A) in which a pillar is replaced by a hydraulic jack. Initially, this jack is pressurized sufficiently high to prevent roof convergence. As the jack is slowly released, the force imposed on it will drop because more loads are transferred to the adjacent pillars. As the jack force is released, roof sagging and floor heaving occurs at the jack location. While the roof remains intact, a linear relation between the jack force and the roof-to-floor convergence could be assumed (Figure 3-37B). The slope of this line is called the Local Mine Stiffness, K_{LMS}.
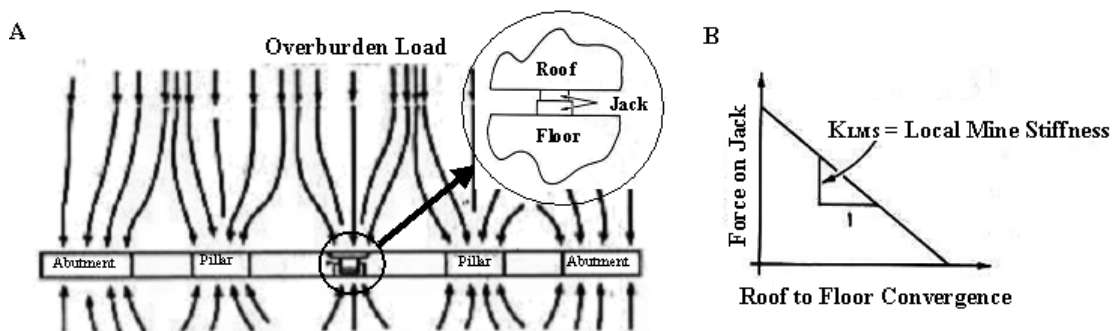
Figure 3-37 Illustration of Local Mine Stiffness Concept

A. Hydraulic jack replaces a coal pillar;

B. K_{LMS} is the slope of jack force versus the roof-to-floor convergence

There are two approaches for estimating the K_{LMS} at a pillar site: the analytical approach developed by Salamon [1970] and the numerical approach (perturbation method) proposed by Starfield and Wawersik [1968]. These approaches consider the pillar and surrounding strata to be homogeneous, isotropic and linear elastic. Also, it is assumed that the stress within the pillar is uniformly distributed.

In order to estimate the K_{LMS} at a specific pillar site, the effect of the hypothetical experiment proposed by Starfield and Fairhurst [1968] (Figure 3-37A) is numerically simulated using the finite element approach. It is assumed that a pillar could be replaced by a series of hydraulic jacks. The number of jacks should be large enough so that the load and roof-to-floor convergence could be assumed uniform at each jack. These jacks exert different forces to the roof and floor depending on their locations within the pillar. By removing the pillar (releasing the jacks), the finite element program ABAQUS [ABAQUS, 1998] first applies the forces that the pillar is exerting on the roof and floor at the nodes of interface. These forces are then ramped down gradually to zero during the pillar removal process. During the pillar removal process the vertical stresses and displacements are monitored for the immediate roof and floor at the location of the removed pillar. At each jack location, which is represented by two vertically aligned nodes; the K_{LMS} is determined by the slope of the relation between the recorded stresses and the roof-to-floor convergences divided by seam height.

The numerical method used to evaluate the K_{LMS} was tested against the analytical solution of a simple case provided by Salamon [1970]. This case assumes a panel of five long pillars in elastic homogeneous isotropic infinite medium. The pillar height and width are 5 ft and the entry width is 5 ft. The overall dimension of this problem is shown in Figure 3-39.

A two-dimensional isoperimetric quadrilateral plane strain finite element model was used to simulate this panel. A large number of elements and nodes (96,800 and 97,461, respectively) were used in this model. The smallest element size in the areas of interest is 0.25 ft x 0.11 ft. The boundary conditions and the material properties used in this model are presented in Figure 3-38. Because of model symmetry, the K_{LMS} was calculated only for Pillars No. 1 to 3 (Figure 3-38) by repeatedly applying the proposed procedure. Figure 3-39 shows the reduced values of the recorded stresses and strains at the center locations of Pillars No. 1 to 3 while removing these pillars. The slope of the stress-strain relationship for each pillar location represents the K_{LMS} at this location.
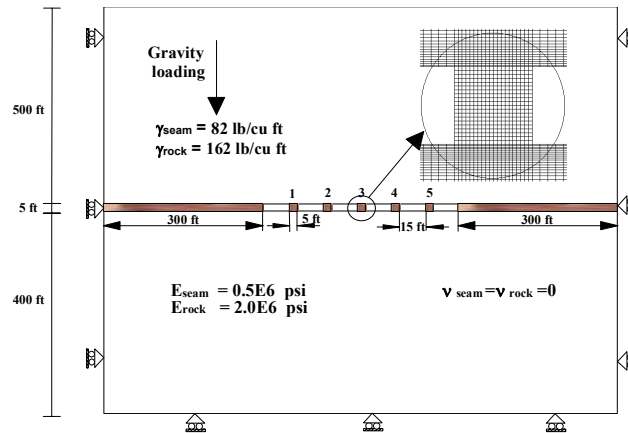
Figure 3-38 Configuration of finite element model used for estimating K$_{LMS}$
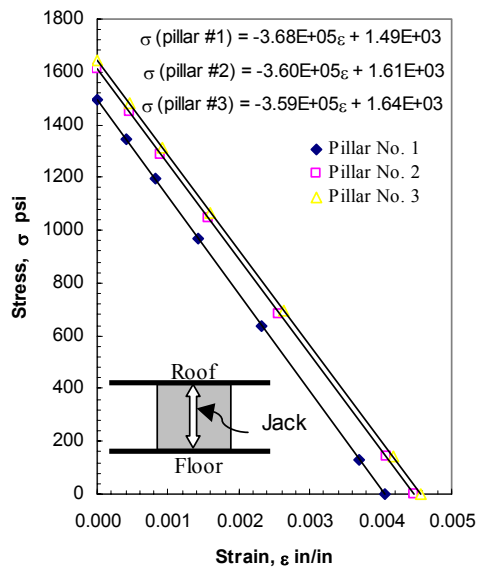
Figure 3-39 Stress-strain relations at the pillar center

Figure 3-40 shows the distribution of K$_{LMS}$ across the pillar width, it is obvious that the K$_{LMS}$ is not uniformly distributed across the pillar. This behavior is due to the non-uniform distribution of vertical stress and roof-to-floor convergence across the pillar width. Data analysis shows that in Pillar No. 3, in spite of the fact that a majority of the area in the pillar has a uniform stress concentration ($\approx$3), there are small zones of non-uniform stress concentration. Salamon [1970] estimated an error of 8 % in K$_{LMS}$

determined by his analytical approach due to the non-uniform stress distribution within the pillar.
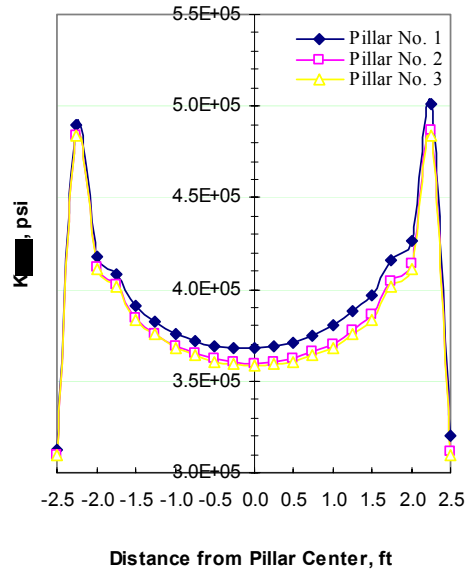
Figure 3-40 Distribution of K_{LMS} Pillars No. 1 to 3

Figure 3-41 shows the average values of K_{LMS} for Pillars No. 1 to 3 locations estimated by the proposed approach as compared with both the analytical and perturbation approaches. Generally, the estimated values of K_{LMS} using the proposed approach are smaller than those of the corresponding analytical methods, which mean that the proposed approach is more conservative. The difference percentages between the estimated K_{LMS} and the ones calculated by Salamon for Pillars No. 1, 2, and 3 locations are 12.29, 9.22 and 8.66 %, respectively. Because the difference percentages are very close to that error (8%) estimated by Salamon (especially at Pillar No. 3 location), it can be concluded that the proposed approach for estimating the K_{LMS} was able to consider the non-uniformity of stress distribution within the pillars and thus more accurate.

3.4 Summary

A typical model for coal pillars, based on the in-situ and laboratory tests was proposed. The proposed model considered the effects of the width-to-height ratio and

confining pressure on the deformation behaviors of coal pillar. This model can be used as a basic coal model in finite element applications. The linear Drucker-Prager model with mobilized angle of friction was found very successful to simulate the proposed model.

In this study, a gob model based on the Terzaghi's model was incorporated successfully into the comprehensive finite element package, ABAQUS, to simulate the loading behavior of longwall gob material. The proposed technique does not require the division of the gob area into zones of different materials as it was used to be done before. Instead, one gob material is prescribed for the whole gob area and the stiffness of gob material is updated automatically during the solution according to the state of stress.

The proposed gob material shows the ability to transfer the abutment loads away from the face and chain pillar system towards the center of the gob area. In spite the deviation of the model predictions from the in-situ measurements in some cases, it shows the same loading behavior. Further work needs to be done to study the effects of some parameters such as the gob height factor (gob height–to-seam height ratio), the overburden depth, the model dimensions, etc. on the performance of the gob model.
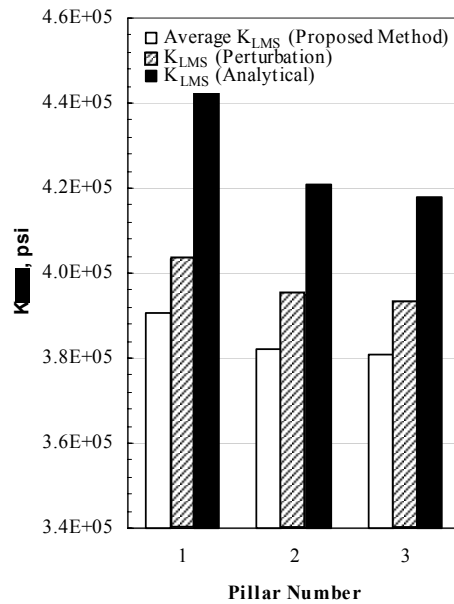
Figure 3-41 Average K_{LMS} for Pillars No. 1 to 3

CHAPTER 4

LONGWALL YIELD PILLAR DESIGN

Chapter 2 of this research presented a literature review for the current methods for yield pillar design; namely Carr and Wilson method, Chen method, and Tsang method. A critical review of these methods is important to develop a new yield pillar design methodology. The aim of this review is not to criticize any of these methods but to explore their main features. Consequently; the points of weakness of these methods can be avoided in the proposed yield pillar design methodology. Also, it would be more constructive to understand the stress distribution in the yield pillar and the yielding mechanism through these methods.

4.1 Discussion on Wilson's confined core concept

A combination of Finite Element models and parametric study were conducted in order to evaluate Wilson's assumptions and equations. Figure 4-1 shows the typical model configurations used in this evaluation. The model simulates the development loading condition of a 2-entry gateroad system of 18 ft wide entries. A row of rectangular pillars of 30 ft wide by 100 ft long was used in the gateroad system. Because of the symmetry, one-quarter of pillar of interest is modeled with an element size of 2.5 ft x 2.5 ft x 2.67 ft. To ensure the load transfer away from the pillar of interest, the model contains an additional pillar and a large part of solid coal of 107 ft wide. The material constitutive models, type of elements and the geological column used in these models are described in Table 4-1. As shown in Table 4-1, some parameters will be varied such as Young's modulus of rock and triaxial stress factors of coal and rock.
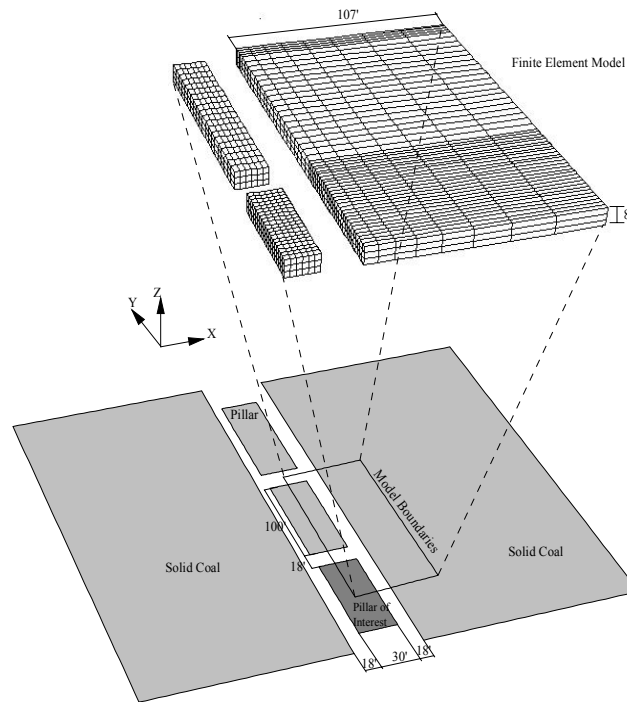
Figure 4-1 Finite Element Model Configurations

Table 4-1 Rock mechanics properties used in FE models

Strata Name	Thickness, ft	Density, lb/ft³	Young's Modulus, E x 10⁶ psi	Passion's ratio, ν	Triaxial stress factor, k	UCS, σc psi
S7	150	162	3	0.17	Elastic strata	
S6	22	167	2.175	0.12	Elastic strata	
S5	10	165	variable	0.13	variable	variable
Coal	8	82	0.35	0.3	variable	900
S3	6	165	variable	0.13	variable	variable
S2	30	167	2.32	0.18	Elastic strata	
S1	150	162	3	0.17	Elastic strata	

To fit Wilson's assumptions the linear Coulomb friction model, Figure 3-2, was used to simulate the interfacial contact between coal pillar and the roof and the floor. A constant friction coefficient, μ of 0.25 was used in these models [Iannacchione, 1990].

Wilson's Confined Core concept is discussed through the following comments:

1. Equation 2-6 implies that the rock/coal interface follows the linear Coulomb friction model (Figure 3-2) in which there is no maximum limit for the interfacial shear stress. Patrick [1982] illustrated that the variation in shear strength decreases as the normal stress increases. Chen [1989] explained that the right hand-side of Equation 2-6 is the maximum possible resistant force under the vertical stress σ_z. The equilibrium can be achieved under smaller frictional force. That implies that there could be an upper limit, τ_{max} for the frictional force to operate between coal pillar and the surrounding rocks. In other words, an alternative Coulomb friction model with shear limit (Figure 3-3) could be more suitable to simulate coal pillar/rock interface. In that model, regardless of the magnitude of the contact pressure stress, sliding will occur if the magnitude of the interfacial shear stress reaches this limit, τ_{max}.

2. Equations 2-12, 2-13, 2-15, and 2-16 imply that the vertical and horizontal stress distributions within the yield zone are independent of the overburden depth, Z. This behavior can be explained as follows: when the pillar ribs start to yield, the coal pillar/rock interface deteriorates at the yield zone. Hence the degree of confinement at the yield zone will be independent of overburden depth. This behavior can't be achieved by using the linear Coulomb friction model for the coal/rock interface. The linear coulomb friction model predicts a higher frictional resistance with higher overburden depths; consequently a higher vertical and horizontal stress will be detected even in the yield zones. To investigate this behavior, the results of two finite element models, Model no. 1 and 2 (Table 4-2), at different overburden depths are compared.

Table 4-2 FE Models Parameters for Wilson's model validation

Model No.	Parameters				
	Z, ft	E_r/E_c	σ_r/σ_c	k(coal)	k(roof/floor)
1	1500	10	4	2	3
2	2500	10	4	2	3
3	2500	10	4	3	3
4	2500	1	1	3	2

These models simulate a RRF condition with overburden depths of 1500 ft and 2500 ft, respectively. More detailed descriptions for the parameters used in these models are given in Table 4-1. The linear friction model, Figure 3-2, was used in these models to simulate the coal/rock interaction.

Stress analysis for the shaded area of study pillar, Figure 4-2D was conducted. Figures 4-2A and 4-2B show the pillar vertical and horizontal stress contours at overburden depths of 1500 ft and 2500 ft, respectively. It is obvious the pillar is composed of an elliptical elastic solid core surrounded by a yield zone. The vertical and horizontal stresses are uniformly distributed in the elastic solid core. The smallest values for the horizontal and vertical stress are observed in the yield zone. Figure 4-2C shows the vertical and horizontal stress distribution profiles along the transverse axis X-X at different overburden depths. The vertical stress distribution is similar to the LRS stress profile (Figure 2-11) except that the sudden change in the stress distribution at the yield/elastic boundary is not observed. It is obvious that higher vertical and horizontal stresses are associated with higher overburden depth. The greatest effect of overburden depth on the stress distribution within the pillar is observed in the elastic solid core. This is due to the high constraint provided by the linear friction model, especially at the elastic core. It is obvious that the coal/rock interaction model is the dominant factor on the stress distribution in the pillar.

A. Stress Contours at Z=1500 ft

B. Stress Contours at Z=2500 ft

- - - - - - - - - - - - - - - - - - **Yield Boundary**

D. Study Pillar

C. Stress Distribution at Section X-X
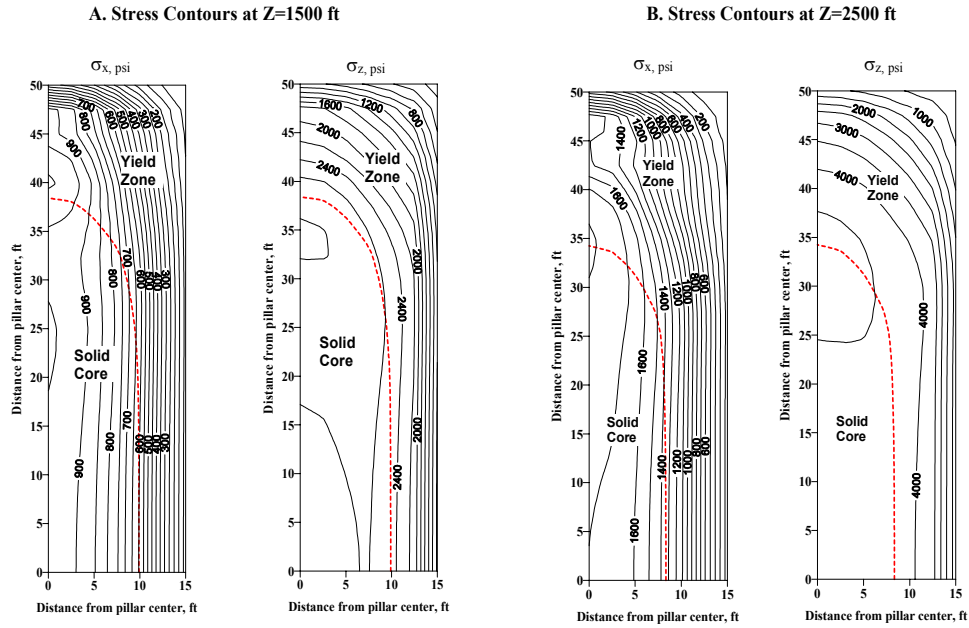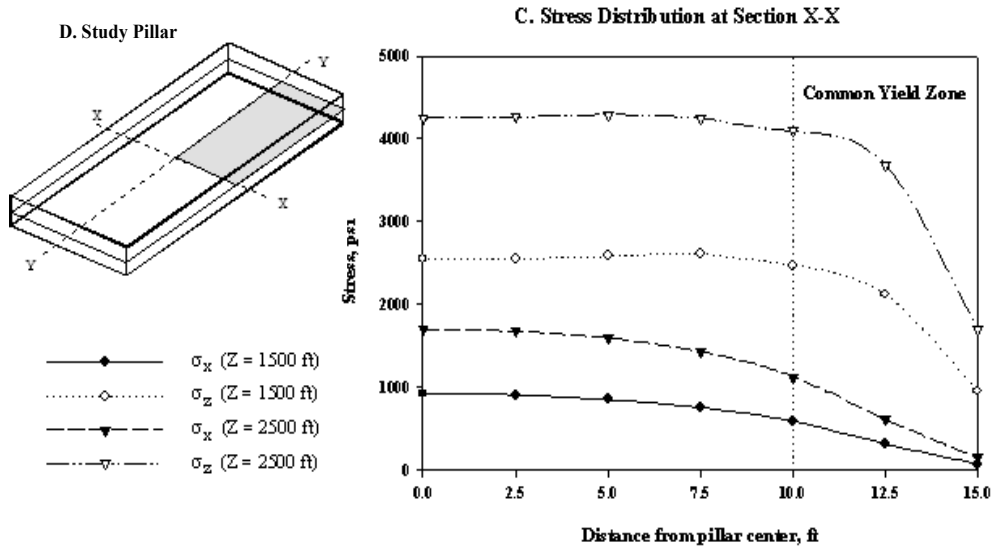
Figure 4-2 Stress distributions for linear Coulomb friction model

The Coulomb friction with shear limit was used instead of the linear model in Models 1 and 2 (Table 4-2). A value of 150 psi was assigned for the maximum possible shear stress, τ_{max} at the coal/rock interface. Figures 4-3A and 4-3B show the vertical and horizontal stress contours at overburden depths of 1500 ft and 2500 ft, respectively.

Due to low shear stress limit, the pillar is completely yielded at both depths. The horizontal stress contours at different overburden depths are identical. The vertical stress contours at the pillar ribs are almost the same for different overburden depths. Figure 4-3C shows the vertical and horizontal stress profiles along the transverse axis X-X for different overburden depths. Again the horizontal stresses along the transverse axis X-X are the same for overburden 1500 ft and 2500 ft. At the pillar core, there are still active constraint forces that make the vertical stress distributions affected by the overburden depth. Finally, it can be seen the independence of stress distribution within the yield zone can be achieved only by using a friction model that has a limit for the interfacial shear stress.

3. It is the friction and even cohesion of the interface between the seam and the rock beds that generates the constraints of the elastic solid core [Salamon, 1992]. Wilson predicted a significant difference for the stress distributions in the yield zones for those two boundary conditions; RRF and YRF. To investigate this adjustment, a stress analysis within the yield zones of two FE models, Models 3 and 4 representing the RRF and YRF, were conducted. The models geometry is shown in Figure 4-1 and its parameters are given in Table 4-2. To meet the YRF definition a significant amount of yielding has to develop in the immediate roof and floor. Hence a small triaxial stress factor was assigned to the roof and floor materials. Figure 4-4 shows part of the FE model for YRF condition, where a significant amount of yielding was observed in the immediate roof and floor. On the other hand, no yielding was observed for RRF condition.

A. Stress Contours at Z=1500 ft

B. Stress Contours at Z=2500 ft

C. Stress Distribution at Section X-X

D. Study Pillar
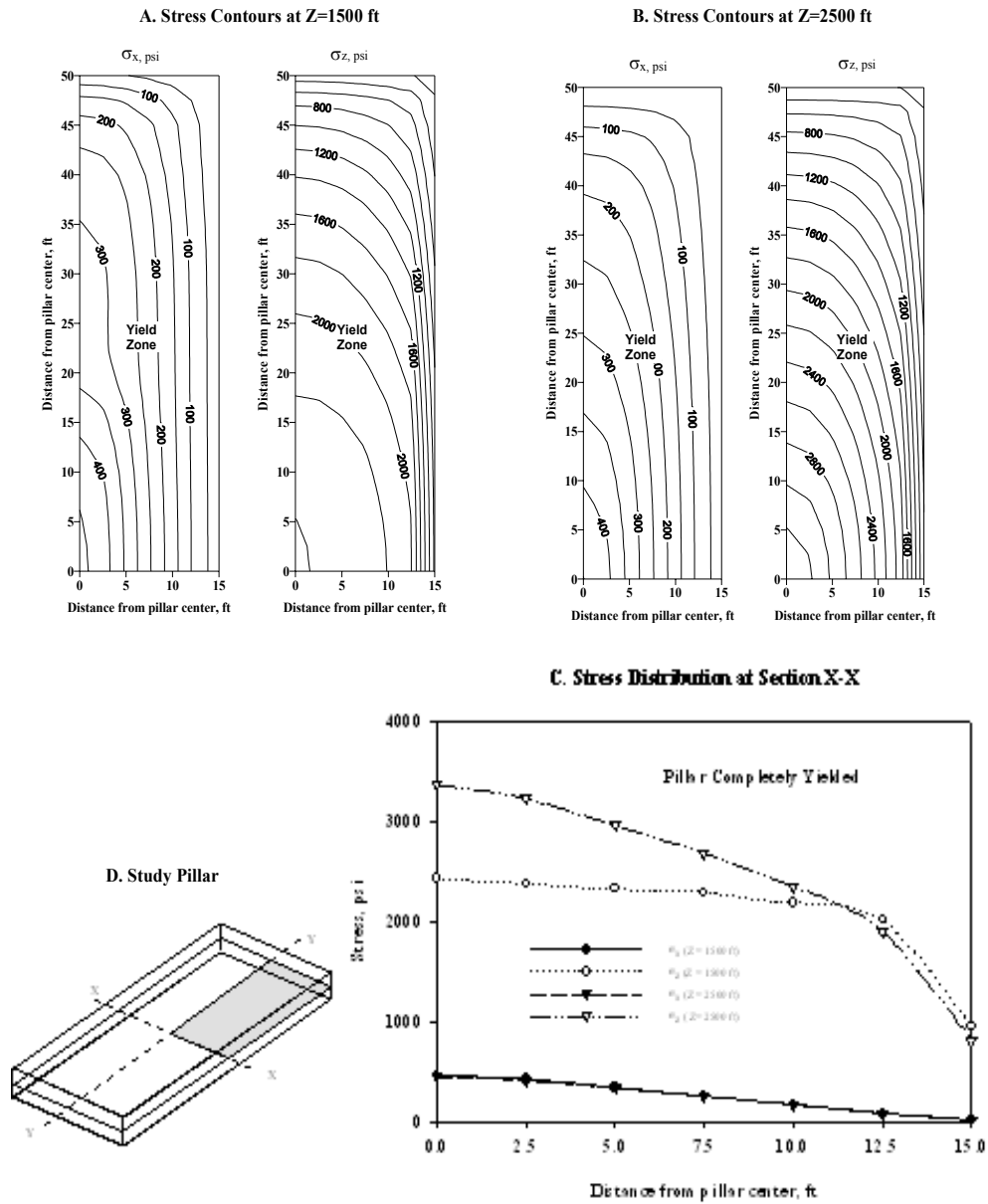
Figure 4-3 Stress distributions for Bi-linear Coulomb friction model

Figures 4-5A and 4-5B show the stress contours and yield boundary for YRF and RRF boundary conditions, respectively. These Figures illustrate that the area of yield zone was independent of the rock mechanics properties of the immediate roof and floor. Also, it shows that the stress levels and contours shapes for YRF and RRF were very close, especially for horizontal stresses distributions. Identifiable differences in the vertical stress contours, especially at the pillar corner and edge, were observed for YRF and RRF.

Figures 4-5C and 4-5D show the vertical and horizontal stress profiles for both YRF and RRF along the transverse axis X-X and longitudinal axis Y-Y, respectively. A small difference can be seen between stress distribution for YRF and RRF in the yield zone. Considering this small difference, it is found that the YRF condition builds up a higher stress level in the yield zone, especially at the pillar ribs, compared with the RRF condition. This conclusion contradicts with that of Wilson's.
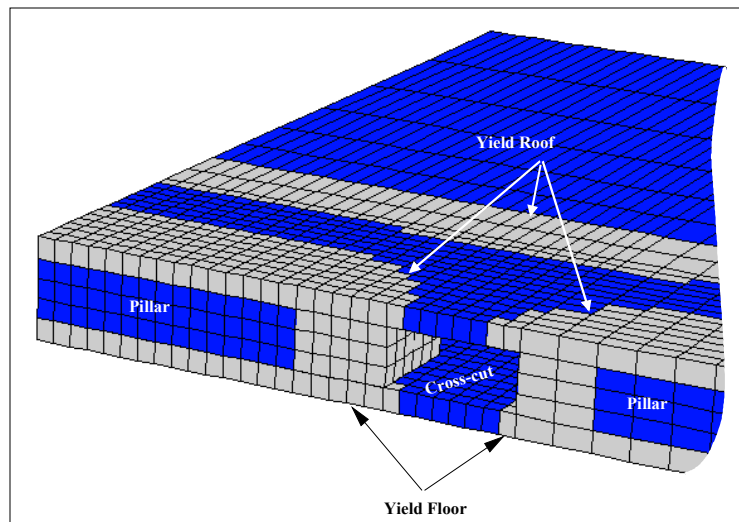
Figure 4-4 Locations of yield zones for YRF condition
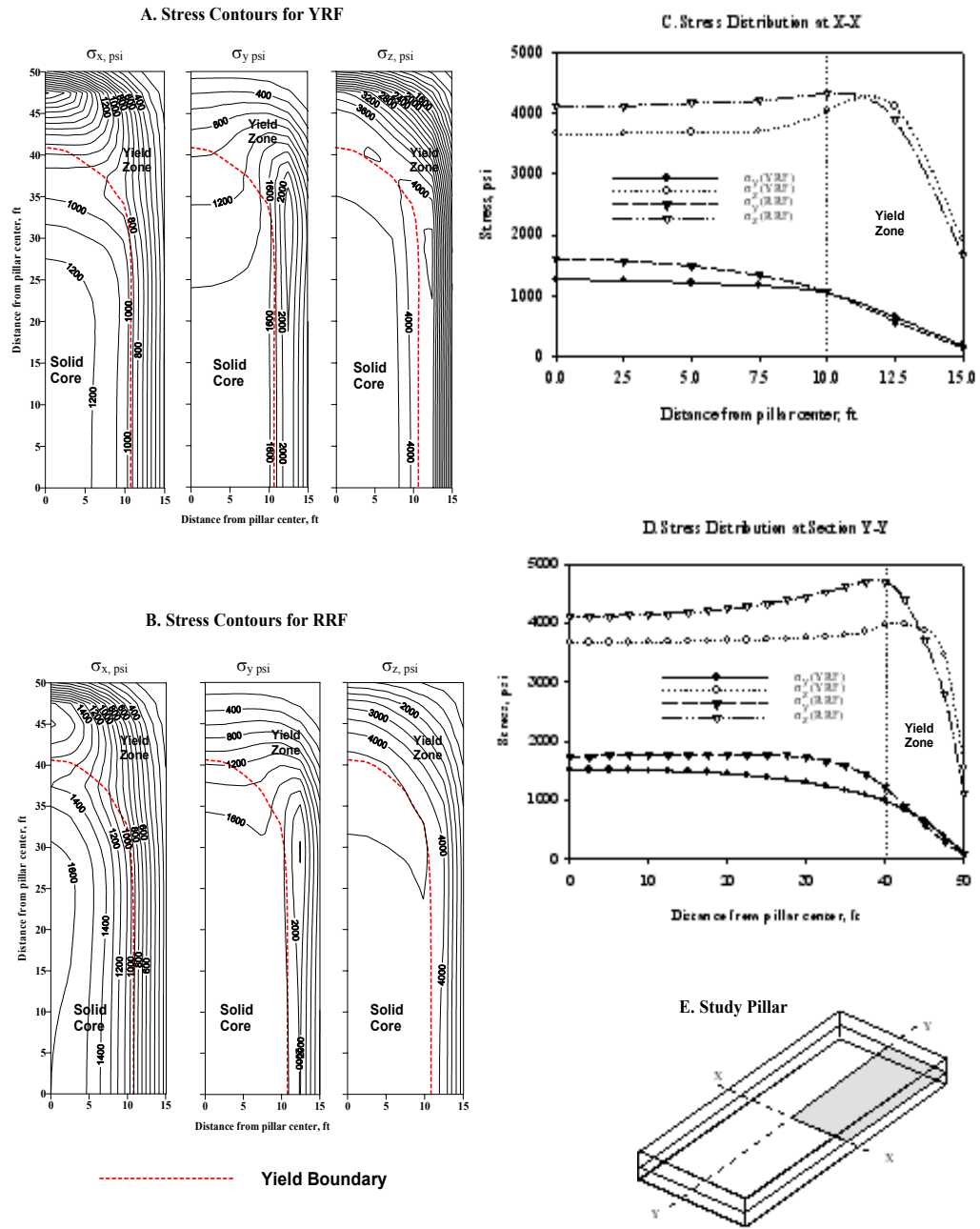
Figure 4-5 Stress distributions for YRF and RRF conditions

The modeling results can be explained by considering the dominant effect of linear friction model and amount of yielding in the immediate roof and floor. For YRF condition, the yielded parts in the roof and floor (Figure 4-4) will not be able to transfer the stresses to the solid core, especially at the pillar ribs. Therefore more stress will concentrate in the yield zone for YRF condition compared with RRF condition. The linear friction model that is assumed by Wilson to simulate the interfacial friction between the coal pillar and surrounding rock will produce high pillar confinement, irrespective of the rock mechanics properties of roof and/or floor. Hence it is not anticipated to see significant differences in the horizontal and vertical stress for YRF and RRF conditions.

From the above discussion, it is believed that the coal/rock frictional model is the key factor that determines the stress distribution in the pillar. To elaborate more about this factor, the Coulomb friction model with shear limit was used in two FE models. These models represent the RRF condition with different shear limits; 150 psi and 500 psi. These models use the parameters of Model 3, Table (4-2).

Figures 4-6A and 4-6B show the vertical and horizontal stress contours for shear limits of 150 psi and 500 psi, respectively. For a shear limit, τ_{max} of 500 psi, the pillar shows two distinct zones, i.e. solid core and yield zone. While the pillar is completely yielded for a low shear limit, τ_{max} of 150 psi. More pillar flows can be expected with lower confinement forces associated with lower shear limit.

It is obvious that a significant difference in magnitudes and shapes of stress contours for those cases. The vertical stress distribution at shear limit of 150 psi is more likely close to UL condition while for a shear limit of 500 psi, it is still close to LRS condition. Figures 4-6C and 4-6D show the vertical and horizontal stress profiles along the transverse and longitudinal axes of the pillar for different shear stress limits, 150 psi and 500 psi. Generally, the higher the shear stress limit, the higher the vertical and horizontal stress are developed in the yield zone. The difference is significant along the longitudinal axis and at the pillar corners.

A. Stress Contours (in psi) at $\tau = 150$ **psi**

B. Stress Contours (in psi) at $\tau = 500$ **psi**

C. Stress Distribution at X-X

D. Stress Distribution at Y-Y

E. Study Pillar

------------------ **Yield Boundary**
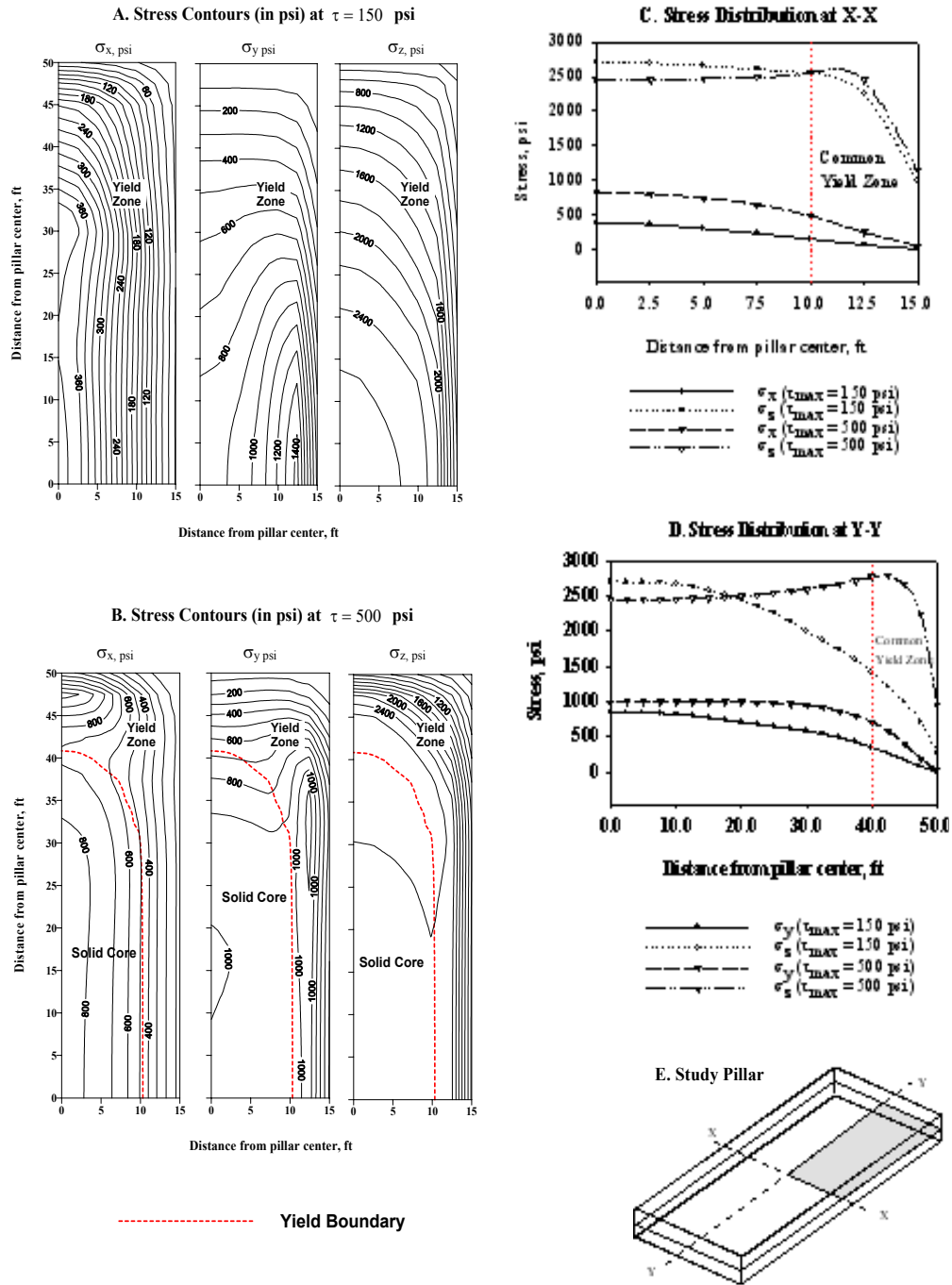
Figure 4-6   Stress distributions for YRF and RRF conditions for Coulomb friction model with shear limit

4. Mark [1988] shows that the estimated bearing capacity of pillar using Wilson formulae, Equations 4-15 to 4-18, was very sensitive to the assumed value of the triaxial stress factor k. Hence the most important material property is the triaxial stress factor k, which is directly related to the frictional angle, Equation 4-5. The value of k can be determined from laboratory triaxial tests. Generally, the measured in-situ friction angles are lower than the ones determined in the laboratory [Mark, 1990].

5. Salamon [1992] commented on Wilson's method, in regard to his assumptions as follows: -

   ♦ To define the extension of yielded zone, Wilson assumed that yielding ends when the horizontal stress in the crushed coal reaches its virgin value.

   ♦ At the interface between the yielded zone and the solid core, there is a discontinuity in the vertical stress, Figure 2-11.

   ♦ The buildup of core constraint is due to the interfacial friction between the coal seam and country rocks. Wilson makes no provision to take the interface conditions into account.

   ♦ Wilson's approach predicts excessively high stresses in the pillar core. The magnitude of these stresses may become sufficiently high to cause failure in the roof and/or in the floor.

4.2 Discussion on Chen's method

Chen's method for yield pillar design was summarized in Chapter 2. It was obvious that the Chen's method is totally based on the same principles of Wilson's method. Therefore, the comments and discussion for Wilson's method are still applicable on Chen's method. Moreover, further discussions on Chen's method can be achieved through the following comments:

1. Chen found that the stress distribution in the yield zone of coal pillars was significantly influenced by the Poisson's ratio, (Equations 2-23 and 2-24). Since this finding was one of the critical conclusions achieved by Chen's study, it was extremely important to investigate it. Therefore, four finite element models, (Table 4-3), were developed. The models configurations are shown in Figure 4-1. The virgin horizontal stress, σ_h is estimated by Equation (2-22) for Models 1 and 2, while it equals to the virgin vertical stress, σ_v for Models 3 and 4.

Table 4-3 FE Models Parameters for Chen's model validation

Model No.	Parameters					
	Z, ft	E_r/E_c	σ_r/σ_c	k	ν	σ_h/σ_v
1	2500	4	2	3	0.3	0.429
2	2500	4	2	3	0.4	0.667
3	2500	4	2	3	0.3	1
4	2500	4	2	3	0.4	1

Figures 4-7A and 4-7B illustrates the vertical and horizontal stress contours for Poisson's ratio of 0.3 and 0.4, respectively. Figures 4-7A and 4-7B illustrate that the pillar is composed of an elliptical elastic core surrounded by a yield zone. Insignificant difference in the stress contours of yield zones can be observed for different Poisson's ratios.

A. Stress Contours (in psi) at $\nu = 0.3$

B. Stress Contours (in psi) at $\nu = 0.4$

C. Stress Distribution at Section X-X

D. Stress Distribution at Section Y-Y

E. Study Pillar

----------------------- **Yield Boundary**
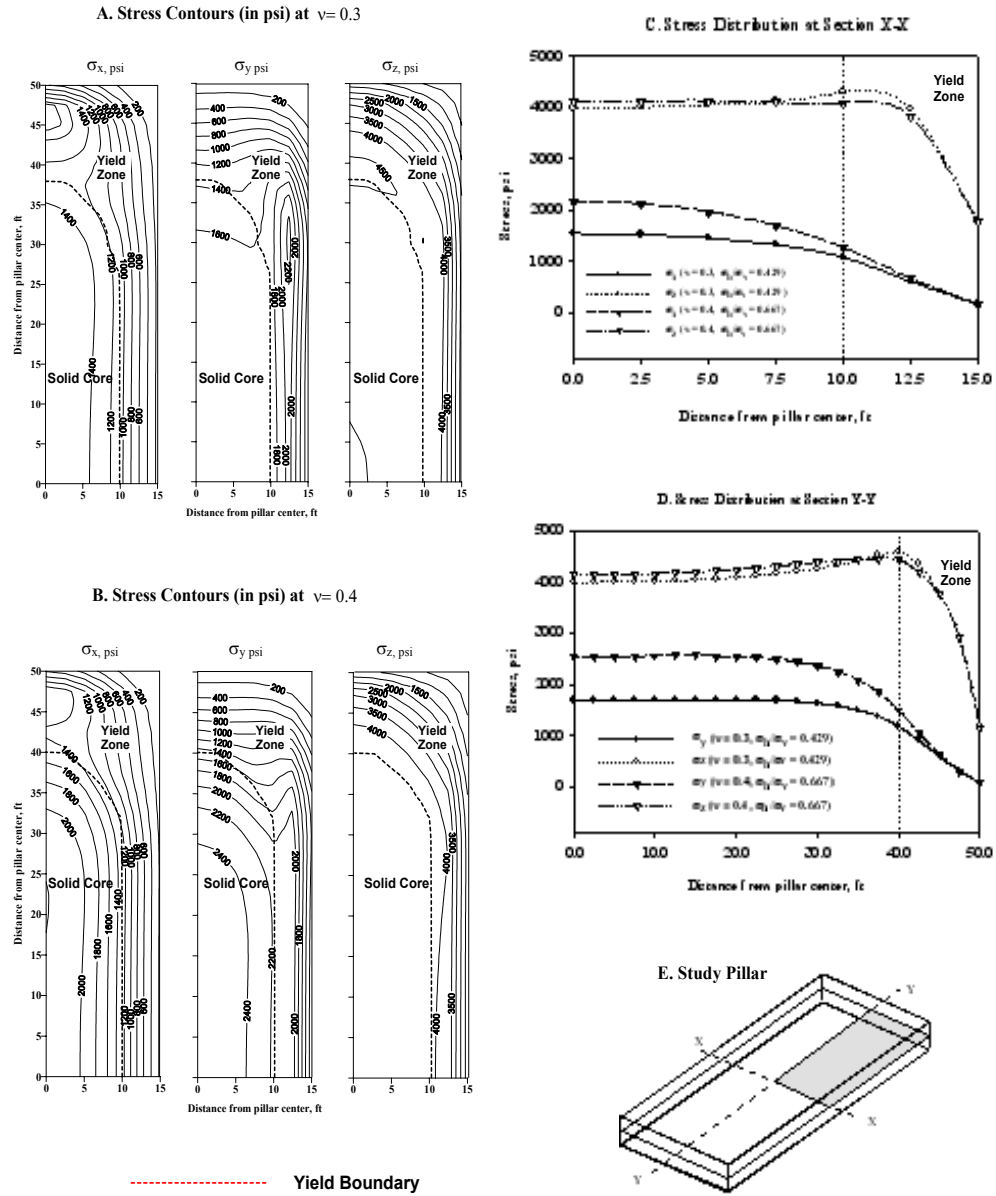
Figure 4-7 Stress distributions for different Poisson's ratios and virgin horizontal stresses

The difference between horizontal stress contours for different Poisson's ratios become significant only in the elastic core. Figures 4-7C and 4-7D show the vertical and horizontal stress distribution profiles along the transverse and longitudinal axes, respectively. It is obvious that the vertical stress distribution is independent of the Poisson's ratios. While the horizontal stress distribution is affected by Poisson's ratio only in the elastic core. The horizontal stress in the elastic core is directly proportional to the Poisson's ratio.

In fact the increase in horizontal stress is due to the high virgin horizontal stress associated with a high Poisson's ratio, Equation 2-22. This behavior can be more obvious in the elastic core than in the yield zones, since the elastic core can preserve high percentage of the virgin horizontal stress.

Model 3 and 4 were conducted to show that the horizontal stress distributions are mainly affected by the virgin horizontal stress level not by Poisson's ratio. The virgin horizontal-to-vertical stress ratio was defined as 1 while the Poisson's ratio was changed from 0.3 to 0.4. Figures 4-7A and 4-7B illustrates the vertical and horizontal stress contours for Poisson's ratios of 0.3 and 0.4, respectively. It is obvious that there are very minute differences in vertical and horizontal contour values for different Poisson's ratios. Figures 4-7C and 4-7D illustrate the vertical and horizontal stresses distributions profiles along the transverse and longitudinal axes. These figures show very small differences for the vertical and horizontal stresses for different Poisson's ratios. It is believed that these small differences could be contributed by the change of Poisson's ratio. Comparing Figures 4-7C and 4-7D with Figures 4-7C and 4-7D, respectively, it could be concluded that the stress distribution in the yield zone is independent of the Poisson's ratio of coal material.

2. It was not clear why Chen did not try to statistically develop a relationship between vertical stress and Poisson's ratio as he already did for horizontal stress distribution. Instead he assumed that the linear relationship between coal strength and the confining pressure is still valid in the yield zone. Consequently he was

able to relate the vertical stress to the horizontal stress at any given point in the yield zone (Equation 2-9). This could be explained by the above analysis which shows the indecency of the vertical stress distribution with respect to Poisson's ratio.

3. Following Wilson's approach, Chen estimated the width of yielding zone by equating the horizontal stress with the virgin vertical stress; assuming that the virgin horizontal and vertical stresses are equal. This assumption conflicts with Equation 2-22, where the virgin horizontal stress is estimated as a fraction of the virgin vertical stress. Therefore, Equation 2-25 should be reevaluated by equating Equation 2-23 to Equation 2-23 and solving for x. The new estimated yield width should be less than the one predicted by Equation 4-23.

4. Chen's method doesn't consider the roof/floor constraint effects for coal pillar. To compensate for this effect, Chen concluded that with a small Poisson's ratios, the estimated yield widths by Chen's method coincide with the ones predicted by Wilson's method for YRF condition. While as the Poisson's ratios increases, the estimated yield widths by Chen's method coincides with the ones predicted by Wilson's method for RRF condition (Figure 4-8). Chen didn't provide any explanation for this conclusion.

5. Finally, Chen used 2D finite element models in his study. This approach can't provide a rational simulation for the front abutment pressures that transferred to both the face and the yield pillars.
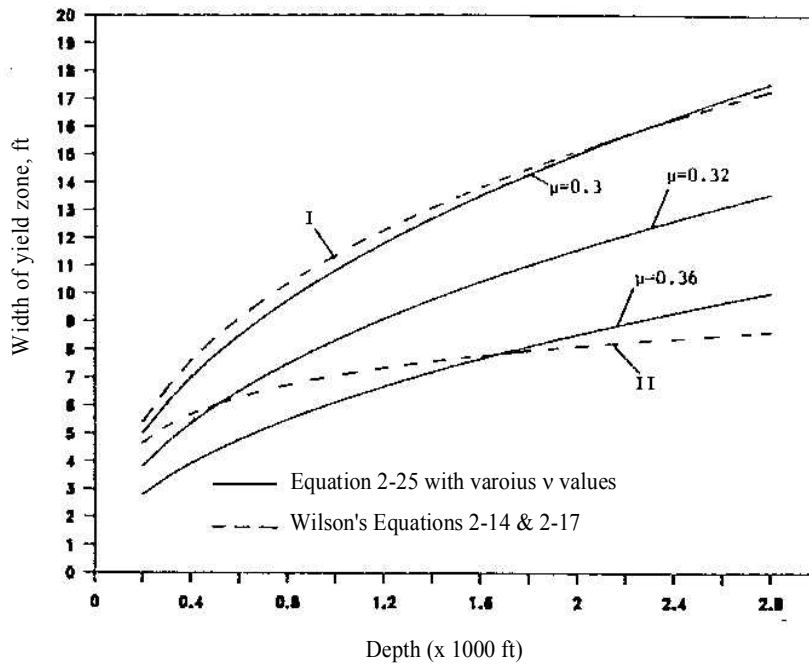
Figure 4-8 Yield zone widths predicted by Chen and Wilson methods

4.3 Discussion on Tsang's method

Tsang's method for yield pillar design was summarized in Chapter 2. It was obvious that this method is of finite element modeling and multi-linear regression. The following comments could be driven:

1. Conceptually like any statistical approach, the orthogonal design of experiment (DOE) technique assumes the possibility of error in the experiment outcomes if it is repeated. The error concept is not applicable to the FE model results, since the same model results will be achieved every time the same FE model is solved.

2. Using the Taguchi DOE approach, Tsang used only 27 models to study the effects of 10 variables in 3 levels. Ignoring the misuse of the DOE technique, this number of models is very small to get a rational regression model for 10 variables. Since;

with this small number of models, it will not be possible to consider all the main effects and the interactions of the studied variables.

3. Unlike Wilson's method and Chen's method, Tsang totally ignores the effect of triaxial stress factor of coal in his regression equations. Instead he introduced the cohesive strength of the coal.

4. Like Chen's method, Tsang used 2D finite element models in his study.

4.4 Summary

Until now, there is no yield pillar design methodology that involves the stability evaluations of the yield pillar in the post-peak region. Therefore, unless the consideration of the post-peak behavior of the yield pillars is included in the pillar design process, the risks of unexpected accidents, such as pillars violently bursting into the entries, still pose a threat to the safety of the personal and equipment close to the entries.

The ultimate strength concept for pillar design is not enough to size a stable yield pillar. Other criteria should be used too, such as; Local Mine Stiffness, Bump Index, explained in Chapter 5.

An appropriate friction model to simulate the roof/floor coal pillar interface is crucial for any yield pillar design model.

To fully consider the interactions between any studied variables, a full factorial analysis, in which the whole combinations of the variables are considered, could be the best choice.

Finally, the interpolation technique rather than regression technique could be more suitable for the development of a yield pillar design model. This is because of the limited number of levels of the studied variable.

CHAPTER 5

EVALUATION OF YIELD PILLAR STABILITY

In this chapter a new method for evaluating the stability of yield pillars will be introduced. The proposed method considers the non-uniform stress distribution of yield pillars by dividing the yield pillar into three loading zones; namely core, transition and rib zones. The proposed yield pillar stability evaluation method is conducted in two steps:

- Estimation of pillar loading – numerical modeling is a good tool to estimate the pillar loading for most of the geological and geometrical conditions. In this study, finite element technique was used to estimate the state of stress, strain, elastic strain energy and plastic energy, etc. at every point within the pillar. This estimation was conducted for different mining stages; development, 1st panel mining and 2nd panel mining.

- Estimation of stability indicators – the pillar stability is checked by number of stability measures, such as; Core Stability Factor, CSF, Pillar Bump Index, PBI and Rib Instability Index, RIF. A detailed discussion for these proposed measures will be presented in this chapter.

5.1 Coal pillar model

5.1.1 Coal pillar stress distribution

Without a good understanding of the stress distribution in a yield pillar, an adequate design of a yield pillar is almost impossible. Wagner [1974] conducted the first comprehensive in-situ tests of coal in a South African coalfield. The tested pillars ranged from 1.968 ft to 6.56 ft wide with width-to-height ratio from 0.6 to 2.2. These tests were very successful in determining the post-peak behavior of coal pillars and providing a detailed insight into the mechanism of pillar failure. Wagner measured the stress

distribution across pillars at various stages of deformation. Figure 5-1 shows the typical stress profiles for pillars with width-to-height ratios of 2 at various stages of pillar compression. Figure 5-1 shows that the stress distribution inside the pillar is not uniform. Wagner illustrated that the pillar failure initiated at the circumference of the pillar and then transferred inwards. It was found that the perimeter of the pillar was capable of carrying relatively little stress but this portion of the pillar provided lateral confinement which enhanced the strength of the pillar core. It was realized that the central portion of the pillar was capable to withstand extremely high stresses even when the pillar has been compressed beyond its maximum resistance, which is traditionally regarded as the strength of the pillar.
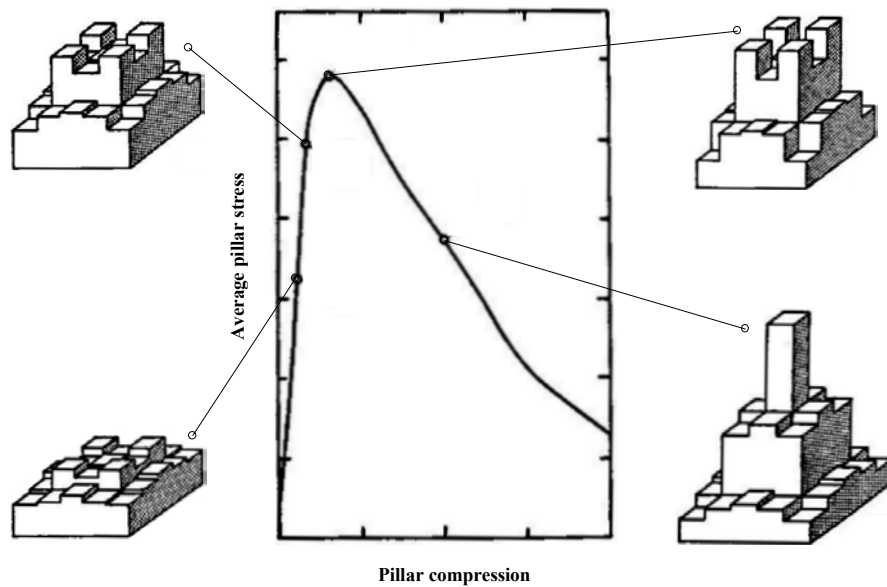
Figure 5-1 Stress profiles at various stages of pillar compression [after, Wagner 1974]

5.1.2   Heasley's model

Heasley [1992] developed a typical model for coal pillar (Figure 5-2). This model assumed that the coal pillar is composed of four zones of different load-deformation

curves. Heasley's model was derived from stress measurement for Olga Mine. Figure 5-2 illustrates that the "external" coal zone is located on the edge of the pillar and the peak and residual strength increases progressively toward the "core" zone in the center of the pillar. The "external" zone behaves more like a brittle material under uniaxial compression. The "external" zone usually formed after the pillar was formed. The "core" zone behaves more like a ductile material because of the triaxial compressive stress condition. The "interior" and "central" zones have the strength in between the two extremes; i.e. external and core (Figure 5-2).
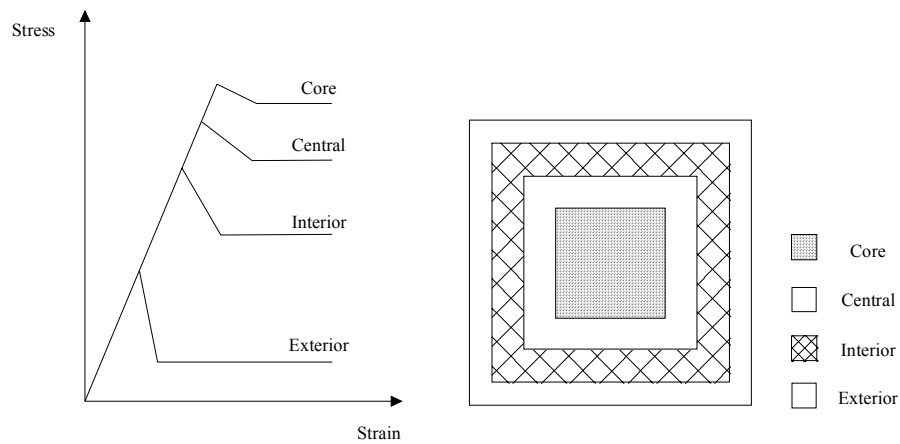
Figure 5-2 Heasley's coal pillar model [after, Heasley 1992]

Heasley estimated the average ultimate strength of each zone by Mark-Bieniawski strength formula, Equation 5-1 [Heasley, 1998].

$$S_p = S_i \left[0.64 + 0.36 \frac{W}{H} \right]$$

Equation 5-1

where S_p is the average pillar strength; S_i is the in-situ coal strength; W is the pillar width; and H is the pillar height.

Heasley estimated the ultimate stress of exterior zone as equal to the average strength of $2E_w$ x $2E_w$ pillar size, where E_w is the element width. Similarly for central,

interior and core, he assumed corresponding pillars of 4E_w x 4E_w, 6E_w x 6E_w and 8E_w x 8E_w, respectively.

5.1.3 New pillar model

Using the adapted Drucker-Prager model and the rock/coal frictional model presented in Chapter 3 of this research, the non-uniform stress distribution in the yield pillar can be simulated. According to the proposed coal model, once the yield pillar is formed, three zones of different amount of confinement could be defined, Figure 5-3; namely core, transition and rib zones. These zones could be defined based on the amount of confinement developed in the yield pillar. More detailed explanation for those zones is presented below:

Rib zone – The rib zone occupies the pillar corners, Figure 5-3. It is the weakest part of the pillar because it is bounded by free faces on two sides; i.e., low confining pressures. The pillar yielding starts from this zone towards the pillar core. In this study, the rib zone is defined as the instable parts of the pillar which have post-peak stiffness larger than or equal to the local mining stiffness, Equation 5-2:

$$\left| K_p \right| \geq \left| K_{LMS} \right| \qquad\qquad \textbf{Equation 5-2}$$

where $|K_{LMS}|$ is the absolute value of the local mine stiffness; and $|K_p|$ is the absolute value of pillar post-peak stiffness.

Therefore, the rib zone behaves as a brittle material under uniaxial compression. Numerically, the rib zone is capable of carrying relatively little stress but it can't store large amount of elastic strain energy. Most of the loading energy of the rib zone is dissipated in the form of plastic deformation. The instability of the rib zone can be manifested in the form of coal bounces. Figure 5-4 shows a corner of yield pillar, where at least a 5ft width of broken coal could be considered as a rib zoon.
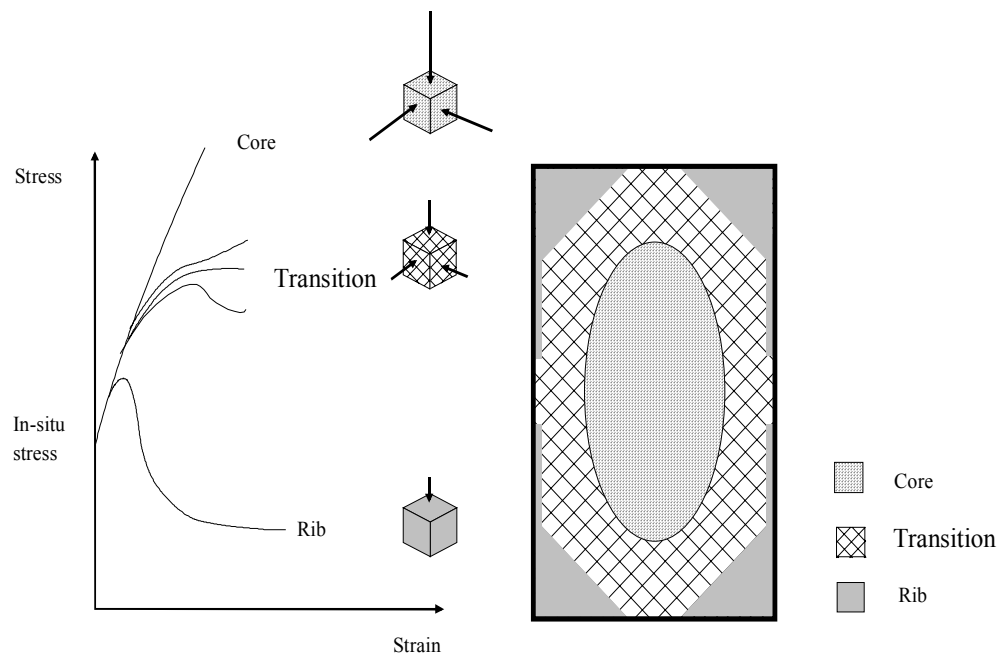
Figure 5-3 Plane view for a yield pillar with different deformation properties

Figure 5-4 A photo for a failed pillar corner

Core zone - The core zone occupies the center portion of the pillar. In this study, the core zone is defined as the part of the pillar that does not experience any plastic deformations. The elastic behavior of the core zone is a result of high horizontal stresses

in this zone. The core represents the strongest part of the pillar which allows the induced stresses to transfer to it. Therefore, the core stores a significant amount of elastic strain energy. Because the yield pillars have relatively small widths and operate under high overburden depths in the U.S., the state of stress in the core zone is usually very close to the yielding condition. Hence the stability of the core zone is crucial when the longwall approaches the yield pillar. At this stage of mining, the core zone starts to yield. The more the elastic strain energy retained in the yielded parts, the more likely the pillar experiences pillar instability such as coal bumps

Transition zone – The transition zone is located between the rib and core zones. The transition zone is characterized by a relatively high horizontal stresses. The transition zone is the most complicated part of the pillar where three types of stress-strain behaviors could be observed for the points located in this zone; namely strain hardening, elastic-plastic and strain-softening with high residual strength. Generally, the transition zone behaves more like a strain-hardening material because of the high triaxial compressive stress condition. Part of the energy of transition zone is dissipated in the form of plastic deformation while a significant amount of elastic strain energy is stored in this zone.

The size of any of the pillar zones depends on many factors, such as; the end constraint provided by the roof and floor, pillar width, overburden depth, stage of mining, etc. During different stages of mining, the pillar zones change their sizes and locations. It is not necessary to have all the three pillar zones, for example under a condition of relatively low pillar end constraints, the elastic zone could be disappeared.

5.2 Yield pillar stability criteria

As illustrated before, the yield pillar is composed of different zones with different load-deformation behaviors. Therefore, more than one stability criterion should be used to evaluate the stability of yield pillar. Throughout the following discussion, the yield pillar is composed of a number of elements. The stability/instability of the pillar zone will be evaluated in two steps: first; the stability factors of the elements inside the pillar zone

are determined, second; the stability of the pillar zone is determined as an average for the stability/instability factors of the elements located inside the studied zone.

5.2.1 Strength criterion

The strength criterion is applied to evaluate the stability of the core zone. The strength criterion evaluates the state of stress in the core with respect to the yield strength. The element stability factor (ESF) is determined by the linear Druker-Prager yield criterion (Equation 3-1) as follows:-

$$ ESF = \frac{k + J_1 \tan \alpha}{J_{2D}} \qquad \text{Equation 5-3} $$

where, α and k are the material property constants related to cohesion and angle of internal friction; J_1 is the first invariant of stress tensor; and J_{2D} is the second invariant of the deviator stress tensor.

Numerically, it is not possible to have ESF less than 1. The possible values for ESF are either 1 for those elements experiencing plastic deformation or greater than 1 for elastic elements. The core stability factor CSF is determined by averaging the element stability factors (ESF) of all elements located within the core zone.

As mentioned earlier, the core zone has the ability to store a significant amount of elastic strain energy. As long as the core stability factor CSF is greater than 1, the elastic strain energy stored in this zone will be in stable condition. This condition can be strongly obvious in the stiff pillar design, where the core zone characterizes most of the pillar and the stress level inside the stiff pillar is far from its yielding strength. On other hand the stability of the core is crucial for the yield pillar, especially when the longwall approaches the yield pillar. At that stage of mining, the yielded elements inside the core zone join the transition zone and the stored elastic strain energy could be released to the surrounding. Therefore another stability criterion is required to check the stability of those yielded elements, i.e. an energy criterion.

5.2.2   Bump Index, BI

The strain energy storage index, described in Chapter 3 of this work, is used as an indicator for the stability of the transition zone. Figure 5-4 shows a typical stress-strain curve for an element located in the transition zone. At any stress level, σ_c, the shaded triangle CED represents the amount of stored strain energy, W_e while the area of polygon OABCE represents the dissipated energy, W_p. In this study, FE technique was used to estimate the state of elastic strain energy and plastic dissipated energy at every element within the pillar. Hence; using Equation 2-5, the element bump index could be calculated as follows:

$$EBI = \frac{W_e}{W_p}$$
Equation 5-4

The bump index BI for the transition zone is determined by averaging the local strain energy storage indices.
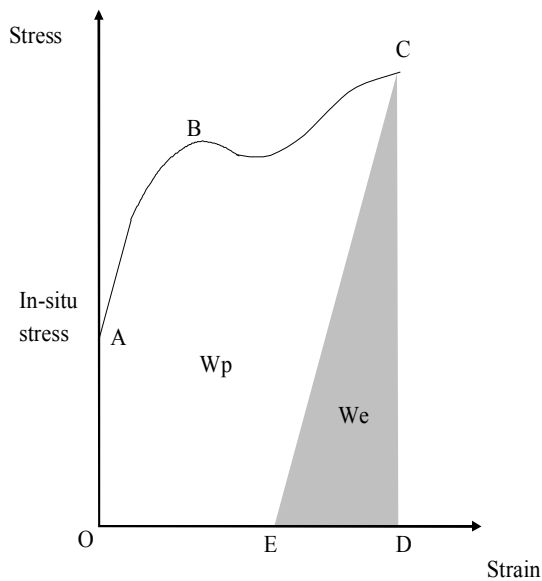
Figure 5-5 Strain energy storage index, BI for transition zone

5.2.3 Rib Instability Factor, RIF

The local mine stiffness criterion, described in Chapter 3, is used to evaluate the instability of the rib zone. The element instability factor EIF for the rib zone elements, is determined by:

$$EIF = \frac{\left|K_p\right|}{\left|K_{LMS}\right|}$$
Equation 5-5

According to the definition of rib zone (Equation 5-2); the EIF is usually greater than 1. The instability factor of the rib zone, RIF is determined by averaging the element instability factors (EIF) of all the elements located in the rib zone. The RIF covers a wide range of instabilities; from unrecognizable bounces to serious ones. The larger the rib instability factors, the larger the energy that can be released to the surrounding.

5.3 Case Study and Model Validation

The U.S. Bureau of Mines (USBM) has long been involved in coal mine bump research as part of its mission to improve mine safety. As a part of this research, a site monitoring program was carried out in Sunnyside No.1 Mine, UT [Koehler, 1994]. The monitoring stations were located in a two-entry gateroad where pillars were uniformly decreased in width from 56 ft to 32 ft along the length of the entry system from the setup room. Two sites were instrumented by USBM hydraulic borehole pressure cells (BPCs). The vertical pressure in the pillars and the degree of pillar yielding were monitored throughout the adjacent panel mining. Coal bumps had occurred at one of the monitoring sites.

In this chapter the USBM monitoring program and its results will be summarized after Koehler [1994, 1996]. The monitoring results will be used to calibrate the three-dimensional FE models for monitoring sites. A detailed study for these models will be conducted to define the conditions associated with coal bumps. Based on this analysis, a

more comprehensive analysis for the proposed yield pillar stability evaluation method will be conducted.

5.3.1   Description of case study

The Sunnyside No. 1 Mine is located in eastern Carbon County, UT, approximately 26 mi east of the town of price. The longwall mining system was first introduced at Sunnyside in 1961 to improve worker safety in the difficult, bump-prone conditions found on the property. Natural factors conducive to coal bumps at the mines include: great depth (as much as 2,950 ft) and massive sandstone strata above and below the coal seam. A two-entry yield pillar system was chosen to cope with these bump-prone conditions. After a process of trial and error, a 33 ft wide yield pillar was found virtually reduces pillar bumps and greatly reduces face bumps [Koehler, 1994].

The field study was located in the two-entry 23rd Left gateroad of the Sunnyside No. 1 mine (Figure 5-6). The longwall panel was 600-ft wide. As a result of surveying error, the chain pillars of the 23rd Left gateroad are uniformly decreased in width from 56.1 ft at the startup room to 32.1 ft at the planned face recovery stop line. The chain pillars size at monitoring Sites 1 and 2 were 55 and 40 ft wide, respectively (Figure 5-6). The horizontal distance between Sites 1 and 2 is approximately 2310ft. The chain pillar size at Site 3 was 35 ft. Site 3 was not monitored because mining operations were prematurely halted for business reasons. The mining height was 7 ft. Only sites 1 and 2 will be described here and will be used for modeling back calculations.

Site 1

Site 1 was located between crosscuts 46 and 49. The size of pillars at Site 1 was 55-ft x 105-ft and the overburden depth was approximately 2600 ft. Four BPC's were installed at 9.8 ft, 18 ft, 36.1 ft and 46 ft measured from belt entry side in one of the chain pillar. Ten probeholes were drilled in two adjacent pillars at site 1 (Figure 5-7).

24th Left Panel

2000 ft 2500 ft 2500 ft 2000 ft 1500 ft 2000 ft 2500 ft 2500 ft

Site 1 (55 ft)

Site 2 (40 ft)

Site 3 (35 ft)

23rd Left Panel

Projected recovery room

Actual face stopline

(Pillar taper not shown. Drawing not to scale)

Dip
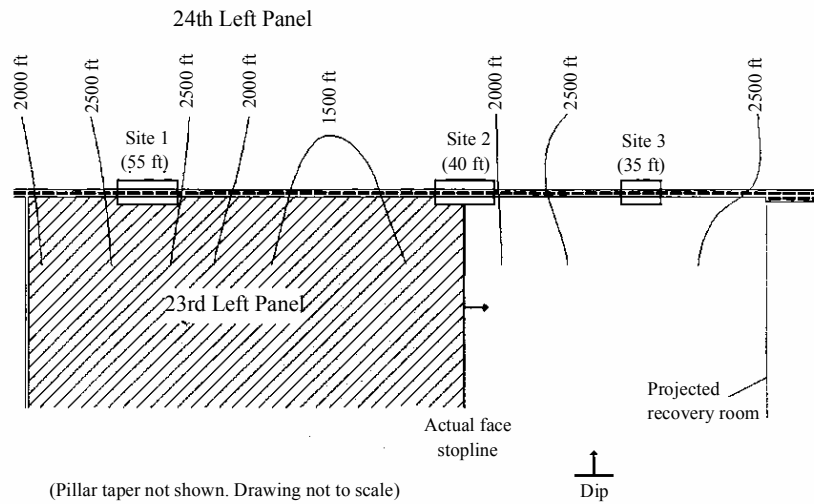
Figure 5-6 Study site locations, Sunnyside No. 1 Mine [Kohehler, 1996]

Site 1
Overburden depth = 2600 ft

Dip

24th Left Panel

Cross-cut 49   Cross-cut 48   Cross-cut 47   Cross-cut 46

55ft

105ft

Scale, ft

23rd Left Panel

■ Borehole pressure cell

— Probehole

0   65.6
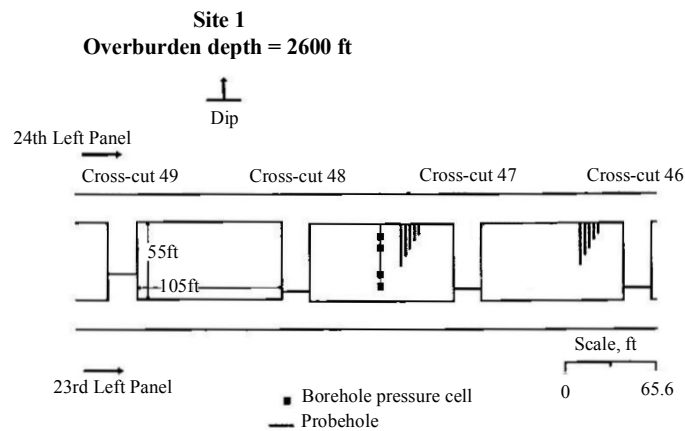
Figure 5-7 Site 1 instrumentation/probehole drilling location map [Koehler, 1994]

Figure 5-8 shows the BPC gage pressure profiles across the instrumented pillar for three face positions (FP); 256 ft, 26 ft and 0 ft inby site 1. The 256 –ft inby FP profile shows that the pillar was uniformly stressed. Very slight differences were observed

between the measured BPC pressures and the virgin stress (2886 psi). The measured pressures were considerably low compared with the face position. Field observations indicated an increase in the frequency and magnitude of rock noise at that face position, but no significant coal bump events had been reported. The pillar was yielded to a depth of 4.9 ft at each side.

As the mining progressed to the 26-ft inby FP (Figure 5-8), the BPC gage pressures increased noticeably because of the approach of front abutment pressure. The pillar was yielded to a depth of 10 ft near the belt entry side. No noticeable changes in the yield zone at the travel way side of the pillar. The stress distribution in the pillar was not uniform anymore, where more load was transferred to the pillar core. The highest pressure of 9200 psi was recorded near the travelway side, while a smaller value of 8400 psi was recorded near the belt entry side. Coal bumps was reported at a distance of 66 to 100 ft behind the face.
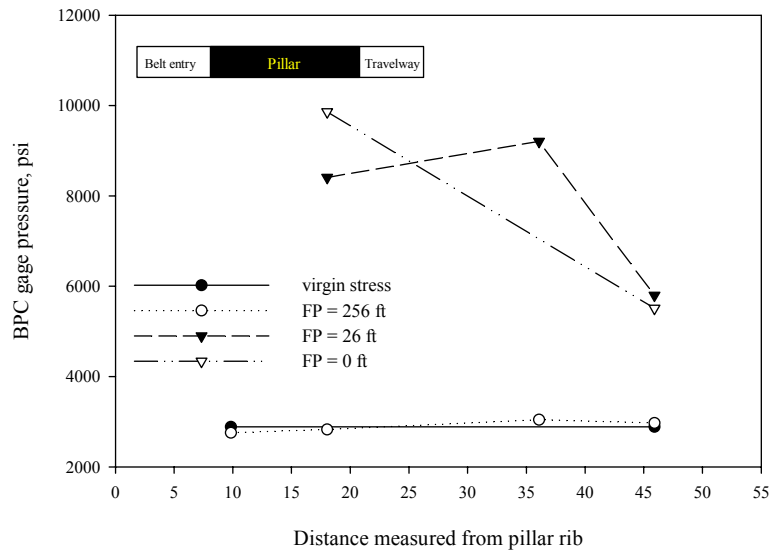
Figure 5-8 Ground pressure profiles for Site 1 [Koehler, 1994]

When the face reached the study site (0 FP), more load was transferred to the pillar (Figure 5-8). The BPC gage pressure increased at the belt entry side of the pillar, while a slight increase in BPC gage pressure was recorded at the travel way side. No more pillar yielding was recorded at that face position. This could be explained that the pillar still have a large elastic zone which makes it able to gain more load without further yielding. Unfortunately, the BPC at 36.1ft deep was lost. The pressure chart of this destroyed cell indicated a sudden increase of pressure by 5800 psi. This sudden pressure increase was explained as a result of heavy bump activity started at the chain pillars immediately inby the study site. Shortly after the face was passed by the study site, the data collection was stopped because of the previously mentioned bump. Another pillar bump was reported when the face was approximately 197 ft outby the study site.

Site 2

Site 2 was located between crosscut 24 and 27. The size of pillars at Site 2 was 40-ft x 105-ft and the overburden depth was approximately 1900 ft. Three BPC's were installed at 10 ft, 20 ft and 30 ft measured from belt entry side in one of the chain pillar. Ten probeholes were drilled in two adjacent pillars at Site 2 (Figure 5-9).
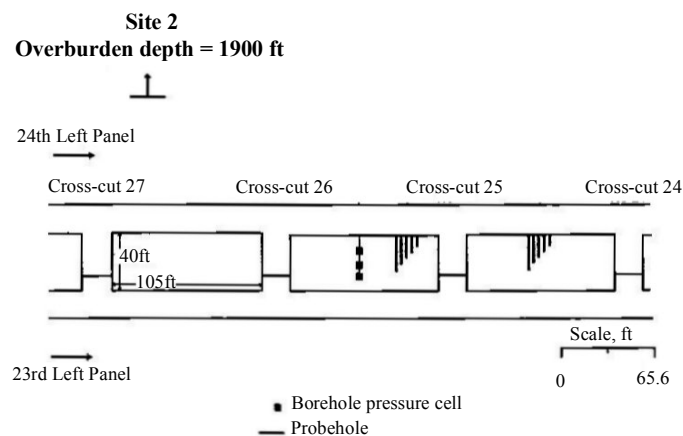
Figure 5-9 Site 2 instrumentation/probehole drilling location map [Koehler, 1994]

Figure 5-10 shows the BPC gage pressure profiles across the instrumented pillar for three face positions (FP); 523 ft, 213 ft and 79 ft inby Site 2. As the mining progressed to the 523-ft inby FP, it was not expected to have a significant load transfer to study site. At that face position, the pillar was mainly stressed by the development loads. The probeholes predict that the pillar was yielded to a depth of 9.8 ft which means that almost halve of the pillar width was yielded at that stage. The 523–ft inby FP profile (Figure 5-10) shows that the pillar load was approximately equal to the virgin vertical stress (2109 psi). The measured pressures are considerably low which could be explained by significant amount of pillar yielding.
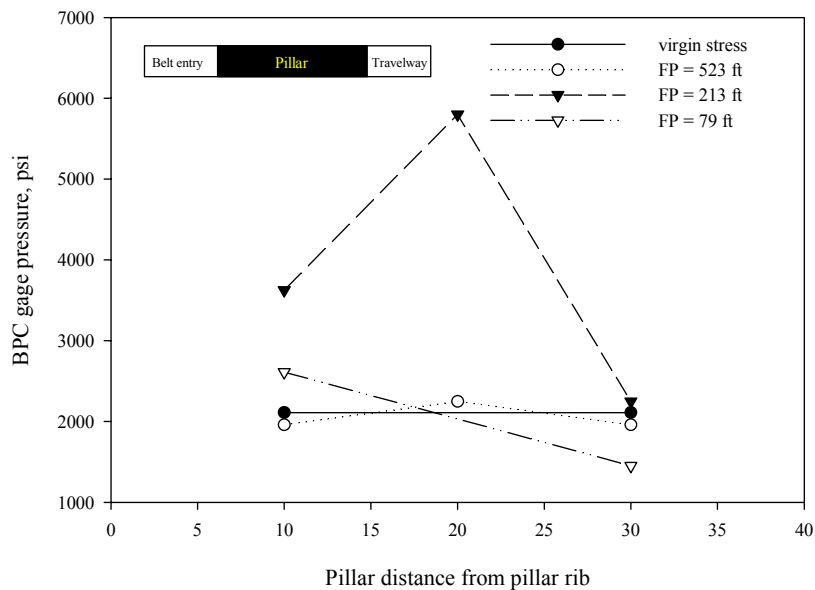
Figure 5-10 Ground pressure profiles for Site 2 [after Koehler, 1994]

As the mining progressed to the 213-ft inby FP (Figure 5-10), the BPC gage pressures increased noticeably because of the approach of front abutment pressure. The central BPC shows the highest pressure (5800 psi), which means that only a small portion in the pillar center, could be considered as the pillar elastic zone.

When the face reached the study site (79 FP), the pillar elastic zone was destroyed. Therefore the BPC gage pressures suddenly dropped across the pillar width.

Examination of the 79-ft inby FP profile reveals that the pillar pressures are approximately returned to the levels similar to those recorded at 523-ft inby FP. No coal bumps were known to have occurred in and around Site 2. The data shows that a significant portion of the pillar has yielded nonviolently.

5.3.2 Geology of Sunnyside mine

The Sunnyside No. 1 Mine portals are located near the base of a series of steep escarpments called the Western Book Cliffs. The cliffs rise sharply approximately 3,280 ft above the valley floor resulting in abrupt changes in mining overburden depth over very short horizontal distance. The overburden depth ranges from 328 ft at the outcrop to nearly 2950 ft at the study site.

The upper and the lower coal beds mined in the Sunnyside No. 1 Mine are considered splits of the Sunnyside coal bed. The split is not present everywhere, but at the mine site there is as much as 75 ft of siltstone between the upper and lower beds. Above and below the two coal beds are generally thin coal beds that thicken and thin, split, and disappear at regular intervals. Sandstone, siltstone, and sandy siltstone beds are interchanged with all coal beds [Scheibner, 1979]. The gate road in which the study sites were conducted was located in the Lower Sunnyside seam. Typically, the lower Sunnyside seam is 3.3 - to 6.6 –ft thick.

The roof strata of Sunnyside No. 1 mine are characterized by significant changes in the thickness of individual roof units over short lateral distance. Figure 5-11 illustrates the widely varying nature of roof lithologies at three consecutive crosscuts, 37, 38 and 39 [Maleki, 1995]. Figure 5-11 shows that the roof could be composed mainly of strong layer of siltsone as in crosscut 37, or it could be mainly composed of weak layers of mudstone. The yielding behavior of coal pillars was greatly affected by the type of immediate roof; i.e. siltstone or mudstone.
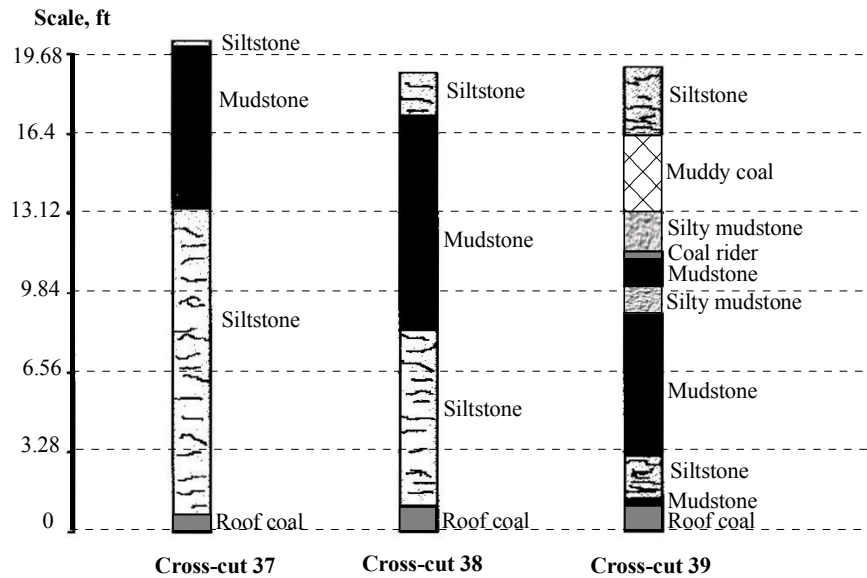
Figure 5-11 Roof logs illustrates at Sunnyside Mine [after DeMarco, 1995]

Generally, five rock types are found in the immediate roof, floor, and interburden between the Lower and Upper beds at study sites [DeMarco, 1996]:

- Dark-brown mudstone,
- Gray-brown silty sandstone,
- Interbedded siltstone and sandstone,
- Fine-grained quartoze sandstone, and
- Fine-grained calcareous sandstone.

The idealized geological model for study sites is shown in Figure 5-12. Each layer of this model is composed of a single homogeneous material. The material parameters used to simulate these layers are given in Table 5-1 [Agababian, 1978].
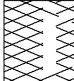
	Rock type	Thick., ft
	Calcite Sandstone	60
	Quartoze Sandstone	40
	Coal	6`
	Calcite Sandstone	26
	Calcite Siltsone	7
	Coal Shale	3
	Mined Coal	7
	Coal Shale	3
	Quartoze Sandstone	60

Figure 5-12 Idealized geological column for Sites 1 and 2

Table 5-1 In-situ material properties for rock mass at Sites 1 and 2

Rock type	Young's modulus x10^6, psi	Poisson's ratio	UCS, psi	D-P friction angle*, α deg	Density lb/ft^3
Fine-grained calcareous sandstone	2.06	0.05	3,900	61.5	162
Coal	0.58	0.23	1,000	50.9	82
Interbedded siltstone and sandstone	2.06	0.05	3,900	61.5	162
Gray-brown silty sandstone	6.15	0.18	5,800	50.6	170
Dark-brown mudstone	1.12	0.1	1,400	57	152
Fine-grained quartoze sandstone	1.9	0.07	3,600	46.4	154

5.3.3   Field simulation

Despite the high overburden depth of 2,600 ft at Site 1, the field data indicated that the 55-ft wide pillars yielded little from development until onset of the front abutment. Therefore, most of the abutment loads were carried by the elastic zone of the 55-ft wide pillars which could lead to pillar bumps. On the other hand, the 40-ft wide pillars at Site 2 began to yield after development. Further pillar yielding occurred with the onset of front abutment pressure. No pillar bumps and more pillar yielding were reported for 40-ft wide pillars. The data collected at the site suggested that the 40-ft wide pillar was a proper yield pillar dimension for mining conditions at Sunnyside mine.

Three-dimensional finite element models were constructed for Sites 1 and 2. The results of the FE calculations served two distinct purposes:

1. Validation of the calculations and
2. Investigation of coal bumps mechanism.

The first of these purposes is accomplished by comparing the field pressure measurements with the corresponding results obtained from calculations. Because the pillar bumps occurred when the face reached the study site (0 FP), it is important to make such a comparison during mining. The second purpose involves the investigation of coal bumps mechanism. Such investigation frequently requires information that is unavailable from mine measurements; such as pillar energies, pillar stress-strain curve, etc.

The ABAQUS finite element code [ABAQUS, 1998] was employed to simulate the complex in-situ coal pillar yielding mechanisms. Because of the potentially large model size, two-step modeling technique was employed using the global models and sub-models. 3-D finite global models were created to simulate the geological column shown in Figure 5-12 and the mine plan shown in Figure 5-6. At the seam level, the global models considered five blocks of chain pillars, half of the 23rd panel and 100 ft of the 24th panel. The dimensions of the global models were 495 ft x 625 ft x 212 ft and 480 ft x 625 x 212 ft, for Sites 1 and 2, respectively (Figure 5-13). The model consisted of 8-node brick elements. Symmetrical conditions were assumed at the middle of the 23rd left Panel.

The remaining three side-boundaries and the bottom boundary of the global models were roller-constrained. Simulation of pillar-rock interface was ignored in the global models.

Site 1

Site 2
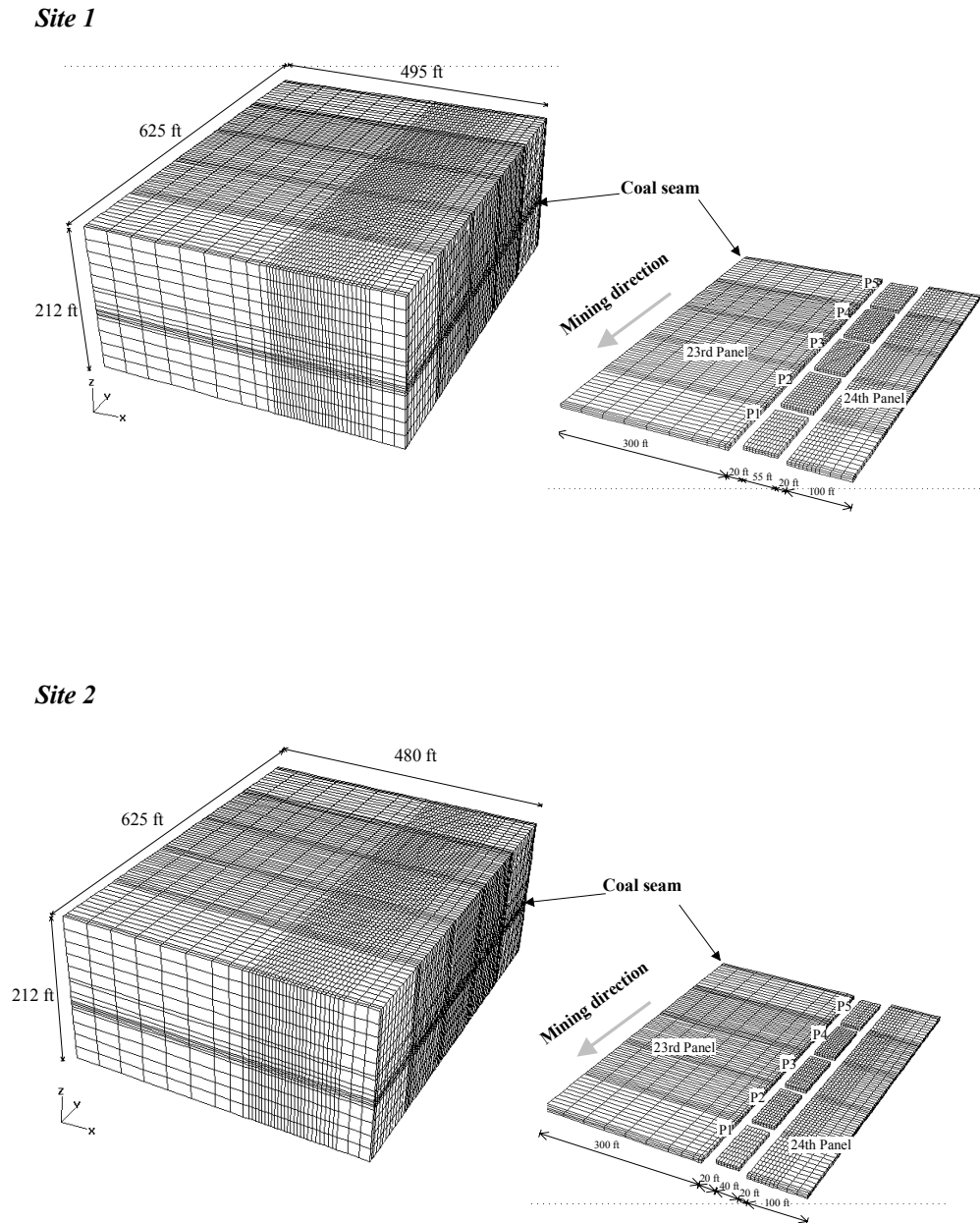
Figure 5-13 FE global models configurations for Sites 1 and 2

The global model was solved in three steps corresponding to the three different mining stages: geostatic, development, and panel retreat. During the geostatic stage, the in-situ stresses were applied and the gob elements were removed. The virgin horizontal stress was applied as a ratio of the vertical stress, as illustrated in Equation 5-6.

$$\sigma_h = \frac{\nu}{1-\nu}\sigma_v \qquad \qquad \textbf{Equation 5-6}$$

where σ_v is the virgin vertical stress; and ν is the Poisson's ratio of coal.

In the development stage, the gateroads of 20-ft wide were removed. In the panel retreat stage, the 23rd panel was passed pillar P3 (Figure 5-13). During the panel retreat, a gob height equivalent to 5 times of mining height was replaced by gob elements. Gob model described in Chapter 3 was used to model the gob created by longwall mining. Perfect elastic-plastic Drucker-Prager materials were assumed for both rock strata and coal pillars in the global models.

Using the sub-modeling features in ABQUAS, the sub-model for the pillar of interest P3 was created. The sub-model was solved in three steps the same as the global model: geostatic, development, and panel retreat. For each step, the sub-model was solved in a number of increments; i.e. small displacement analysis. This procedure can allow us to monitor the behavior of the sub-model during each step. A detailed simulation for the coal/rock interaction and strain softening model for coal pillar were considered in the sub-model. Perfect elastic-plastic Drucker-Prager materials were assumed for rock strata. The Coulomb friction model with shear limit, described in Chapter 3, was implemented. The interfacial coefficient of friction was assumed to be 0.25. The shear limit of coal/rock interface is the only unknown geotechnical parameter. Because the immediate roof changes significantly throughout the studied gateroad, the shear limit of coal/rock interface should be expected to change accordingly. The collected data at Site 1 shows little pillar yielding. Therefore, high values of coal/rock interface shear limits (325 psi and 500 psi) were tried at Site 1 to match the in-situ measurements with the modeling results. On the other hand, the pillar at Site 2 was completely yielded with the approach

of front abutment pressure. Therefore, lower values of coal/rock interface shear limits (150 psi and 325 psi) were tried at Site 2.

Figure 5-14 shows the vertical stress distribution at section A-A of the studied pillar at Site 1 at panel retreat stage. Also, Figure 5-14 shows the in-situ pillar pressures at face positions (FP), 0 and 26 ft. Irrespective of the coal/rock interface shear limit, Figure 5-14 shows higher vertical stresses at the belt-entry side of the pillar. A coal/rock interface shear limit of 500 psi shows stress values closer to the in-situ measurements, especially at the belt-entry side of the pillar.
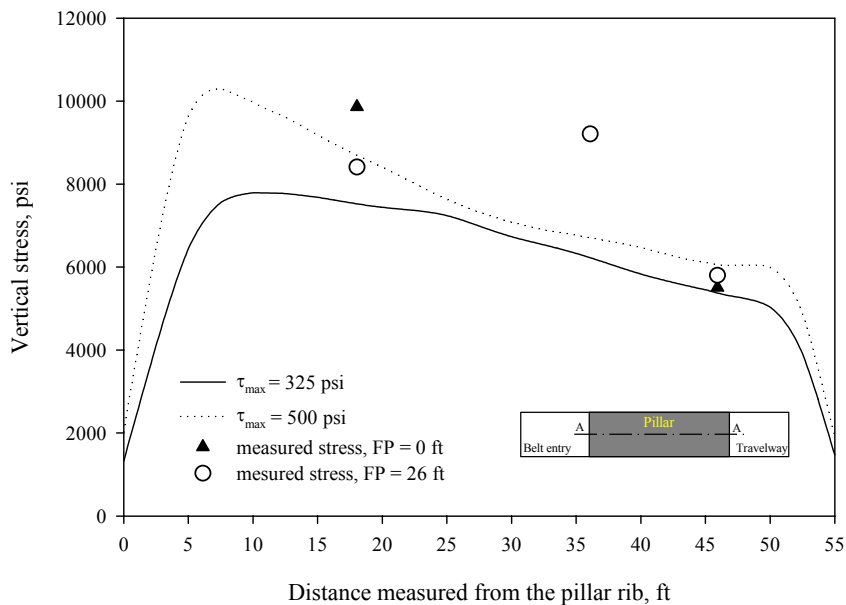
Figure 5-14 Pillar vertical stress distribution at Site 1

Figure 5-15 shows the plastic strain distribution for the studied pillar at panel retreat stage, assuming coal/rock interface shear limit of 500 psi. Figure 5-15 shows large yielding zones at the pillar corners. In spite of the high overburden depth and the front abutment pressure, Fig. 5-15 shows that the studied pillar has a large elastic zone as observed by field measurements. A yielding zone of 7.5 ft was predicted at pillar rib near the belt-entry side. Only a difference of 2.5 ft was observed between the in-situ yield zone measurements and numerical modeling prediction.
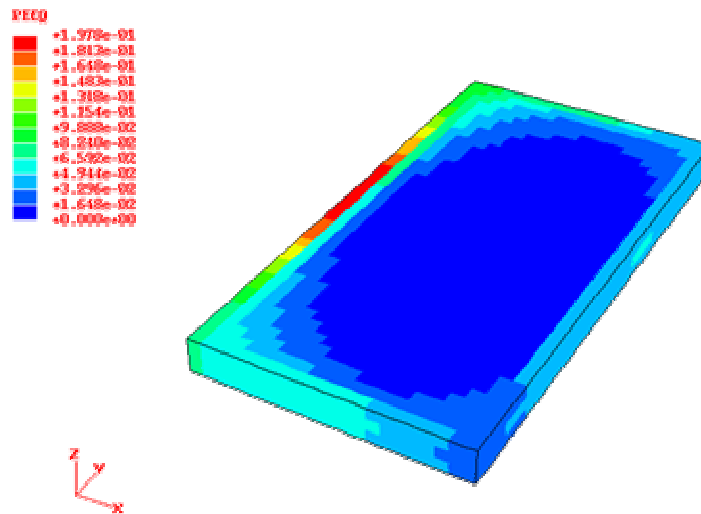
Figure 5-15 Pillar plastic strain fringes at Site 1

Figure 5-16 shows the vertical stress distribution at section A-A of the studied pillar at Site 2, for development and panel retreat stages. For development stage, the vertical stress prediction associated with 150 psi coal/rock shear limit, shows better agreement with the in-situ measurements. For panel retreat stage, the vertical stress distribution associated with a coal/rock interface shear limit of 325 psi, shows high stress values and stress concentration at the belt-entry side of the pillar. These results contradict with the in-situ measurements. On the other hand, the vertical stress distribution associated with a coal/rock interface shear limit of 150 psi, shows stress values closer to the in-situ measurements and stress transformation towards pillar center.

Figure 5-17 shows the plastic strain distribution for the studied pillar at panel retreat stage, assuming coal/rock interface shear limit of 150 psi. Figure 5-17 shows that the pillar was completely yielded which match with field observation. Larger plastic strain values were predicted near the belt-entry pillar side because of the front abutment pressure.

A. Gateroad development
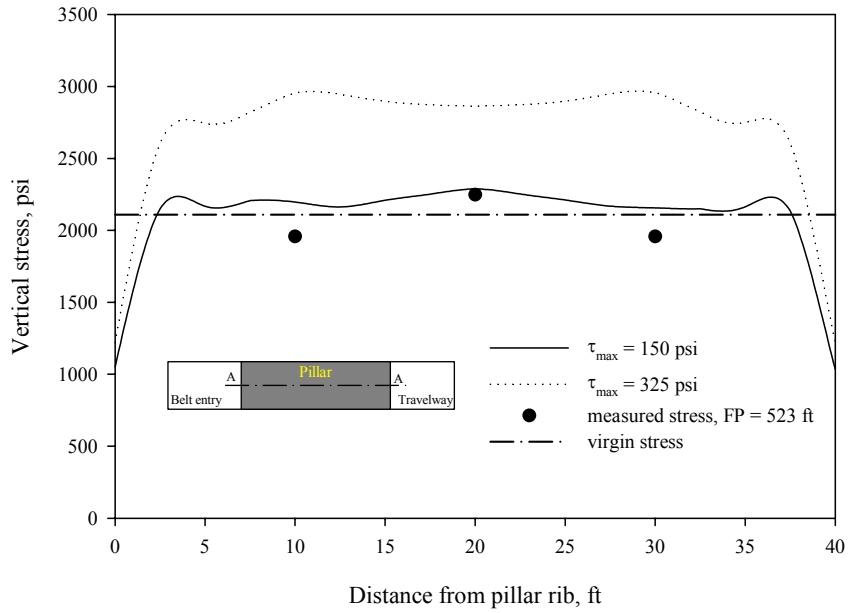
B. Panel retreat
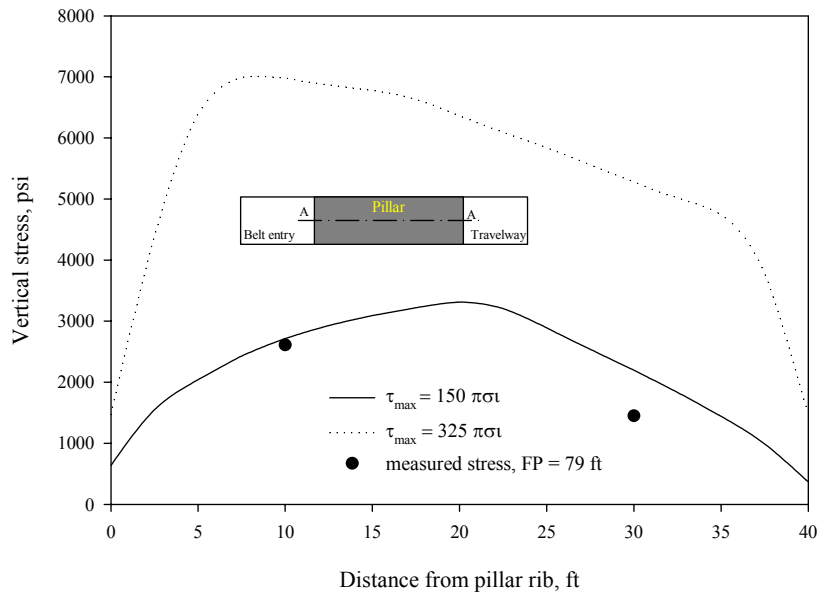
Figure 5-16 Pillar vertical stress distribution at Site 2

From the above discussions, coal/rock interface shear limits of 500 psi and 150 psi were found to be more suitable for Sites 1 and 2, respectively. The difference between the proposed coal/rock interface shear limits at Sites 1 and 2, could be explained by the continuously changes in the immediate roof in the studied gateroad. A large horizontal distance of 2310 ft is observed between Sites 1 and 2, Figure 5-1.
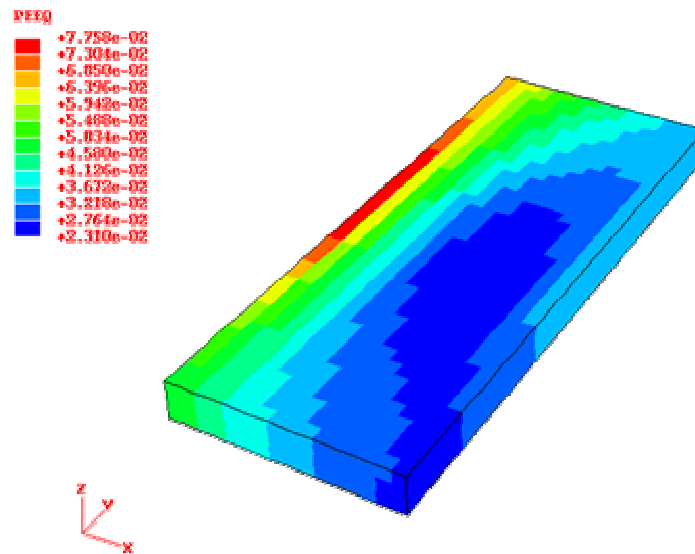
Figure 5-17 Pillar plastic strain fringes at Site 2

5.3.4   Pillar stability evaluation

The proposed method for evaluating the stability of yield pillars was applied at Sites 1 and 2. The results of these evaluations will serve the following objectives:

- To define the thresholds for stability measures, namely; core stability factor CSF, pillar bump index PBI, and rib instability factor RIF.
- To assess the concepts that introduced in the design methodology.
- To achieve a better understanding for the proposed methodology.

Before starting the evaluation, it is worthy to summarize the stability condition at study Sites 1 and 2.

For Site 1, the field observations could be summarized as follows:

- During the panel retreat, the pillar at Site 1 was able to gain extra load without further yielding.
- An increase in the frequency and magnitude of rock noise was observed after development. These activities ranged from coal bounces to minor coal bumps.
- Heavy bump activity started at the chain pillars immediately inby the study site.

For Site 2, the field observations could be summarized as follows:

- A significant portion of the pillar has yielded after development.
- No coal bumps were known to have occurred in and around Site 2.
- The pillar was completely yielded during the panel retreat.

5.3.4.1 Stability evaluation for Site 1

Figure 5-18 shows a relationship between the average vertical stress and average vertical strain of pillar in Site 1 during development and panel retreat. It is well known that the stress and strain distributions inside the pillar are not uniform, but the average stress-strain relationship can illustrates a global view about the loading behavior of the pillar. Figure 5-18 shows that the maximum average vertical stress of 3685 psi was observed right before the end of the development stage. During the panel retreat the pillar starts reloading again and the average vertical stress inside the pillar reached a value of 6036 psi. The pillar P3 at Site 1 showed a strain hardening behavior during the panel retreat.
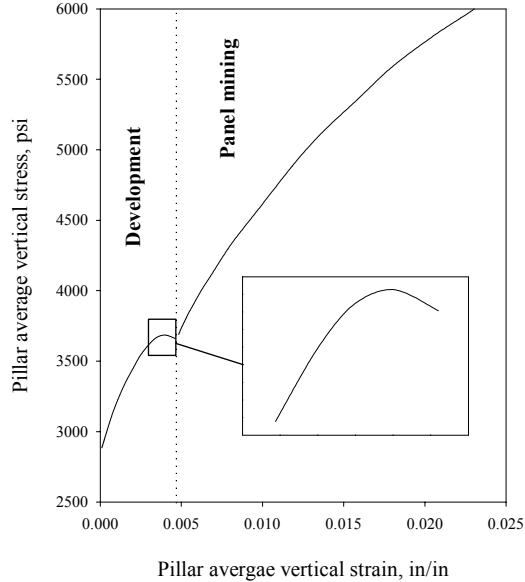
Figure 5-18 Average stress-strain curve for pillar P3, at site 1

A detailed analysis for the stress condition inside pillar P3 can be achieved by considering the different loading zones within the pillar. Figure 5-19 shows the three loading zones; namely, core, transition and rib zones, after the development stage. Figure 5-19 shows the pillar loading zones at different pillar sections; bottom, middle and top sections at distance of 2.33 ft, 4.67 ft and 6.99 ft measured from the mine floor, respectively. Figure 5-19 shows that the core and transition zones represent large percentage of the pillar volume, 47 % and 40%, respectively while the rib zones only represents 13%. The rib zone occupied pillar corners and ribs.

Figure 5-20 shows the pillar loading zones at three sections across the pillar when the face approached the pillar from its left side. The figure shows that the core zone disappeared completely while the transition and rib zones increased. The percentages of the transition and rib zones were 78% and 22% of the pillar volume, respectively. Because the panel was retreating from the left side of the pillar, larger rib zones were observed at the left side of the pillar compared with the right side.

Bottom section · Middle section · Top section

Core zone
Transition zone
Rib zone
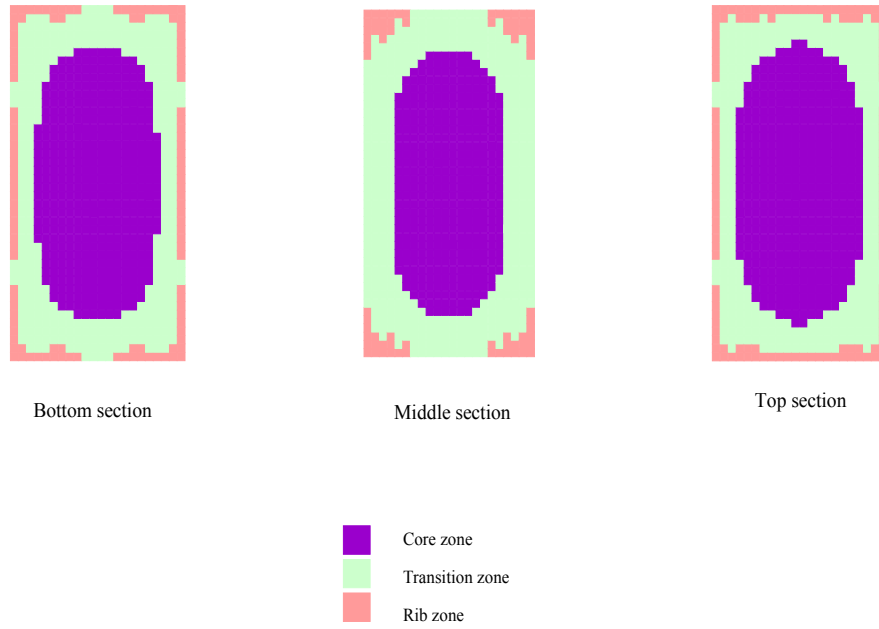
Figure 5-19 Pillar zones at different sections after development, Site 1

Panel retrat

Bottom section · Middle section · Top section

Transition zone
Rib zone

Figure 5-20 Pillar zones at different sections during panel retreat, Site 1

Figure 5-21 shows the stress-strain relationships for three elements located in the middle section of the pillar. The solid parts of the stress-strain relationships represent the development stage while the dashed ones represent the panel retreat stage. Element E1 is located at the rib zone with a coordinates of (2.5 ft, 100ft) measured from the left bottom corner of the section. Elements E2 and E3 are located in the transition zone with coordinates of (27.5 ft, 95 ft) and (0, 52.5 ft), respectively. The element E1 shows a strain softening behavior where the element shows a residual strength of 1000 psi. The transition zone shows a complex stress-strain behavior, where many load-deformation patterns can be observed. The element E2 shows a strain hardening behavior while element E3 shows a perfect plastic behavior. It is obvious that element E3 was part of the core zone during the development stage because it shows a relatively high stress value of 4000 psi during that stage. On the other hand, element E2 was part of transition zone in the development stage. Element E2 shows a strain softening behavior of high stress, 3277 psi, by the end of the development stage.
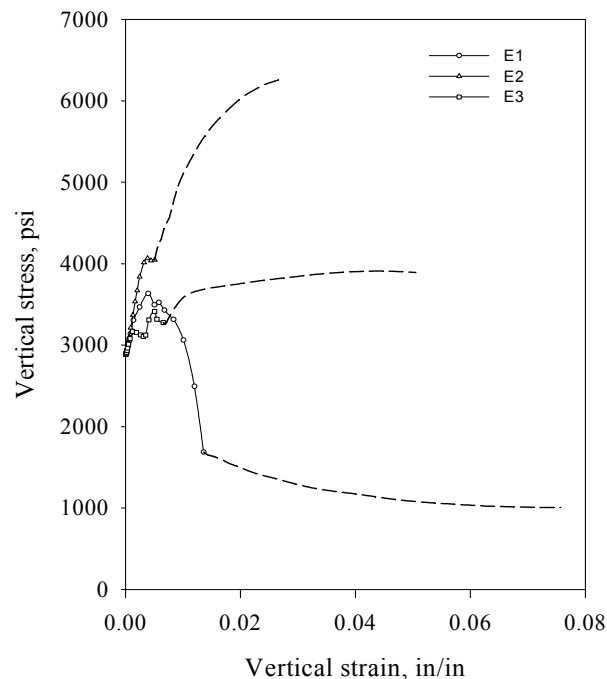
Figure 5-21 Stress-strain curves at different pillar zones, Site 1

An average stability factor CSF of 1.080 was estimated for the core zone after the development stage. The CSF of the core zone ranged from 1 to 1.190. Figure 5-22 shows the cumulative percentage for CSF. It shows that 75 % of the elements of the elastic zone have a SF less than 1.15 which means that most of the elements of the elastic zone were within 15% of their yielding strength. Therefore the elastic zone was considered in critical condition where there was a great tendency to release the stored elastic strain energy to the surrounding if the elastic zone started yielding.
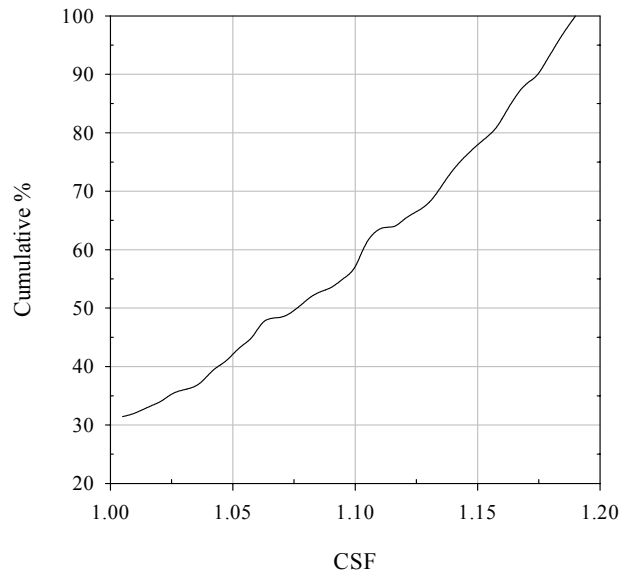
Figure 5-22 Cumulative plot for CSF of the elastic zone after development, Site 1

An average bump index BI of 9.570 was estimated for the transition zone after the development stage. The BI of the transition zone ranged from 0.266 to 21.766. Figure 5-23 shows the cumulative percentage for BI. It shows that 75 % of the elements of the transition zone have a BI less than 11. This might be one of the reasons for the observed coal bounces activities that observed after the pillar was developed.
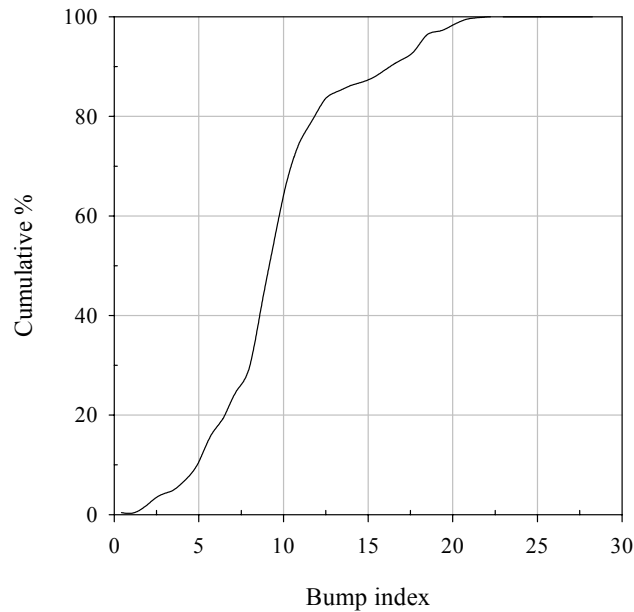
Figure 5-23 Cumulative plot for BI of the transition zone after development, Site 1

The analysis showed that all the elements within the core zone were transferred to transition zone during the panel retreat. Therefore a significant increase in the BI of the transition zone was expected. An average bump index BI of 18.882 was estimated for the transition zone when the panel reached the studied pillar. The BI of transition zone has been doubled because of the panel retreat. The BI of the transition zone ranged from 2.003 to 61.771.

Figure 5-24 shows the cumulative percentage for BI. It shows that 75 % of the elements of the transition zone have a BI less than 32. This means that most of the pillar has high bump index. The high BI is believed the main contributor for the coal bump events which were reported in Site 1.
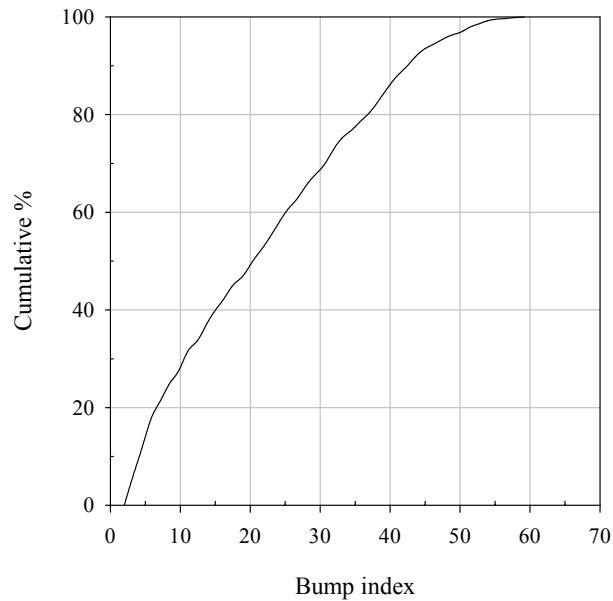
Figure 5-24 Cumulative plot for BI of the transition zone during panel retreat, Site 1

The rib zone represents a significant portion of the pillar volume at the stage of mining; i.e. 13 %. An average Rib Instability Factor RIF of 1.761 was estimated for the rib zone after the development stage. The RIF of the rib zone ranged from 1 to 3.99. Figure 5-25 shows the cumulative percentage for RIF. It shows that 75 % of the elements of the rib zone have a rib instability factor less than 2.1.

The analysis showed that some of the elements of the transition zone were transferred to rib zone during the panel retreat, especially those elements at the boundaries between the two zones. Most of those transferred elements were already yielded during the development stage but they were subjected to a high confinement. Therefore the minimum post peak slopes of those transferred elements were much larger the minimum post peak slopes of the rest of elements of the rib zone. The rib zone represents 22 % of the pillar's volume at the retreat step. An average RIF of 1.832 was estimated for the rib zone when the panel reached the studied pillar. The RIF of the rib zone ranged from 1.0 to 5.921. Figure 5-26 shows the cumulative percentage for RIF. It shows that 75 % of the elements of the rib zoon have a RIF less than 2.2.
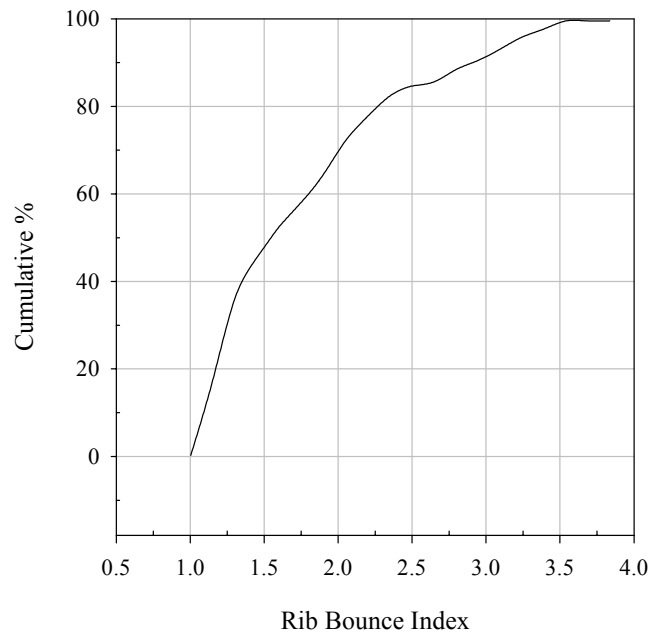
Figure 5-25 Cumulative plot for RIF of the rib zone after development, Site 1
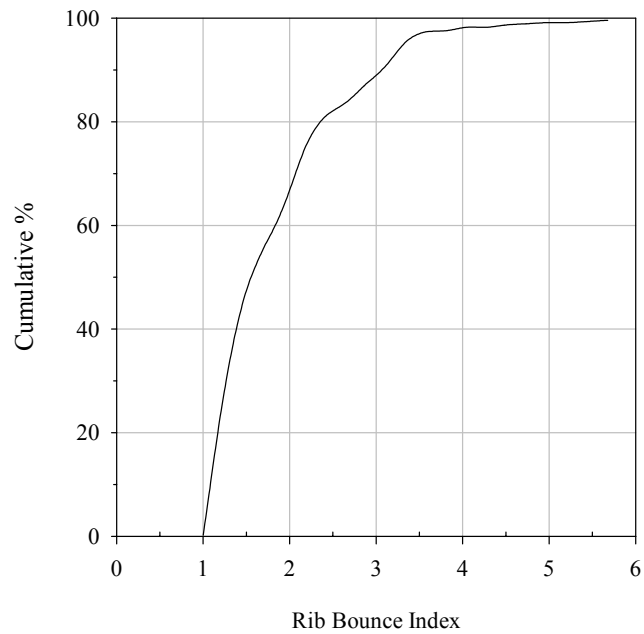
Figure 5-26 Cumulative plot for RIF of the rib zone during panel mining, Site 1

5.3.4.2 Stability evaluation for Site 2

Figure 5-27 shows a relationship between the average vertical stress and average vertical strain of pillar in Site2, during the development and panel retreat. Figure 5-27 shows that all the pillar's elements have passed the yield strength after the development stage. The maximum average vertical stress of 2410 psi was observed at the early stages of pillar development, which means that the pillar reached its ultimate strength right after it was developed. By the end of the development the pillar average vertical stress dropped to 1580 psi. During the panel retreat the pillar maintained the same stress level. Generally, the pillar P3 at Site 2 showed a strain softening behavior during the panel retreat.
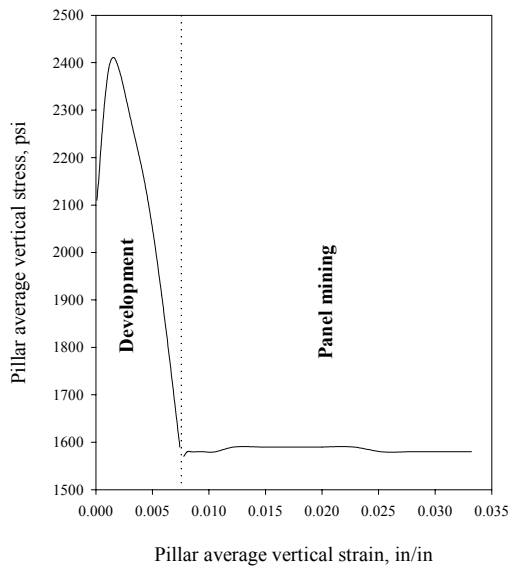
Figure 5-27 Average stress-strain curve for pillar P3, at site 2

As mentioned earlier, the FE models were solved in small increments at each step of mining. Therefore a detailed monitoring for model outputs, such as stress, strain, displacement, energy, etc can be conducted during model solution for each step. Figure 5-28 shows the propagation of pillar loading zones, i.e. core, transition and rib zones, at the middle section of the studied pillar during its development. At early stages of loading, i.e. 14% of the total load, the pillar was completely in the elastic stage where only the elastic

core zone was observed. At 62% of the total load, the core zone shrinks while the rib zones observed at the pillar four corners. The transition zones occupied the pillar's ribs. This process continued until the elastic zone was completely disappeared at 92 % of the total load. At that stage the rib zones covered the front and back ribs of the pillar. At 100 % of total load the rib zones propagated toward the pillar core while the transition zones covered smaller portions of the pillar center.
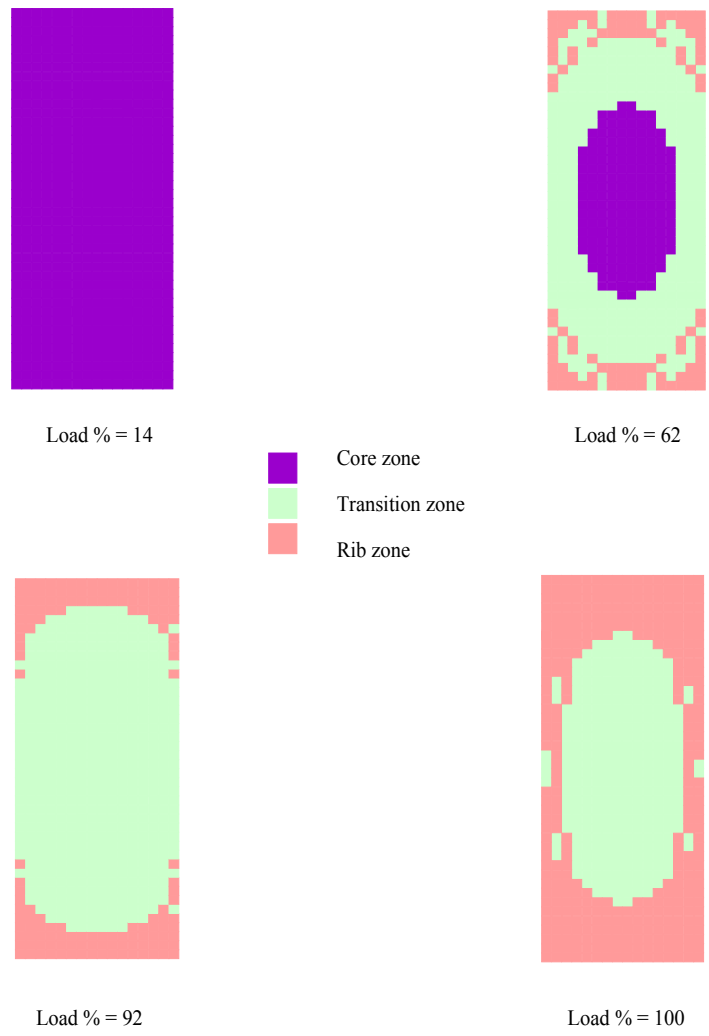
Figure 5-28 Propagation of pillar zones during development stage, Site 2

Bottom section   Middle section   Top section

Transition zone

Rib zone
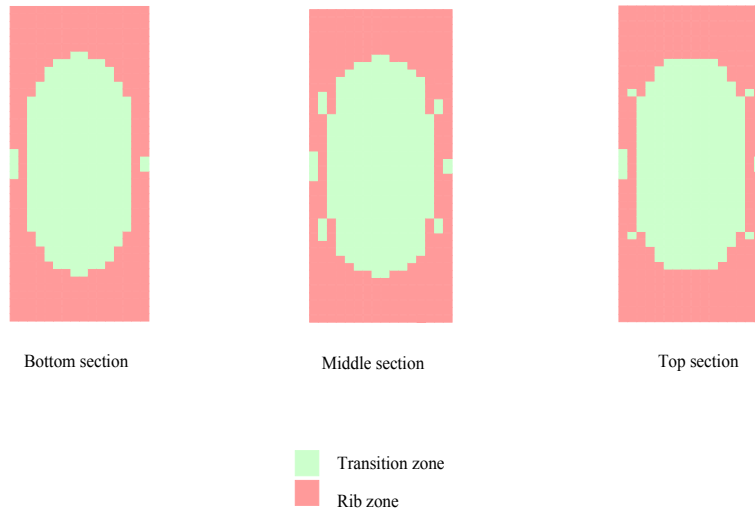
Figure 5-29 Pillar zones at different sections after development, Site 2

Figure 5-30 shows the pillar loading zones at three sections across the pillar when the face approached the pillar from its left side. The percentages of the rib and transition zones were the same as in development stage, i.e., 46 % and 54 % of the pillar volume, respectively. This could be explained by that the pillar reached its residual strength during the panel retreat, Figure 5-27. Therefore no expected changes in the pillar post-peak stiffness during the panel retreat.

Bottom section   Middle section   Top section
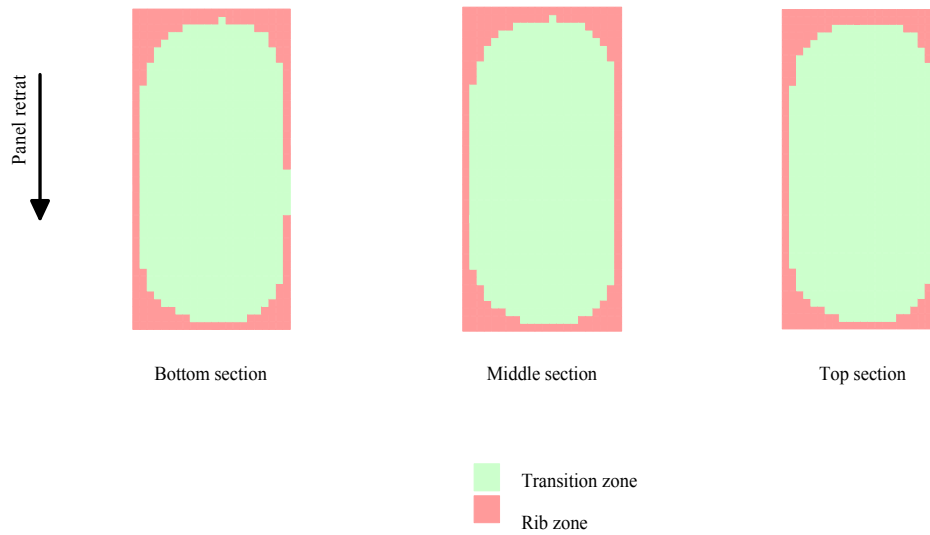
Transition zone

Rib zone
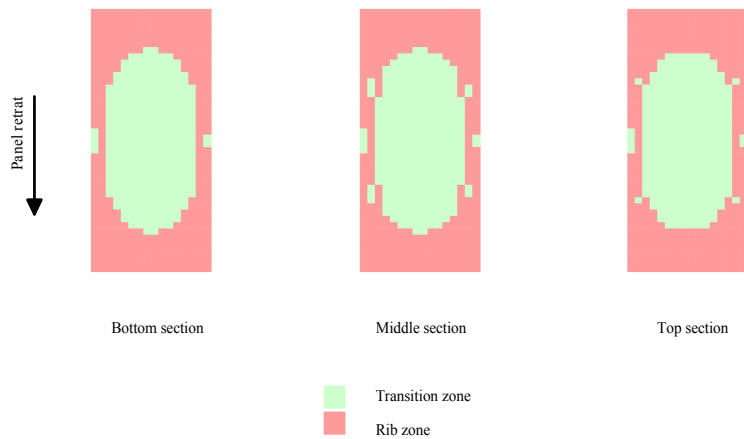
Figure 5-30 Pillar zones at different sections during panel retreat, Site 2

Figure 5-31 shows the stress-strain relationships for four elements located in the middle section of the pillar. The solid parts of the stress-strain relationships represent the development stage while the dashed ones represent the panel retreat stage. Elements E1 is part of rib zone while elements E1, E2 and E4 are part of transition zone. Element E1 is located at the left bottom corner of the section. The stress-strain behavior of element E1 is the typical pattern for the rib zone. Element E1 showed a strain softening behavior with a residual strength of 360 psi. Elements E2, E3 and E4 are located in the transition zone with coordinates of (2.5 ft, 62.5 ft), (25 ft, 50 ft) and (20 ft, 50 ft) measured from the left bottom corner of the section, respectively. The transition zone showed a complex stress-strain behavior. More than one load deformation pattern can be observed in the transition zone. The stress-strain behavior of element E2 is the typical pattern for the transition zone. By the end of the development stage, element E2 showed a strain softening behavior of high post-peak stress of 2210 psi. During the panel retreat, element E2 continued to strain softening with a high residual stress of 1743 psi. At the end of the development stage, elements E3 and E4 showed softening behaviors with high post-peak stresses. Elements E3 and E4 showed a strain hardening behavior during the panel retreat. The in-situ horizontal stress at Site 2 was 904 psi. After the pillar development, the minor and intermediate principal stress at element E3 was 329 psi and 868 psi, respectively. When the face passed by the study site, the minor and the measure horizontal stresses at element E3 increased to 406 psi and 1083 psi, respectively. Therefore, element E3 was part of softening during the development stage then it became part of the transition zone when the face approached the study site. On other hand element E4 was part of transition zone during development and panel retreat stages.

An average bump index BI of 1.711 was estimated for the transition zone after the development stage. The BI of the transition zone ranged from 0.723 to 2.727. Figure 5-32 shows the cumulative percentage for BI. It shows that 75 % of the elements of the transition zone have a BI less than 2.15. The average BI for Site 2 is approximately 1/5 of the Site 1 at the development stage. This could explain why the condition was more quite at Site 2 compared with Site 1.
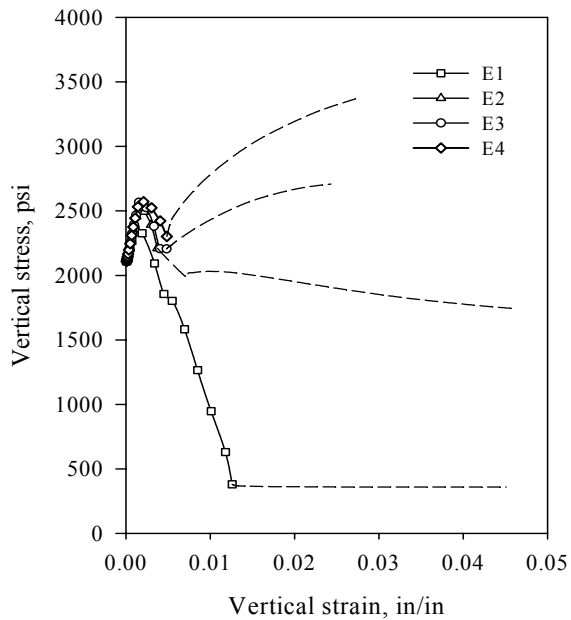
Figure 5-31 Stress-strain curves at different pillar zones, Site 2
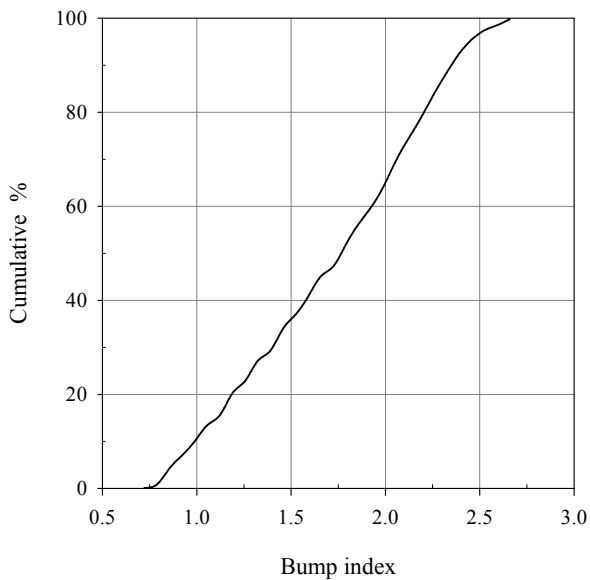
Figure 5-32 Cumulative plot for BI of the transition zone after development, Site 2

Unlike Site 1, the BI is decreased in Site 2 during the panel retreat. An average bump index BI of 0.533 was estimated for the transition zone of Site 2 when the face reached the studied pillar. This could be explained by the strain softening behavior of the transition zone during panel retreat in Site 2. On the other hand, the main pattern for transition zone of Site 1 was strain hardening. The BI of the transition zone of Site 2 ranged from 0.05 to 1.41. Figure 5-33 shows the cumulative percentage for BI. It shows that 75 % of the elements of the transition zone have a BI less than 0.70. This means that most of transition zone has a low tendency for coal bumps which match well with the field observations at Site 2.
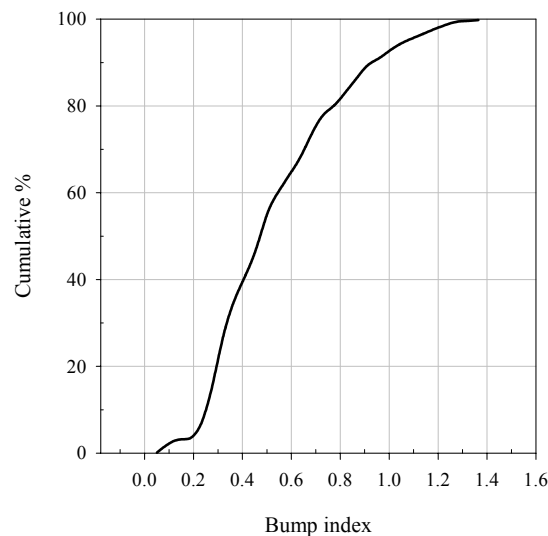
Figure 5-33 Cumulative plot for BI of the transition zone during panel retreat, Site 2

Figure 5-34 shows a 3D plot for the bump index at Sites 1 and 2 during panel retreat. The BI distributions were taken at the mid-height section of pillar P3. The Figure shows BI distribution irrespective of the loading zone. Figure 5-34 shows relatively high BIs near the pillar center for both Sites 1 and 2. The calculated bump indices for rib zones were relatively small at Sites 1 and 2. This observation indicates that the bump index measure is not suitable to evaluate the stability of softening zone. Also, it confirms the previous observation that the high BI at transition zone of Site 1 was the major contributor for the coal bump at that site.

Site 1

_ _ _ _ _   Rib/Transition boundary

Site 2
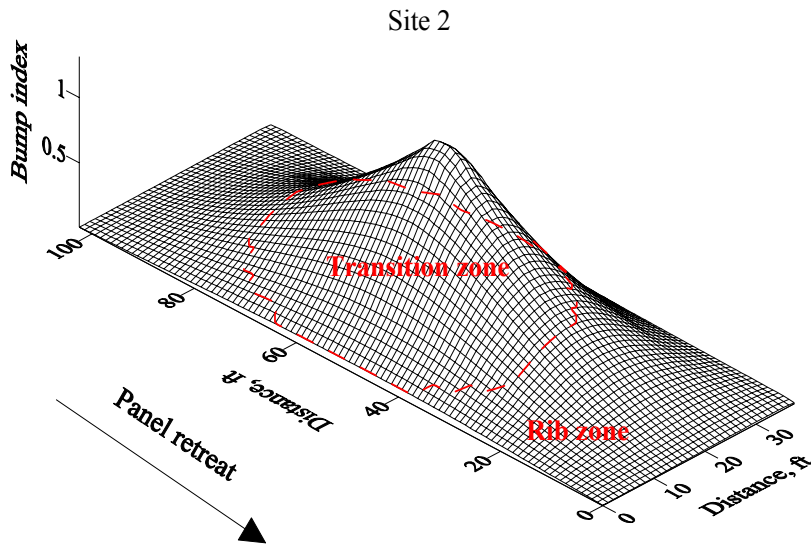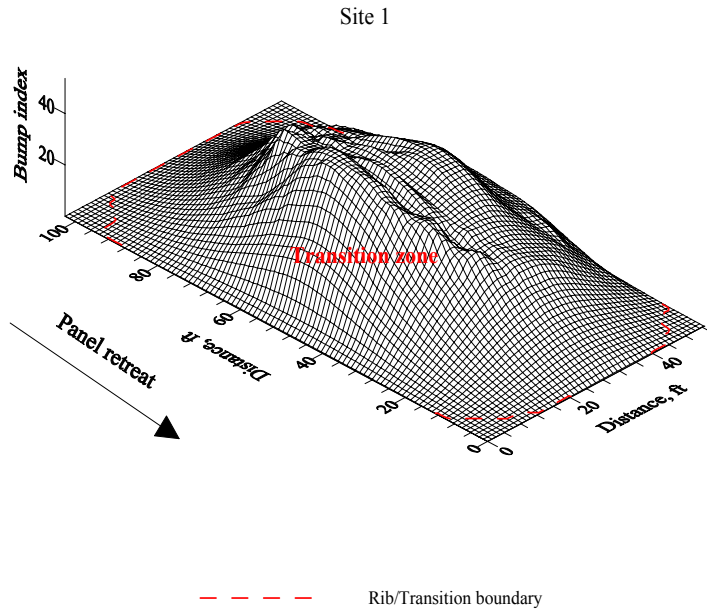
Figure 5-34 Distribution of bump index of pillar P3 at Sites 1 and 2, during panel retreat

The rib zone represents 46 % of the pillar's volume after the development step. An average RIF of 1.699 was estimated for the rib zone after the development stage. The RIF of the rib zone ranged from 1 to 4.502. Figure 5-35 shows the cumulative percentage for RIF. It shows that 75 % of the elements of the rib zone have a RIF less than 1.99. Compared to Site 1, the average RIF for Site 2 was slightly smaller by a difference of 0.062. The absolute average of post-peak stiffness for rib zones of Sites 1 and 2 are $2.21*10^5$ psi and $1.96*10^5$ psi, respectively. The absolute average of local mine stiffness for rib zones of Sites 1 and 2 are $1.25*10^5$ psi and $1.23*10^5$ psi, respectively. It is obvious that there is insignificant difference for K_{LMS} between Sites 1 and 2. This is because the same immediate roof and floor were presented in both sites. The rib zone in Site 2 showed smaller absolute average value for the post-peak stiffness. This is due to the rib zone in Site 2 was much larger and included elements that near the pillar core with higher confinement. On other hand the rib zones in Site 1 were concentrated at the pillar corners and ribs of less confining.
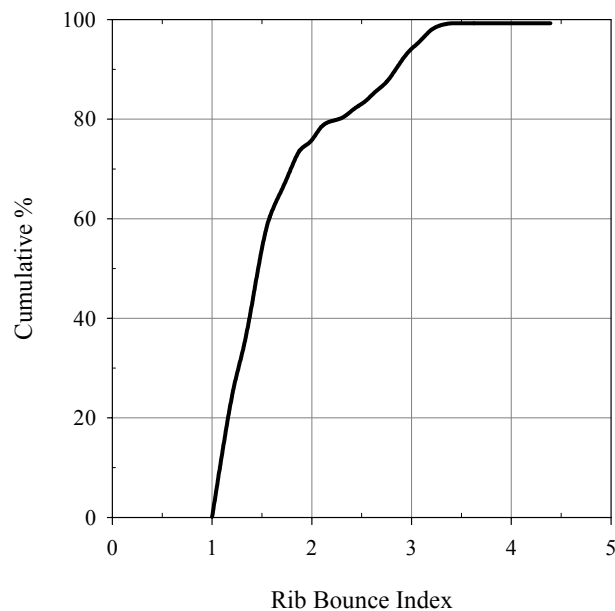
Figure 5-35 Cumulative plot for RIF of the rib zone after development, Site 2

Compared with the development stage, the ratio of rib zone didn't change due to panel retreat. This is because the pillar had reached its residual strength during the development stage. Therefore no significant changes were expected for the rib zone post-peak stiffness in the retreat stage. A rib instability factor RIF of 1.70 was estimated for the rib zone when the face reached the studied pillar of Site 2. Similar to the development stage, there is an insignificant difference in RIF for Sites 1 and 2 during panel retreat.

Considering both the rib zone ratio and the rib instability factor, Site 2 was expected to have more coal bounces compared with Site 1. But the field observations were not conclusive about this result. The field observations in Site 1 explained the noise activities during the development stage as either coal bounces or minor coal bumps. From the above discussion, it is believed that these noise activities were due to coal bumps rather than rib bounces.
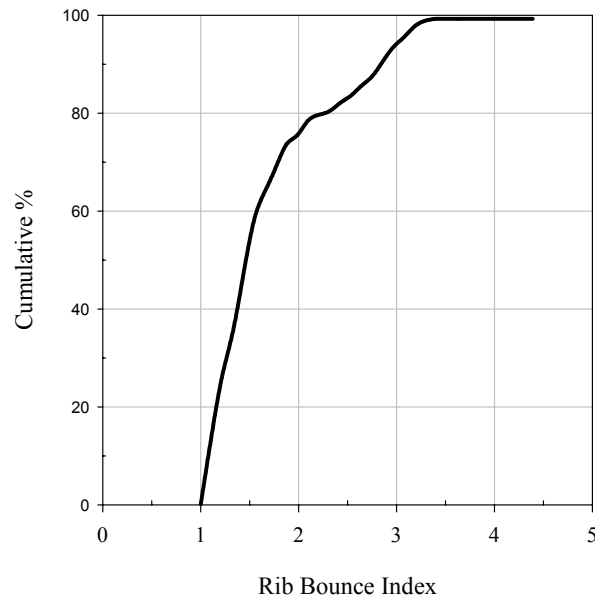
Figure 5-36 Cumulative plot for RIF of the rib zone during panel mining, Site 2

5.4 Summary

In this chapter a new method for evaluating the stability of yield pillar was evaluated. The proposed method considered the non-homogeneity of yield pillar by dividing the yield pillar into three loading zones; namely core, transition and rib zone. An appropriate stability criterion was assigned for each loading zone. A case study of unsuccessful yield pillar design associated with coal bumps and another stable design was used to assess the proposed method. The proposed method was able to evaluate the stability of yield pillar systems in both designs. The evaluations elaborated some important features for the proposed method, such as:

- The proposed coal model was able to show different stress-strain behaviors inside the pillar.
- Based on the amount of confinement inside the pillar, the yield pillar could be divided to three loading zones.
- The size and stability of loading zones depend on the mining stage.
- The rib instability factor for evaluation the stability of rib zone was more relevant to the development stage.
- The BI was meaningful only for the transition zone.

CHAPTER 6

NEW METHOD FOR YIELD PILLAR DESIGN

A number of yield pillar design methods were discussed in detail in Chapter 3. These methods define the yield pillar as the one that is completely yielded by using the conventional concept of pillar design. In fact, any rational design for yield pillar should consider the stability of yield pillar in the post-peak region of its loading curve; i.e. after it yields. Moreover, none of these methods had provided any criterion to evaluate the stability of yield pillar against the risk of coal bumps.

In Chapter 5, a new method of evaluating the stability of yield pillars has been proposed. This method tried to overcome the deficiency of the previous design methods. The proposed method provides a number of pillar stability measures to evaluate the pillar stability during mining stages, i.e. development and panel retreats. The proposed method was evaluated by a case study and it was found hopeful.

To formulate the proposed evaluation method into a design methodology, a statistical screening analysis for the geological and geometrical factors was conducted. Therefore the factors that have greatest effects on the proposed stability measures can be defined. In this chapter an interpolation model for estimating the pillar stability measures was developed. This model is based on a fairly large database that correlates the proposed stability measures and the geological and geometrical factors. The database was established by conducting more than 432 three-dimensional finite element models. Finally, a design algorithm for yield pillar design was proposed and evaluated by three case studies in addition to the Sunnyside case described in Chapter 5.

6.1 Stability Measures of Yield Pillars

Throughout this discussion, it is assumed that the pillar is composed of a number of elements. Despite of the pillar size, the dimensions of the pillar's elements were held

constant at 2.5 ft x 2.5 ft x 2.67 ft. The stability measures introduced in Chapter 5 aimed to evaluate the stability of yield pillars in all stages of mining. These measures evaluate the pillar stability in both the elastic and post-peak regions of pillar loading curves.

♦ **Pillar Yield Ratio, PYR**

The PYR is a measure of the amount of pillar yielding at a mining stage. The PYR is defined as the ratio of the yielded portions in the pillar to the total volume of the pillar, it is defined by:

$$PYR = \frac{N_y}{N_T}$$

<div align="right">**Equation 6-1**</div>

where N_y is the number of yielded elements in the pillar. The element is considered to be yielded once it shows a plastic deformation; and N_T is the total number of elements in the pillar.

♦ **Core Stability Factor, CSF**

If a pillar still has an elastic core, the CSF provides a measure of stress level inside that core with respect to its yielding stress. The CSF is defined as the average value of stability factors for the elements in the elastic core. To ease the calculations for the CSF, the Pillar Stability Factor PSF is estimated first. The PSF is estimated as an average value of stability factors for all the pillar's elements.

$$PSF = \frac{\sum ESF}{N_T}$$

<div align="right">**Equation 6-2**</div>

The Element Stability Factor, ESF can be estimated by Equation 5-3.

The CSF can be estimated from the PSF and PYR, as follows:

$$CSF = \frac{PSF - 1}{1 - PYR} + 1$$

<div align="right">**Equation 6-3**</div>

For a completely yielded pillars, i.e. PYR = 1, the elastic core will vanished. Because of small yield pillar widths and high overburden depths, the CSF of yield pillar is usually small. Through this study the PYR will be the only stress measure that represents the core zone.

♦ **Pillar Bump Index, PBI**

The pillar bump index (PBI) is a measure of the pillar stability with respect to coal bumps. The PBI is estimated as an average value for bump indices of all the pillar's elements. The element bump index, EBI can be estimated as follows:

$$EBI = \begin{cases} 0 & \rightarrow \text{for elastic elements} \\ \dfrac{W_e + W_v}{W_p} & \rightarrow \text{for yielded elements} \end{cases}$$

<div align="right">Equation 6-4</div>

where W_e is the stored elastic strain energy; W_p is the dissipated strain energy; and W_v is the dissipated energy in viscous damping. The component of dissipated energy in viscous damping can was calculated for elements that show numerical instability; see Section 3-1-2.

The PBI can be estimated by:

$$PBI = \frac{\sum EBI}{N_T}$$

<div align="right">Equation 6-5</div>

♦ **Rib Zone Ratio, RZR**

The RZR describes the ratio of the rib zone portion in the pillar to the total volume of the pillar, it is defined by:

$$RZR = \frac{N_r}{N_T}$$

<div align="right">Equation 6-6</div>

where N_r is the number of elements in the rib zone, defined by Equation 5-2.

Based on the definition of rib zone, Section 5-1-3, the RZR will be used to measure the rib zone instability for coal bounces. The larger the rib zone area, the higher the probability for coal bounces. As illustrated in Chapter 5, the RZR could be considered mainly in the development stages, because during this stage the pillar ribs are formed.

♦ **Roof-to-floor convergence, C**

The roof-to-floor convergence measures the degree of closure in the tailgate during the panel retreat-3. The amount of roof-to-floor convergence can reflect the amount of load imposed on the auxiliary supports. The roof-to-floor convergence at any location (i) along the cross-section x-x, is estimated as follows (Figure 6-1):

$$C_i = \delta_{r_i} + \delta_{f_i}$$
<div align="right">**Equation 6-7**</div>

where δ_{ri} is the downward roof displacement at location (i); δ_{fi} is the upward floor displacement at location (i).

The cross-section x-x extended from the T-junction to the next outby crosscut, as shown in Figure 6-1. The roof-to-floor convergence along the cross-section x-x, C is defined as follows:

$$C_i = \frac{C_i}{N_c}$$
<div align="right">**Equation 6-8**</div>

where N_c is the number of convergence stations along the cross-section x-x.
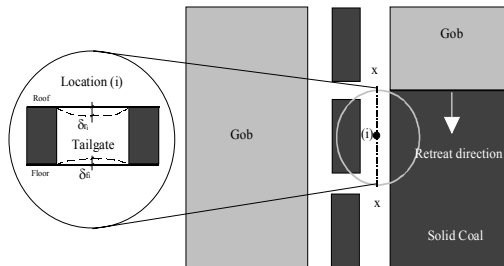
Figure 6-1 Roof-to-floor convergence locations

6.2 Screening Analysis for Geological and Geometrical Factors

The main objectives of the proposed pillar design method are to define the conditions that lead to pillar bumps and to provide a methodology for using the yield pillars to prevent the coal bumps. The geometrical and geological factors, presented in Chapter 2 of this research, can be classified into two types based on their effect on the yielding mechanism of pillar system:

1. **Insignificant factors** – The coal creep properties was found insignificant for yield pillar design [Tsang, 1993].
2. **Significant factors** – These factors can be classified into two types:
    a. Fixed factors - which are held constants in the study, such as :
        - In-situ coal strength, σ_c = 900 psi
        - Coal Poisson's ratio = 0.3
        - Coal Young's Modulus = 3.5×10^5 psi
        - Friction angle of coal-roof and coal-floor interfaces = 14°
        - Pillar length = 100 ft
        - Pillar height = 8 ft
        - Panel width = 900 ft
        - Entry width = 18 ft
    b. Non fixed factors – Table 6-1 summarizes these factors and their study ranges. In this research we will call these "non fixed factors" simply as "factors".

A full factorial design is used to evaluate the main and interaction effects of the factors listed in Table 6-1 on the yielding mechanism of pillar system. Therefore, 216 three-dimensional finite element models are required to consider all possible combinations of all levels of these factors. The same amount of models is required to estimate the local mine stiffness at development stage, as described in Chapter 3. A large amount of time and effort has to be spent in order to conduct these large numbers of finite

element models at different stages of longwall retreats. These models become more complicated if the coal/rock interface is considered.

Table 6-1 Geometrical and geological factors

Parameter	Level-1	Level-2	Level-3
Mining depth, Z in ft	1500	2000	2500
Shear limit of Coal/Rock interface, τ_{max} in psi	150	325	500
Roof/coal Young's modulus ratio, E_r/E_c	4	-	10
Roof/coal uniaxial compressive strength ratio, σ_r/σ_c	2	-	4
Coal angle of internal friction, ϕ	20		30
(Triaxial stress factor, k)	(2)	-	(3)
Pillar width, W in ft	20	30	50

$$k = \frac{1 + \sin \phi}{1 + \cos \phi}$$

Pillar height, H = 8 ft

To reduce the modeling time, the study will be conducted in two steps:

- Step 1- A screening analysis will be conducted for the first five factors listed in Table 6-1. Two levels, 1 and 3, full factorial design will be used in the screening analysis. The pillar width will not be considered in the screening analysis. A 30 ft-wide pillar will be used for the screening analysis. By this screening analysis we could eliminate one or two of the screened factors. The screening analysis will be conducted only for the development stage. The models descriptions and configurations are shown in Figure 4-1. The rock mechanics data used in these models are given in Tables 4-1 and 6-1.

- Step 2- Another full factorial analysis for the most important factors, defined by Step1 with additional levels, in addition to the pillar width will be conducted. This

analysis will consider the loading conditions of different stages of longwall retreats.

Running the full complement of all possible factor combinations means that we can estimate all the main and interaction effects. With a 2-level, five factors (2^5) full factorial design we can fit a model containing 5 main effects, 10 first-order interaction effects,10 second-order interaction effects, 5 third-order interaction effects and 1 fourth-order interaction effect (32 parameters including the intercept). However from an engineering viewpoint all third-order and higher interaction effects can be considered insignificant. Table 6-2 shows the design matrix for five factors and the calculated pillar stability measures.

A second order interaction regression model for 2^5 full factorial design is given by [Montgomery, 1997]:

$$y = b_0 + b_1 x_1 + b_2 x_2 + b_3 x_3 + b_4 x_4 + b_5 x_5$$
$$+ b_{12} x_1 x_2 + b_{13} x_1 x_3 + b_{14} x_1 x_4 + b_{15} x_1 x_5 + b_{23} x_2 x_3 + b_{24} x_2 x_4 + b_{25} x_2 x_5 + b_{34} x_3 x_4 + b_{35} x_3 x_5 + b_{45} x_5 x_5$$
$$+ b_{123} x_1 x_2 x_3 + b_{124} x_1 x_2 x_4 + b_{134} x_1 x_3 x_4 + b_{234} x_2 x_3 x_4 + b_{125} x_1 x_2 x_5 + b_{125} x_1 x_3 x_5 + b_{235} x_2 x_3 x_5$$
$$+ b_{145} x_1 x_4 x_5 + b_{245} x_2 x_4 x_5 + b_{345} x_3 x_4 x_5 + \varepsilon$$

Equation 6-9

where y is the model response; x_1, x_2, x_3, x_4 and x_4 are model variables; b's are regression coefficients; ε is the model error.

Stepwise regression is a technique for choosing the variables to include in a multiple regression model. Forward stepwise regression starts with no model terms. At each step it adds the most statistically significant term (the one with the highest F-statistic) until there are no more variables left [Netter, 1990]. This analysis is conducted using SAS [JMP 4 software, 2000].

An illustrative example will be presented to determine the significance of geometrical and geological parameters on the pillar yield ratio PYR of 30 ft-wide pillar during the development stage.

Response variable: Pillar Yield Ratio (PYR)

Model Factors: The model has five contributing factors: overburden depth, Z ft; roof/coal Young's modulus ratio, E_r/E_c; roof/coal uniaxial compressive strength ratio, σ_r/σ_c; shear limit of Coal/Rock interface, τ_{max} psi; and triaxial stress factor, k of coal.

The design matrix and the calculated PYR are listed in (Table 6-2).

Table 6-2 Design matrix for 2^5 full factorial analysis

Z, ft	E_r/E_c	σ_r/σ_c	τ_{max}, psi	k	CSF	PYR	PBI	RZR	RIF
1500	4	2	150	2	1.000	1.000	1.721	0.728	1.033
1500	4	2	150	3	1.021	0.761	1.045	0.361	0.743
1500	4	2	500	2	1.040	0.647	1.383	0.244	0.399
1500	4	2	500	3	1.213	0.317	0.510	0.094	0.260
2500	4	2	150	2	1.000	1.000	1.390	0.647	1.008
2500	4	2	150	3	1.000	1.000	1.056	0.875	1.400
2500	4	2	500	2	1.000	1.000	5.624	0.278	0.553
2500	4	2	500	3	1.072	0.600	2.999	0.269	0.607
1500	10	2	150	2	1.000	1.000	1.700	0.724	1.077
1500	10	2	150	3	1.020	0.756	1.112	0.366	0.884
1500	10	2	500	2	1.035	0.664	1.354	0.264	0.470
1500	10	2	500	3	1.205	0.317	0.525	0.094	0.301
2500	10	2	150	2	1.000	1.000	1.568	0.681	1.191
2500	10	2	150	3	1.000	1.000	1.183	0.875	1.548
2500	10	2	500	2	1.000	1.000	5.696	0.272	0.636
2500	10	2	500	3	1.071	0.597	2.646	0.316	0.788
1500	4	4	150	2	1.000	1.00	1.721	0.728	1.033
1500	4	4	150	3	1.021	0.76	1.045	0.361	0.743
1500	4	4	500	2	1.040	0.65	1.383	0.244	0.399
1500	4	4	500	3	1.213	0.32	0.510	0.094	0.260
2500	4	4	150	2	1.000	1.00	1.390	0.647	1.008
2500	4	4	150	3	1.000	1.00	1.056	0.875	1.400
2500	4	4	500	2	1.000	1.00	5.624	0.278	0.553
2500	4	4	500	3	1.072	0.60	2.998	0.269	0.607
1500	10	4	150	2	1.000	1.00	1.701	0.725	1.079
1500	10	4	150	3	1.020	0.76	1.111	0.367	0.885
1500	10	4	500	2	1.035	0.66	1.354	0.264	0.471
1500	10	4	500	3	1.205	0.32	0.525	0.094	0.301
2500	10	4	150	2	1.000	1.00	1.570	0.697	1.219
2500	10	4	150	3	1.000	1.00	1.184	0.900	1.593
2500	10	4	500	2	1.000	1.00	5.728	0.272	0.637
2500	10	4	500	3	1.071	0.60	2.554	0.317	0.790

After fitting the 26-term model of Equation (6-9), the following analysis (Table 6-3) is obtained.

Table 6-3 Output after fitting the 26-term model (Equation 6-1)

Summary of Fit

R-Square	0.999988
R-Square Adj	0.999938
Root Mean Square Error	0.001901
Mean of Response	0.791531
No. of Observations	32

Effect Tests

Source	F- Ratio
Z	2893.158
E_r/E_c	2.7210
σ_r/σ_c	0.0500
τ_{max}	5321.501
k	2886.245
Z x E_r/E_c	3.2379
Z x σ_r/σ_c	0.0673
Z x τ_{max}	12715.75
Z x k	3912.843
E_r/E_c x σ_r/σ_c	1.1362
E_r/E_c x τ_{max}	17.4675
E_r/E_c x k	6.5678
σ_r/σ_c x τ_{max}	0.0308
σ_r/σ_c x k	0.0164
τ_{max} x k	2354.482
Z x E_r/E_c x σ_r/σ_c	0.2161
Z x E_r/E_c x τ_{max}	10.5908
Z x σ_r/σ_c x τ_{max}	0.0086
E_r/E_c x σ_r/σ_c x τ_{max}	0.7003
Z x E_r/E_c x k	7.2709
Z x σ_r/σ_c x k	0.4236
E x σ_r/σ_c x k	1.9452
Z x τ_{max} x k	12846.93
E_r/E_c x τ_{max} x k	5.4035
σ_r/σ_c x τ_{max} x k	0.4236

Table 6-3 shows that the fit has a high R^2 and adjusted R^2, but the large number of small F Ratio indicates that the model has many unnecessary terms.

Starting with these 26 terms (including the intercept term), we next use the JMP Stepwise Regression option to eliminate unnecessary terms. By a combination of stepwise regression and the removal of remaining terms with a *p*-value higher than 0.05, we quickly arrive at a model with an intercept and 14 significant effect terms. Table 6-4 shows the output of fitting the 14-term model.

Table 6-4 Output after fitting the 14-parameter model

Summary of Fit

R-Square	0.999975
R-Square Adj	0.999954
Root Mean Square Error	0.001641
Mean of Response	0.791531
No. of Observations	32

Effect Tests

Source	F-Ratio
Z	8243.246
E_r/E_c	2.1273
τ_{max}	11725.18
k	8733.442
Z x E_r/E_c	4.3443
Z x τ_{max}	21969.2
Z x k	9885.889
E_r/E_c x τ_{max}	23.8812
E_r/E_c x k	6.2053
τ_{max} x k	4491.185
Z x E_r/E_c x τ_{max}	14.2150
Z x E_r/E_c x k	9.7590
Z x τ_{max} x k	17243.23
E x τ_{max} x k	7.2526

At this stage, this model appears to account for most of the variability in the response, achieving an adjusted R^2 of 0.9999. Only four of the main effects are significant, as are 6 first-order interactions and 4 second-order interaction.

Table 6-4 shows that σ_r/σ_c has no effect on the pillar yield ratio. To compare the effects of different terms on the pillar yield ratio, we should examine it in a more scale-invariant fashion. Hence; the unit effect can be ignored in the comparison. To do so, each factor will be scaled in a range -1 to 1. Figure 6-2 shows the scaled effects of the significant terms listed in Table 6-5. The positive scaled effect means that the studied factor is directly proportional for the investigated stability measure. Oppositely, the negative scaled effect means that the studied variable is inversely proportional to the stability measure. Figure 6-2 illustrates that interfacial shear stress limit τ_{max} is by far the most important factor. The coal triaxial stress factor k plays the next most critical role, followed by the overburden depth Z. There was no main effect for E_r/E_c on the PYR. The interaction Z x k has the lowest effect on the PYR.
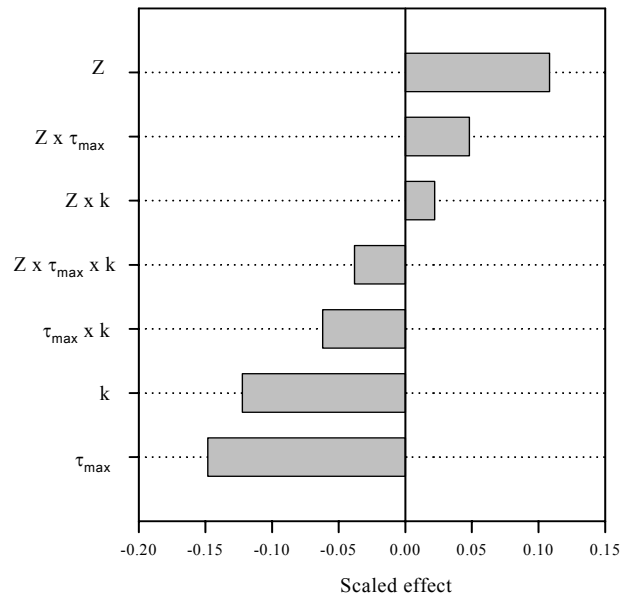
Figure 6-2 Scaled effect of geological and geometrical factors on the PYR

Similar to the above analysis, the effects of studied variables on the rest of the stability measures were conducted. Figures 6-3 shows the scaled effects of the studied factors on the PBI and RZR.
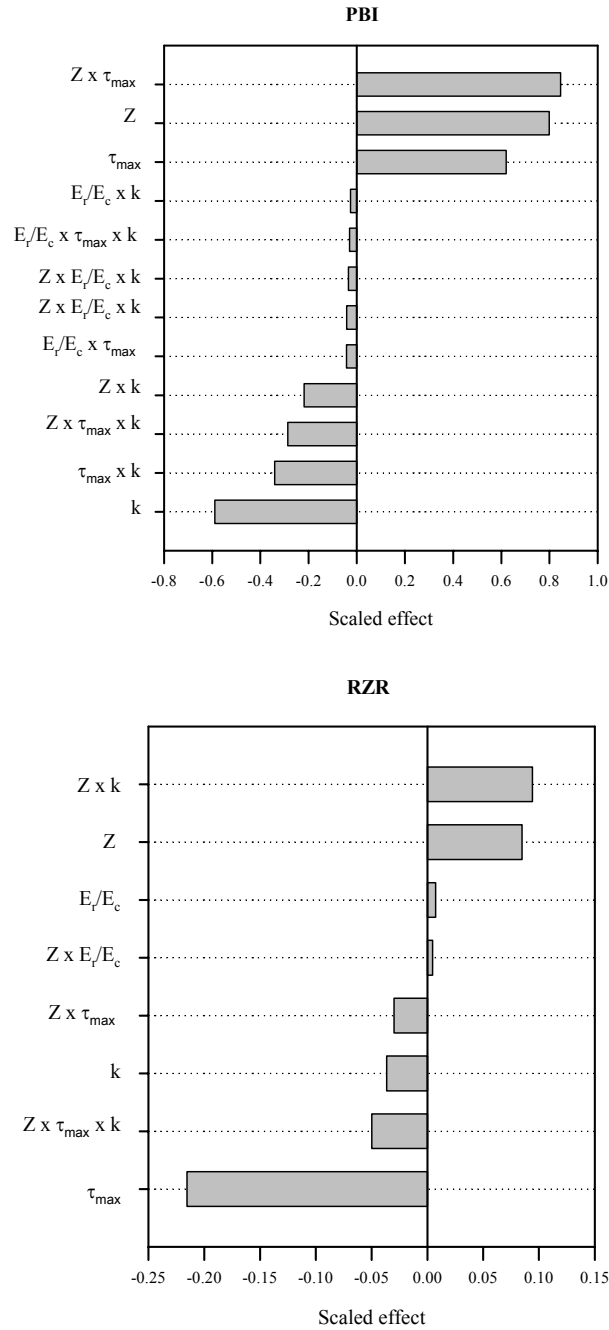
Figure 6-3 Scaled effect of geological and geometrical factors on PBI and RZR

At this stage of study, it would not be necessary to study how the screened factors affect the yield pillar stability measures. Figure 6-3 illustrates that the significance of a factor is highly related to the type of stability measure. For example the E_r/E_c has no effect on the PYR. It has its highest effect only on RZR. Also, the number and type of interactions depends on the type of stability measure. The PBI has the largest number of interactions which reflects the complexity of this stability measure. The effect of some factors was increased when it interacts with another factor. For example, the effect of overburden depth Z on the RZR was increased when it interacted with shear limit of coal/rock interface, τ_{max}. Figures 6-2 and 6-3 shows that third-order interaction effects still have effects on the yield pillar stability measures, for example; the Z x τ_{max} x k interaction has a significant effect on all the stability measures.

The screening analysis showed that the most influential factors that could affect the yield pillar stability are:

- Mining depth, Z;
- Shear limit of coal/rock interface, τ_{max};
- Rock-to-coal Young's modulus ratio, E_r/E_c;
- Friction angle of coal, ϕ, or triaxial stress factor, k.

6.3 Full Factorial Design for Finite Element Modeling

The previous discussions showed the pillar width is one of the most important factors. Table 6-1 shows the levels of the considered factors. A total of 108 three-dimensional FE models have to be conducted to consider the full factorial design for the factors. The full factorial combinations of these parameters and their levels are illustrated in Appendix A. The yield pillar stability has to be evaluated for different mining stages; i.e., development, panel retreat-1, panel retreat-2 and panel retreat-3. Appendix A illustrates the estimated stability measures for the full factorial combinations of the studied parameters.

Figure 6-4 shows the global models steps at the seam level. The global model considered 9 blocks of chain pillars, to reduce the boundary effects on the study area and to ensure the stress build up in the gob area. To reduce the model size the symmetry conditions was assumed at the middle of the panels. Therefore only half of the panels were considered. In addition to the geostatic step, the global model was solved in four steps; development, Retreat-1, Retrteat-2 and Retreat-3, Figure 6-4. Detailed simulation for the pillar at the T-junction, study area, was conducted by sub-modeling techniques for the same steps. The global models and sub-models were solved using the same finite element techniques described in Chapter 3.

Development

Panel Retreat-1

Panel Retreat-2

Panel Retreat-3
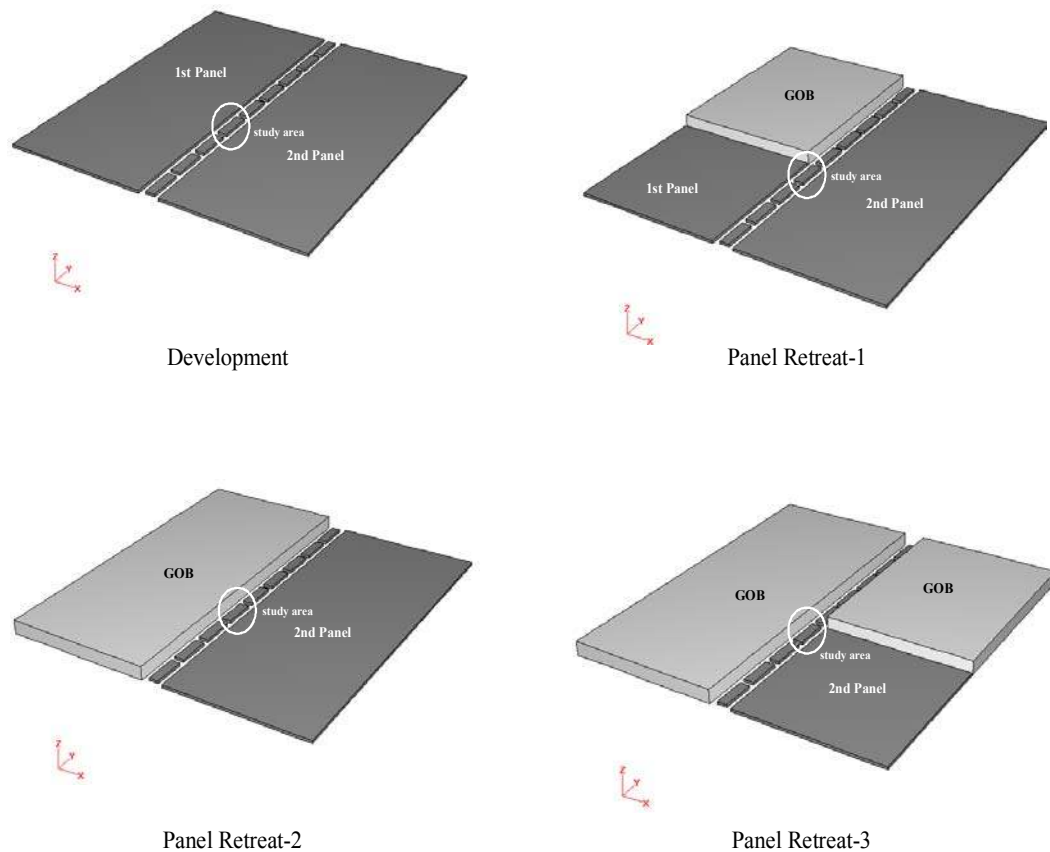
Figure 6-4 Steps of Finite Element modeling

6.4 Evaluation of Longwall Yield Pillar Stability Model (ELYPS-model)

The ELYPS-model is a Windows-based computer program that can evaluate and design yield pillar systems. The ELYPS-model is developed using MATLAB ver 6. It is based on an interpolation model and a suggested design algorithm for yield pillar systems.

Using the built-in interpolation functions of MATLAB ver 6, an interpolation model was developed. This interpolation model can predict the stability measures for any geological and geometrical combination within the ranges defined in Table 6-1. The stability measures estimated by FE models and the corresponding geological and geometrical factors were used as database for interpolation model.

ELYPS-model can carry out two main tasks:

I.   Evaluating an old project – to evaluate an old project, the user has to provide the following parameters:

1. Mining depth, Z in feet
2. Rock-to-coal Young's modulus ratio, E_r/E_c
3. Internal friction angle of coal, ϕ, in degrees
4. Shear limit of Coal/Rock interface, τ_{max} in psi
5. Pillar width, ft

II. Design a new project – to design a new project, i.e. to estimate the recommended pillar width, the user will be asked to provide the first four parameters listed above in addition to the following design criteria:

1. Allowable pillar bump index, PBI_a.
2. Allowable roof-to-floor convergence, AC_a in inches.

Snapshots for the ELYPS-model are illustrated in Appendix B. These snapshots illustrate model interfaces for both tasks; i.e. the evaluations and the design tasks.

CHAPTER 6   159

ELYPS-model is composed of a number of modules, Figure 6-5. The main modules are:

- **Interpolation module**

The interpolation module uses the established database of stability measures to predict the stability measures for any combination of geometrical and geological factors.

- **Design module**

The ELYPS-model designs the yield pillar based on two criteria:

1. The allowable pillar bump index, PBI_a; and
2. The allowable roof-to-floor convergence, C_a.

The ELYPS-model designs yield pillars to yield with acceptable levels of bump index (PBI) and roof-to-floor convergence (C). Therefore, the recommended yield pillar width is determined such that the pillar has a bump index and roof-to-floor convergence less than the allowable pillar bump index and the allowable roof to floor convergence; respectively. Figure 6-6 shows the design space of PBI_a and C_a. The design space is divided into $3^2 = 9$ zones. Each zone has a specific design algorithm to define the recommended yield pillar width.

For given geological and geometrical conditions, the interpolation module estimates the followings:

- The minimum and maximum bump index, PBI_min and PBI_max; respectively, for pillar widths ranged from 20 ft to 50 ft.

- The minimum and maximum roof-to-floor convergence, C_min and C_max; respectively, for pillar widths ranged from 20 ft to 50 ft.

Based on the estimated PBI_min, PBI_max, C_min, and C_max and the predefined PBI_a and C_a, the program chooses the appropriate design algorithm (Figure 6-6) to determine the recommended yield pillar width.

The gray zones in Figure 6-6 indicate that the program can define the recommended yield pillar width automatically. For any other zones, the user has to define the width of yield pillar based on the allowable pillar bump index, or the allowable roof-to-floor convergence. A more attention has to be given for the support plane if the users choose to design based on the allowable pillar bump index. But if he choose to design based on the allowable roof-to-floor convergence, a stress relief method maybe considered, see Chapter 2 for those methods.

To help the user for choosing between those two criteria the program provides the user with plots for the pillar width vs. the minimum pillar bump index and roof-to-floor convergence, see Appendix B for snapshots of these plots.
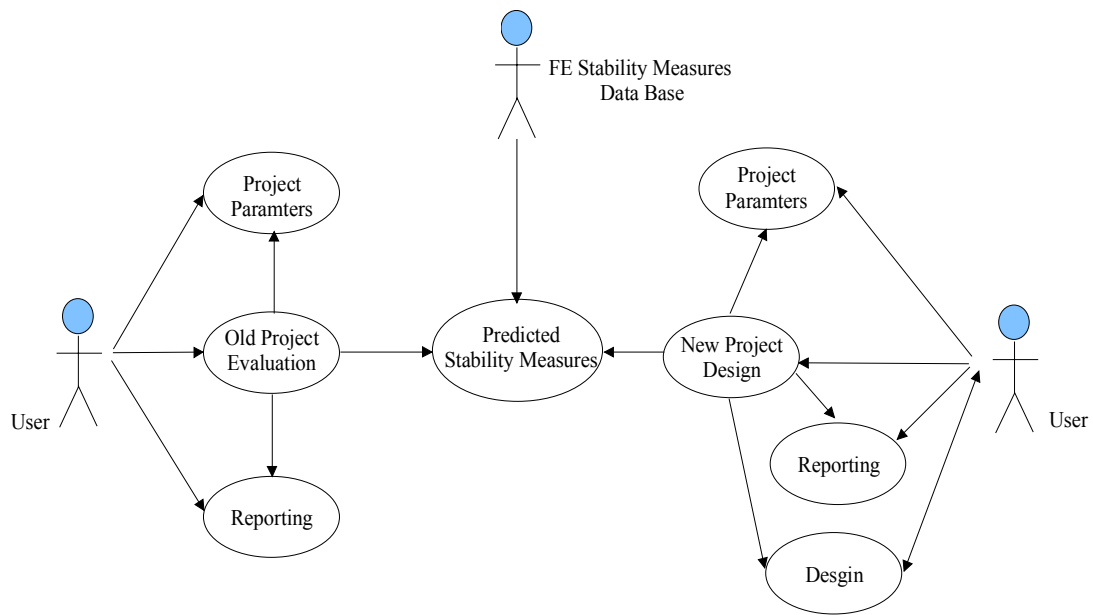
Figure 6-5 Use cases of ELYPS-model

Pillar Bump Index	$C\_a < C\_min$	$C\_min <= C\_a <= C\_max$	$C\_a > C\_max$
$PBI\_a > PBI\_max$	$W = W_{PBI\_min}$ OR $W = W_{C\_min}$	If $W_{PBI\_min} >= W_{c\_a}$ $W = W_{PBI\_min}$ Else $W = W_{c\_a}$	$W = W_{PBI\_min}$
$PBI\_min <= PBI\_a <= PBI\_max$	If $W_{PBI\_min} >= W_{PBI\_a}$ $W = W_{PBI\_min}$ Else $W = W_{PBI\_a}$ OR $W = W_{c\_min}$	If $W_{PBI\_min} <= W_{PBI\_a}$ & $W\_{PBI\_a} >= W\_{ca}$ $W = \max(W_{PBI\_min}, W\_{ca})$ Else $W = W_{PBI\_a}$ OR $W = W_{c\_a}$	If $W_{PBI\_min} >= W_{PBI\_a}$ $W = W_{PBI\_min}$ Else $W = W_{PBI\_a}$ OR $W = W_{c\_min}$
$PBI\_a < PBI\_min$	$W = W_{PBI\_min}$ OR $W = W_{c\_min}$	If $W_{PBI\_min} >= W_{c\_a}$ $W = W_{PBI\_min}$ Else $W = W_{PBI\_min}$ OR $W = W_{c\_a}$	$W = W_{PBI\_min}$ OR $W = W_{c\_min}$

Roof-to-floor Convergence

C_min = Minimum predicted roof-to-floor convergence at the headgate.
C_max = Maximum predicted roof-to-floor convergence at the headgate.
C_a = Allowable roof-to-floor convergence.
W_{c_min} = Estimated yield pillar width at C_min.
W_{c_a} = Estimated yield pillar width at C_a.
PBI_min = Minimum predicted pillar Bump Index through all stages of mining.
PBI_max = Maximum predicted pillar Bump Index through all stages of mining.
PBI_a = Allowable Pillar Bump Index.
W_{PBI_min} = Estimated yield pillar width at PBI_min.
W_{PBI_a} = Estimated yield pillar width at PBI_a.

Automatic decision.

User decision.

Figure 6-6 Design table foe ELYPS-model

6.5 Model Evaluation

The threshold values of pillar bump index and the roof-to-floor convergence can be determined by evaluating the ELYPS-model against large number of successful and unsuccessful cases. In this study, preliminary threshold values for the pillar bump index and the roof-to-floor convergence will be determined by estimating the PBI and C for three successful yield pillar design and one unsuccessful design associated with bump activities.

♦ **Mine A**

Mine A is located in Utah. There was two-seam mining in descending order. The upper seam is called Blind Canyon and the lower seam is called Hiawatha seam. A sandstone interburden of 80ft separates the upper and lower coal seams. The Blind Canyon seam is 7-10 ft thick with sandstone immediate roof and sandy shale immediate floor. The Hiawatha seam is 6.5-9.5 ft thick with shale immediate roof and sandstone immediate floor. The overburden ranges from 600 to 1600 ft with respect to the lower seam.

Currently, the mining operation is conducted in Hiawatha seam. Two-entry gateroad system of 30 ft x 80ft yield pillars is used for all panels regardless of cover depth and entry width. They never had any pillar bumps. Earlier instrumentation showed that the 30-ft pillar yield 3-ft deep upon development. To control the roof-to-floor convergence, two rows of 4-ft diameter concrete cans of varying length 6-9 ft were installed in staggered pattern in the future tailgate about 100 ft outby the face, Figure 6-7. The face experienced sloughage with different degrees. Near the tailgate, face sloughage with noise and "bangs" was frequent.

During the mine visit, it was observed that the shale immediate roof provided a little confinement to the pillar and a significant amount of pillar sloughing was observed in the top portions of coal pillar, as shown in Figure 6-8. Therefore, a moderate value of 325 psi was assigned for rock/coal interface shear limit.

Table 6-5 shows the evaluations results for Mine A estimated by ELYPS- model. The evaluation shows that during the development stage more than half of pillar volume is in elastic condition, (1-0.447 = 0.553). Based on the estimated RZR, a rib zone of 2.79 ft could be estimated at the pillar ribs. A small PBI was estimated during development stage. 33% of the pillar was considered as an elastic core during the Retreat-1. The highest PBI of 2.043 was estimated during Retreat-1. Because of low overburden depth, a small roof-to-floor convergence of 2.877" was estimated at the headgate.

Figure 6-7 Cans installed in the tailgate
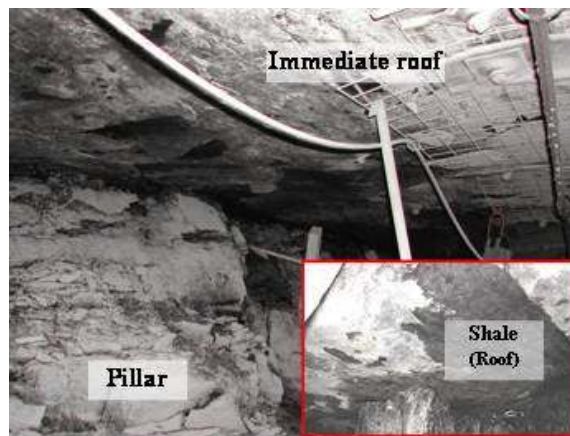
Figure 6-8 Significant pillar sloughing

Table 6-5 Design evaluation for Mine A

Yield Pillar Width, ft = 30
Overburden Depth, ft = 1600
Rock-to-Coal Young's modulus = 4
Internal friction angle of coal, degrees = 30
Shear limit of rock/coal interface, psi = 325

	Development	Retreat-1	Retreat-2	Retreat-3
Pillar Yield Ratio, PYR	0.447	0.669	1.000	1.000
Pillar Bump Index, PBI	0.762	2.043	1.522	1.268
Rib Zone Ratio, RZR	0.186			
Roof-to-floor Convergence, in				2.887

♦ **Mine B**

Mine B is located in Utah. The average mining height is 8 ft. The immediate roof is firm shale overlain by sandstone. In some areas sandstone was the immediate roof. Two-entry gateroad system is used in Mine B. The entry width is 20 ft wide and yield pillar is 29 ft wide by 100 ft long. Supplementary support in the tailgate was 2 rows of cans, 2-ft in diameter. The row of cans adjacent to the yield pillar is 7-ft from the pillar and that the row on the solid coal block is as close to the coal block as possible to prevent roof fall so during next panel mining it would be safe to travel. On the other hand it can not be too close for the shearer to cut and clear off the tail drive in the next panel. No significant pillar bumps were reported for Mine B.

During the mine visit, the mining operation was conducted in Panel 18. It was noticed that the first two yield pillars from the set-up room of Panel 18 did not have much sloughage. The sloughage increased in magnitude outby as it advanced further from the set-up room and also due to increasing cover depth. From 1500 to 2400 ft cover depth, the sloughed off debris although small in size filled up the spaced between pillar and meshes along the cans. The face location during the visit was at the 2400 ft cover location. Heavy pillar sloughage began one block inby. In the outby side, the affected

zone is only one block. Further outby, yield pillars show minor sloughage at mid-height and decreases with cover depth, Figure 6-9. Rib sloughage occurred in the solid coal block side also although in much smaller magnitude than the yield pillar side, mostly at mid-height and sometimes at the top along a coal/shale interface. At the cross-sections the yield pillars have an hour-glass shape because of the soft layer at the pillar mid-height, Figure 6-10. It was obvious that the pillar sloughage or pillar yielding depends very much on the nature and location of interfaces of soft layers making up the pillar.

Because of the firm contact between the coal pillar and the immediate roof, Figures 6-9 and 6-10, a high value of 500 psi was expected for rock/coal interface shear limit.
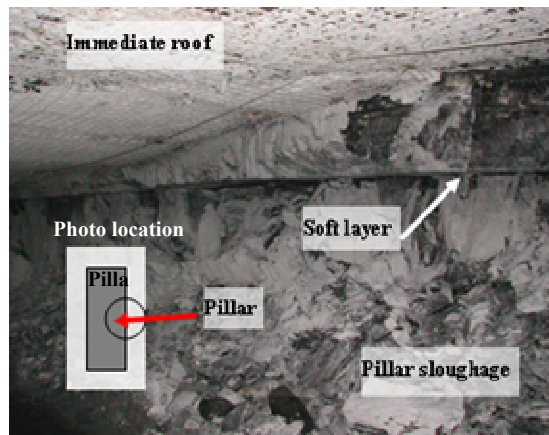
Figure 6-9 Rib sloughing

Table 6-6 shows the evaluations results for Mine B estimated by ELYPS- model. The evaluation shows that during the development stage less than half of pillar volume is in elastic condition, (1-0.601 = 0.399). Based on the estimated RZR, a rib zone of 3.7 ft could be estimated at the pillar ribs. Compared with Mine A, Mine B showed a relatively high PBI during development stage. The highest PBI of 4.610 was estimated during Retreat-1. Because of high overburden depth, a large roof-to-floor convergence of 4.339" was estimated at the headgate. Figures 6-9 and 6-10 show the immediate roof was intact.
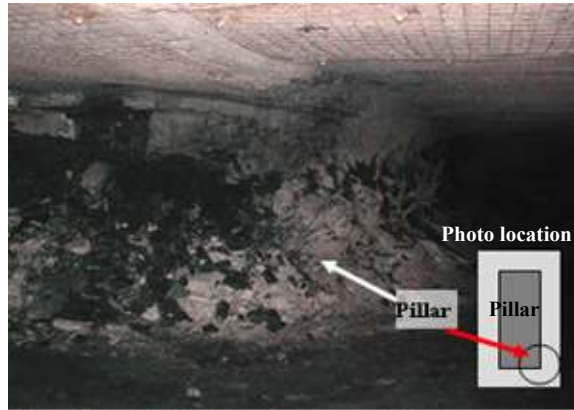
Figure 6-10 Hour-glass failure shape at the pillar's corner

Table 6-6 Design evaluation for Mine B

Yield Pillar Width, ft = 29

Overburden Depth, ft = 2400

Rock-to-Coal Young's modulus = 4

Internal friction angle of coal, degrees = 30

Shear limit of rock/coal interface, psi = 500

	Development	Retreat-1	Retreat-2	Retreat-3
Pillar Yield Ratio, PYR	0.601	0.777	1.000	1.000
Pillar Bump Index, PBI	2.772	4.610	2.306	1.953
Rib Zone Ratio, RZR	0.255			
Roof-to-floor Convergence, in				4.339

♦ **Mine C**

The Mine C is located in Utah. The mining operation is carried out in the Lower Sunnyside seam. The mining height is kept at 8 ft. The overburden depth ranges from 1000 to 2200 ft. The mining condition in Mine C is similar to that of Mine B. The

immediate roof is firm shale and immediate floor is hard sandstone. Two-entry gateroad system was employed in the Mine C. The belt entry width was 20 ft wide while the future tailgate was 18 ft wide. Yield pillars were 30 ft x 100 ft. Supplementary support in the tailgate was 2 rows of cans, 2-ft in diameter. No pillar bumps have been reported for mine C.

During the mine visit, it was observed that at 1000 ft deep cross cut, less than 1-2 ft fracture zone was developed at cross section ribs, Figure 6-11. The roof and floor were intact. For cross section at a depth of 2200 ft, the cross section ribs sloughed off very uneven and badly, Figure 6-12. A yielding zone of 4 ft was observed at pillar side. The block side sloughed off mostly on top but less severe than the pillar side. Because of the firm contact between the coal pillar and the immediate roof, Figures 6-11 and 6-12, a high value of 500 psi was expected for rock/coal interface shear limit.

Figure 6-11 Small rib fractures at 1000 ft deep

Table 6-7 shows the evaluations results for Mine C at different mining depths estimated by ELYPS-model. This case is very important where the effect of overburden depth can be investigated for the similar mining conditions. As expected smaller PYR and roof-to-floor convergence was estimated for smaller overburden depth.

During Retreat-2 and Retreat-3, the smaller PBI was estimated for larger overburden depth. During the development and Retreat-1, the smaller PBI was estimated

for smaller overburden depth. A smaller RZR was estimated for smaller overburden depth.

Figure 6-12 Rib's sloughing at 2200 ft deep

Table 6-7 Design evaluation for Mine C

Yield Pillar Width, ft = 30

Rock-to-Coal Young's modulus = 4

Internal friction angle of coal, degrees = 30

Shear limit of rock/coal interface, psi = 500

Overburden Depth, ft = 1500

	Development	Retreat-1	Retreat-2	Retreat-3
Pillar Yield Ratio, PYR	0.317	0.453	1.000	1.000
Pillar Bump Index, PBI	0.510	1.660	5.157	4.695
Rib Zone Ratio, RZR	0.094			
Roof-to-floor Convergence, in				2.746

Overburden Depth, ft = 2200

	Development	Retreat-1	Retreat-2	Retreat-3
Pillar Yield Ratio, PYR	0.538	0.696	1.000	1.000
Pillar Bump Index, PBI	2.079	3.763	2.770	2.476
Rib Zone Ratio, RZR	0.213			
Roof-to-floor Convergence, in				3.725

♦ **Sunnyside Mine**

A detailed description for Sunnyside mine was given in Chapter 5. Two sites were investigated in Sunnyside mine. Site 1 experienced a sever coal bump while Site 2 was stable. The pillar width and overburden depth of Site 1 were 55 ft and 2600 ft, respectively. Due to the interpolation limits of ELYPS-model, the pillar width and overburden depth of Site 1 were reduced to 55 ft and 2500 ft, respectively. Table 6-8 shows the evaluations results for Site 1 and Site 2 at different mining depths estimated by ELYPS-model. Site 1 shows larger pillar bump indices compared with Site 2.

Table 6-8 Design evaluation for Sunnyside Mine

Rock-to-Coal Young's modulus = 3.55

Internal friction angle of coal, degrees = 30

Site 1

Yield Pillar Width, ft = 50

Shear limit of rock/coal interface, psi = 500

Overburden Depth, ft = 2500

	Development	Retreat-1	Retreat-2	Retreat-3
Pillar Yield Ratio, PYR	1.196	0.525	1.000	1.000
Pillar Bump Index, PBI	0.398	3.630	7.376	6.206
Rib Zone Ratio, RZR	0.230			
Roof-to-floor Convergence, in				3.014

Site 2

Yield Pillar Width, ft = 40

Shear limit of rock/coal interface, psi = 150

Overburden Depth, ft = 1900

	Development	Retreat-1	Retreat-2	Retreat-3
Pillar Yield Ratio, PYR	1.009	0.992	1.000	1.000
Pillar Bump Index, PBI	0.921	1.716	0.393	0.351
Rib Zone Ratio, RZR	0.538			
Roof-to-floor Convergence, in				2.843

6.6 Summary

The screening analysis for the effects of geological and geometrical factors on the yield pillar stability showed:

♦ The overburden depth, shear limit of coal/rock interface, the triaxial stress factor of coal and the ratio of rock-to-coal Young's modules are the most significant factors.

♦ The effects of geological and geometrical factors on the yield pillar stability measures were very complicated. Therefore, the design of experiment techniques wouldn't be appropriate to consider all levels of interactions between the geological and geometrical factors on the yield pillar stability measures. Instead, a full factorial design is more suitable to consider the high levels of interactions among the geological and geometrical factors.

In addition to the outcomes of the screened factors, the pillar width was considered as a basic factor for the new design method of yield pillar systems. The design method was based on the estimation of four stability measures; i.e. yield pillar ratio, YPR, rib zone ratio, RZR, pillar bump index, PBI and roof-to-floor convergence.

A windows-based computer program, ELYPS-model, was established based on a proposed definition of yield pillar design and the developed interpolation model. The ELYPS-model model was used to evaluate three cases of stable yield pillar design in addition to the Sunnyside case presented in Chapter 5. Based on these evaluations a preliminary threshold values for the design criteria can be given: a value of 3 can be assigned for the allowable pillar bump index, while a value of 3-inches can assigned for the allowable roof-to-floor convergence. These figures can be changed in the future by investigating more accurate cases.

CHAPTER 7

CONCLUSIONS

A critical review of current methods of yield pillar design was conducted. The aim of this review was to explore their main features in order to avoid the repeat of weak points in the new proposed yield pillar design method. The followings are some of the main conclusions obtained from this review:

1. All the previous methods sized the yield pillars based on the conventional strength concept. Therefore none of them were able to evaluate the stability of yield pillars in the post-peak region. Unless the post-peak behavior of the yield pillars is included in the pillar design process, the risk of coal bumps is still possible.

2. An appropriate friction model to simulate the roof/floor coal pillar interface is crucial for any yield pillar design model.

3. Yield pillar system is a complex structure. The interactions among the geological and geometrical factors on the behavior of the pillar system are crucial. A full factorial analysis is the best choice to consider such interactions.

4. 3D finite element modeling is a necessity to simulate the complex loading condition of yield pillar systems.

A typical model for coal pillars, based on the in-situ and laboratory tests was proposed. The proposed model considered the effects of the width-to-height ratio and confining pressure on the deformation behaviors of coal pillar. This model can be used as a basic coal model in finite element applications. The linear Drucker-Prager model with mobilized angle of friction was found very successful to simulate the coal material.

A gob model based on Terzaghi's compaction model was developed to simulate the loading behavior of longwall gob material. The proposed technique does not require the division of the gob area into zones of different materials. Instead, one gob material is

prescribed for the whole gob area and the stiffness of gob material is updated automatically during the solution according to the state of stress. The proposed gob material shows the ability to transfer the abutment loads away from the face and chain pillar system towards the center of the gob area. In spite of the deviation of the model predictions from the in-situ measurements in some cases, it shows the same loading behavior. Further work needs to be done to study the effects of some parameters such as the gob height factor (gob height–to-seam height ratio), the overburden depth, the model dimensions, etc. on the performance of the gob model.

A new method for evaluating the stability of yield pillars was evaluated. The proposed method considers the non-homogeneity of yield pillar by dividing the yield pillar into three loading zones; namely core, transition and rib zone. An appropriate stability criterion was assigned for each loading zone. A case study of unsuccessful yield pillar design associated with coal bumps and another stable design was used to assess the proposed method. The proposed method successfully evaluated the stability of yield pillars in both designs. The evaluations elaborated some important features for the proposed method, such as:

1. The proposed coal model was able to show different stress-strain behaviors inside the pillar.
2. Based on the amount of confinement inside the pillar, the yield pillar could be divided to three loading zones; elastic core, transition and rib.
3. The size and stability of loading zones depend on the mining stage.

The screening analysis for the effects of geological and geometrical factors on the yield pillar stability showed:

1. The overburden depth, shear limit of coal/rock interface, the triaxial stress factor of coal and the ratio of rock-to-coal Young's modules are the most significant factors.

2. The geological and geometrical factors are highly interacted which means the usage of any design of experiment technique wouldn't be appropriate.

In addition to the outcomes of the screening analysis, the pillar width was considered as a basic factor in a new method for yield pillar design. The design method was based on the interpolation of four stability measures; i.e. yield pillar ratio, YPR, rib zone ratio, RZR, pillar bump index, PBI and roof-to-floor convergence, C.

A PC-program, ELYPS-model, was established based on the proposed definition of yield pillar and the developed interpolation model. The ELYPS-model model was used to evaluate three cases of stable yield and unstable pillar designs. Based on these evaluations preliminary threshold values for the allowable pillar bump index and roof-to-floor convergence, 3 and 3-inches, respectively, were proposed. These thresholds can be changed in the future by investigating more accurate cases.

APPENDIX A

Table A-1 Stability measures for different mining stages

Run #	Z, ft	$\frac{E_r}{E_c}$	W, ft	k	τ_{max}, psi	Development			*R-1		**R-2	***R-3
						PYR	PBI	RZR	PYR	PBI	PBI	PBI
1	1500	4	20	2	150	1.00	1.611	0.529	1.00	1.324	0.238	0.202
2	1500	4	20	3	150	0.95	1.252	0.446	1.00	1.417	0.237	0.201
3	1500	4	20	2	325	1.00	1.896	0.246	1.00	3.710	0.960	0.790
4	1500	4	20	3	325	0.55	1.366	0.204	0.93	2.250	0.931	0.769
5	1500	4	20	2	500	0.93	1.958	0.250	1.00	3.792	2.492	2.039
6	1500	4	20	3	500	0.47	0.839	0.158	0.86	2.104	2.370	1.876
7	1500	4	30	2	150	1.00	1.721	0.728	1.00	1.637	0.357	0.313
8	1500	4	30	3	150	0.76	1.045	0.361	1.00	1.953	0.356	0.311
9	1500	4	30	2	325	0.74	1.384	0.314	0.95	2.921	1.739	1.435
10	1500	4	30	3	325	0.39	0.619	0.147	0.61	1.732	1.633	1.358
11	1500	4	30	2	500	0.65	1.383	0.244	0.78	2.600	5.463	4.944
12	1500	4	30	3	500	0.32	0.510	0.094	0.45	1.660	5.157	4.695
13	1500	4	50	2	150	0.85	1.151	0.645	1.00	1.969	0.709	0.648
14	1500	4	50	3	150	0.56	0.858	0.263	0.80	1.490	0.682	0.624
15	1500	4	50	2	325	0.48	0.898	0.317	0.64	1.881	4.778	4.252
16	1500	4	50	3	325	0.24	0.382	0.087	0.39	1.178	4.525	4.012
17	1500	4	50	2	500	0.40	0.939	0.288	0.51	1.649	13.150	13.086
18	1500	4	50	3	500	0.20	0.316	0.057	0.28	1.066	10.526	11.102
19	1500	10	20	2	150	1.00	1.477	0.579	1.00	1.424	0.269	0.232
20	1500	10	20	3	150	0.98	1.295	0.458	1.00	1.573	0.268	0.231
21	1500	10	20	2	325	1.00	1.949	0.283	1.00	3.766	1.048	0.877
22	1500	10	20	3	325	0.55	0.827	0.213	0.83	2.266	1.015	0.853
23	1500	10	20	2	500	1.00	1.801	0.288	1.00	3.983	2.612	2.349
24	1500	10	20	3	500	0.47	0.849	0.158	0.64	2.102	2.476	2.248
25	1500	10	30	2	150	1.00	1.701	0.725	1.00	1.706	0.402	0.354
26	1500	10	30	3	150	0.76	1.111	0.367	1.00	2.017	0.399	0.352
27	1500	10	30	2	325	0.78	1.279	0.336	0.96	2.908	1.879	1.567
28	1500	10	30	3	325	0.40	0.583	0.150	0.60	1.706	1.752	1.473
29	1500	10	30	2	500	0.66	1.354	0.264	0.79	2.512	5.604	5.192
30	1500	10	30	3	500	0.32	0.525	0.094	0.45	1.625	5.239	4.892
31	1500	10	50	2	150	0.86	1.131	0.650	1.00	1.964	0.793	0.726
32	1500	10	50	3	150	0.56	0.914	0.277	0.78	1.464	0.757	0.695
33	1500	10	50	2	325	0.50	0.818	0.335	0.64	1.797	5.110	4.587
34	1500	10	50	3	325	0.23	0.354	0.090	0.38	1.158	4.799	4.295
35	1500	10	50	2	500	0.43	0.887	0.308	0.52	1.597	13.717	13.526
36	1500	10	50	3	500	0.21	0.304	0.062	0.27	1.002	10.172	11.005
37	2000	4	20	2	150	1.00	1.483	0.488	1.00	0.898	0.181	0.155
38	2000	4	20	3	150	1.00	1.419	0.775	1.00	0.761	0.174	0.149
39	2000	4	20	2	325	1.00	3.724	0.300	1.00	3.791	0.684	0.575

Run #	Z, ft	$\frac{E_r}{E_c}$	W, ft	k	τ_{max}, psi	Development			*R-1		**R-2	***R-3
						PYR	PBI	RZR	PYR	PBI	PBI	PBI
40	2000	4	20	3	325	0.83	2.351	0.417	1.00	4.200	0.678	0.571
41	2000	4	20	2	500	1.00	5.380	0.225	1.00	6.308	1.678	1.373
42	2000	4	20	3	500	0.66	1.862	0.254	1.00	3.944	1.638	1.346
43	2000	4	30	2	150	1.00	1.668	0.600	1.00	1.215	0.266	0.234
44	2000	4	30	3	150	1.00	2.000	0.667	1.00	1.136	0.260	0.228
45	2000	4	30	2	325	1.00	3.325	0.292	1.00	5.232	1.199	1.004
46	2000	4	30	3	325	0.64	1.548	0.314	0.85	3.293	1.163	0.978
47	2000	4	30	2	500	0.85	2.732	0.228	0.99	5.668	3.424	3.110
48	2000	4	30	3	500	0.49	1.549	0.178	0.63	3.085	3.235	2.967
49	2000	4	50	2	150	1.00	2.152	0.908	1.00	1.884	0.504	0.458
50	2000	4	50	3	150	0.89	1.698	0.560	1.00	2.216	0.504	0.457
51	2000	4	50	2	325	0.73	2.430	0.380	0.87	3.879	3.064	2.663
52	2000	4	50	3	325	0.41	1.121	0.380	0.59	2.536	2.845	2.491
53	2000	4	50	2	500	0.56	2.124	0.170	0.68	3.833	11.282	10.187
54	2000	4	50	3	500	0.28	0.930	0.117	0.40	2.034	11.127	9.901
55	2000	10	20	2	150	1.00	1.533	0.508	1.00	1.027	0.206	0.178
56	2000	10	20	3	150	1.00	1.505	0.829	1.00	0.873	0.198	0.172
57	2000	10	20	2	325	1.00	3.761	0.254	1.00	3.947	0.755	0.643
58	2000	10	20	3	325	0.86	2.214	0.442	1.00	4.276	0.747	0.637
59	2000	10	20	2	500	1.00	5.102	0.246	1.00	6.373	1.780	1.649
60	2000	10	20	3	500	0.67	1.894	0.267	0.85	4.141	1.742	1.619
61	2000	10	30	2	150	1.00	1.723	0.558	1.00	1.378	0.301	0.265
62	2000	10	30	3	150	1.00	2.057	0.686	1.00	1.298	0.294	0.260
63	2000	10	30	2	325	1.00	3.367	0.303	1.00	5.251	1.307	1.103
64	2000	10	30	3	325	0.64	1.559	0.322	0.84	3.317	1.265	1.071
65	2000	10	30	2	500	0.86	2.959	0.228	0.99	5.651	3.595	3.319
66	2000	10	30	3	500	0.48	1.552	0.183	0.63	3.054	3.377	3.147
67	2000	10	50	2	150	1.00	2.300	0.928	1.00	2.044	0.567	0.515
68	2000	10	50	3	150	0.88	1.681	0.572	1.00	2.482	0.565	0.514
69	2000	10	50	2	325	0.73	2.240	0.410	0.87	3.807	3.303	2.887
70	2000	10	50	3	325	0.41	1.077	0.257	0.58	2.453	3.068	2.693
71	2000	10	50	2	500	0.56	1.737	0.242	0.68	3.716	11.616	10.508
72	2000	10	50	3	500	0.28	0.958	0.142	0.39	1.952	11.434	10.243
73	2500	4	20	2	150	1.00	1.057	0.583	1.00	0.657	0.147	0.127
74	2500	4	20	3	150	1.00	0.793	0.904	1.00	0.546	0.140	0.121
75	2500	4	20	2	325	1.00	4.516	0.354	1.00	3.230	0.543	0.462
76	2500	4	20	3	325	1.00	3.864	0.475	1.00	3.185	0.531	0.452
77	2500	4	20	2	500	1.00	6.294	0.346	1.00	6.488	1.271	1.075
78	2500	4	20	3	500	0.84	4.436	0.308	0.99	6.247	1.257	1.065
79	2500	4	30	2	150	1.00	1.390	0.647	1.00	0.891	0.216	0.191
80	2500	4	30	3	150	1.00	1.056	0.875	1.00	0.727	0.204	0.181
81	2500	4	30	2	325	1.00	5.272	0.325	1.00	4.875	0.916	0.781

Table A-1 Stability measures for different mining stages, cont.

Run #	Z, ft	$\frac{E_r}{E_c}$	W, ft	k	τ_{max}, psi	Development			*R-1		**R-2	***R-3
						PYR	PBI	RZR	PYR	PBI	PBI	PBI
82	2500	4	30	3	325	0.84	3.008	0.414	0.95	4.879	0.905	0.772
83	2500	4	30	2	500	1.00	5.624	0.278	1.00	8.805	2.483	2.007
84	2500	4	30	3	500	0.60	2.998	0.269	0.78	4.897	2.397	1.953
85	2500	4	50	2	150	1.00	2.005	0.935	1.00	1.450	0.402	0.365
86	2500	4	50	3	150	1.00	2.089	0.867	1.00	1.278	0.383	0.349
87	2500	4	50	2	325	0.92	4.263	0.450	1.00	6.214	2.214	1.921
88	2500	4	50	3	325	0.60	2.410	0.357	0.77	4.018	2.118	1.846
89	2500	4	50	2	500	0.71	4.060	0.203	0.84	6.346	7.834	6.548
90	2500	4	50	3	500	0.40	1.592	0.230	0.53	3.630	7.376	6.206
91	2500	10	20	2	150	1.00	1.206	0.625	1.00	0.765	0.168	0.146
92	2500	10	20	3	150	1.00	0.901	0.958	1.00	0.631	0.160	0.139
93	2500	10	20	2	325	1.00	4.523	0.296	1.00	3.655	1.257	0.922
94	2500	10	20	3	325	1.00	3.739	0.554	1.00	3.462	0.735	0.604
95	2500	10	20	2	500	1.00	6.556	0.279	1.00	6.896	1.367	1.299
96	2500	10	20	3	500	0.81	3.860	0.404	1.00	6.726	1.350	1.284
97	2500	10	30	2	150	1.00	1.570	0.697	1.00	1.026	0.245	0.217
98	2500	10	30	3	150	1.00	1.184	0.900	1.00	0.834	0.231	0.206
99	2500	10	30	2	325	1.00	5.353	0.317	1.00	5.125	1.004	0.861
100	2500	10	30	3	325	0.83	3.028	0.494	1.00	5.000	0.991	0.850
101	2500	10	30	2	500	1.00	5.728	0.272	1.00	8.980	2.637	2.450
102	2500	10	30	3	500	0.60	2.554	0.317	0.79	4.974	2.534	2.369
103	2500	10	50	2	150	1.00	2.114	0.972	1.00	1.641	0.451	0.410
104	2500	10	50	3	150	1.00	2.387	0.852	1.00	1.475	0.433	0.395
105	2500	10	50	2	325	0.92	4.227	0.477	1.00	6.196	2.408	2.092
106	2500	10	50	3	325	0.60	2.421	0.370	0.76	4.038	2.298	2.002
107	2500	10	50	2	500	0.71	4.016	0.217	0.83	6.331	8.174	6.879
108	2500	10	50	3	500	0.40	1.591	0.237	0.52	3.638	7.698	6.517

Note:

    * Retreat -1
    ** Retreat -2
    *** Retreat -3
    The PYR values for panel Retreat 2 and 3 are equal to 1.

Table A-2 Roof-to-floor convergence for panel Retreat-3

Run #	Z, ft	W,ft	E_r/E_c	Roof-to-floor Convergence, C in
1	1500	20	4	5.399
2	2500	20	4	7.624
3	2000	20	4	6.579
4	2000	20	10	6.106
5	1500	20	10	4.985
6	2500	20	10	7.186
7	1500	30	4	2.746
8	2500	30	4	4.134
9	2000	30	4	3.452
10	2000	30	10	2.856
11	1500	30	10	2.254
12	2500	30	10	3.430
13	1500	50	4	1.935
14	2500	50	4	3.014
15	2000	50	4	2.486
16	2000	50	10	2.005
17	1500	50	10	1.555
18	2500	50	10	2.433

APPENDIX B

Snapshots for the ELYPS-model
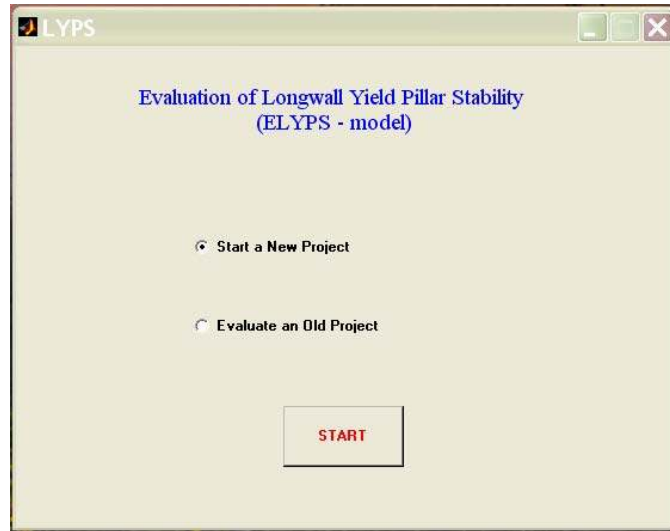
Figure C- 1 ELYPS-model starting interface
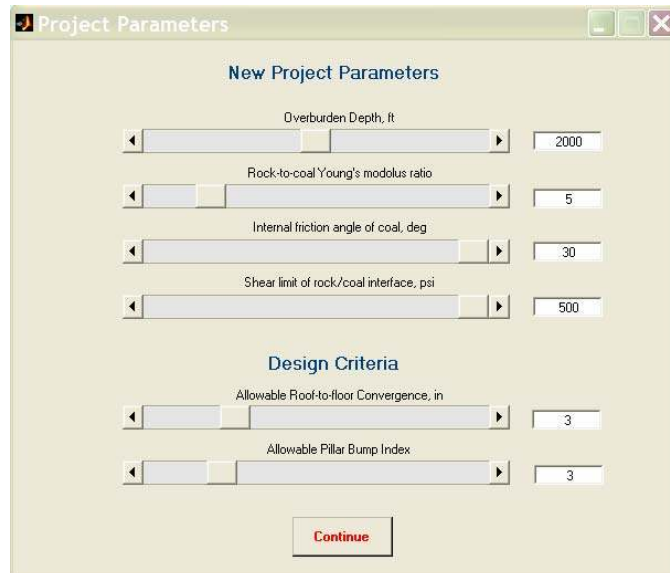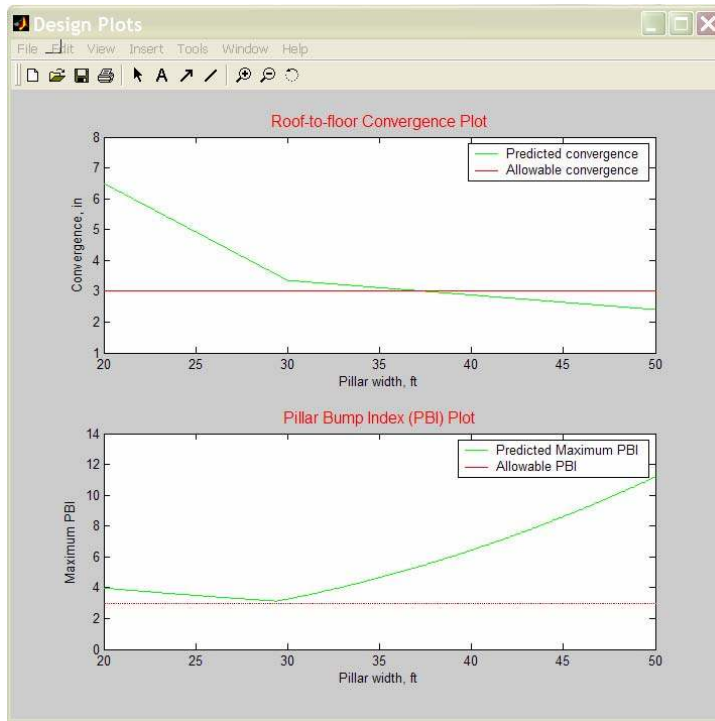

Figure C- 2 New project parameters interface

Figure C- 3 Design plots

Figure C- 4 Design report

REFERENCES

1. ABAQUS, 1998, *Standard User's Manual*, version 5.8.

2. Adachi, T. and Oka, F., 1985, "An Elasto-Plastic Constitutive Equation of Geological Materials," Proceedings of the 5th ICNMIG.Nagoya, pp. 293-300.

3. Adachi, T., Zhang, F., Oka, F., and Yashima A., 1991, "Finite Element Analyses with Strain-Softening Constitutive Model," *Computer Methods and Advances in Geomechanics*, Beer, Booker & Carter, pp. 535-540.

4. Babcock, C. O. and Bickel, D. L., 1984, "Constraint – The Missing Variable in The Coal Burst Problem," Proceedings of the 25th U.S. Symposium on Rock Mechanics, pp. 639-647.

5. Barron, K., 1992, "A Revised Model for Coal Pillars," Proceedings of the Workshop on Coal Pillar Mechanics and Design, US Bureau of Mines, IC 9315, pp. 144-157.

6. Barton, N., 1976, "The Shear Strength of Rock and Rock Joints," *Int., J. Rock Mech. Min. Sci. and Geom. Abs.*, vol. 13, pp. 255-279.

7. Bieniawski, Z.T., 1968, "The Effect of Specimen Size on Compressive Strength of Coal," *Int. J. of Rock Mech. and Mining Science,* vol. 5, pp. 325-535.

8. Bieniawski, Z.T., 1992, "A Method Revised: Coal Pillar Strength Formula Based on Field Investigations," Proceedings of the Workshop on Coal Pillar Mechanics and Design, US Bureau of Mines, IC 9315, pp. 158-165.

9. Brasfield, J., and Hendon, G. "Yield Pillar Behavior at Jim Walter No. 7 Mine Stress and Strata Measurements of Yield and Abutment Pillars," Proceedings of the 13th International Conference on Ground Control in Mining, WVU, Morgantown, WV, 1994, pp. 91-99.

10. Bräuner. G., 1994, *Rockbursts in Coal Mines and their Prevention*, A. A. Balkema, Rotterdam, Brookfield, 37 p.

11. Campoli, A. A., Barton, T. M., Dyke, F. C. V., and Gauna, M., 1990, "Mitigating Destuctive Longwall Bumps through Conventional Gate Entry Design," RI 9325, U.S. Bureau of Mines.

12. Campoli, A. A., Barton, T. M., Dyke, F. C. V., and Gauna, M., 1993, "Gob and Gate Road Reaction to Longwall Mining in Bump-Prone Strata," RI 9445, U.S. Bureau of Mines.

13. Carr, F., 1992, "Ten Year's Experience of Wilson/Carr Pillar Sizing Method at Jim Walter Resources Inc.," Proceedings of the Workshop on Coal Pillar Mechanics and Design, US Bureau of Mines, IC 9315, pp. 166-179.

14. Chen, G., 1989, *Investigation into Yield Pillar Behavior and Design Consideration*, Ph.D. Dissertation, Virginia Polytechnic Institute and state university.

15. Chen, R and Stimpson, B., 1997, "Simulation of Deformation and Fracturing in Potash Yield Pillars, Vanscoy, Saskatchewan," *Canadian Geotech., J.,* vol., 34, pp. 283-292.

16. Cox R. M., Conover, D. P., and McDonanell, J. P., 1995, "Integrated Shield and Pillar Monitoring Techniques for Detecting Catastrophic Failures," Proceedings in mechanics and mitigation of violent failure in coal and hard-rock mines, USBM Special Publication 01-95, pp. 119-140.

17. Crouch, S. L. and Fairhurst, C., 1973, "The Mechanics of Coal Mine Bumps," USBM, Contract No. H0101778.

18. Das, M. D., 1986, "Influence of Width/Height Ratio on Post-Failure Behavior of Coal," *International Journal of Mining and Geological Engineering*, Vol. 4, pp. 79-87.

19. DeMarco, M.J. 1994, "Yield Pillar Gateroad Design Considerations for Longwall Mining," Proceedings, USBM Technology Transfer Seminar, pp. 19-36.

20. DeMarco, M.J. 1996, "Critical Pillar Concept in Yield-Pillar-Based Longwall Gateroad Design," *Mining Engineering*, August, pp. 73-78.

21. DeMarco, M.J., Koehler and Maleki, H., 1995, "Gateroad Design Considerations for Mitigation of Coal Bumps in Western U.S. Longwall Operations," Proceedings in mechanics and mitigation of violent failure in coal and hard-rock mines, USBM special Publ. 01-95, pp. 141- 165.

22. Desai, C. S., and Siriwardane, H. J., 1984, *Constitutive Laws for Engineering Materials with Emphasis on Geologic Materials*, Prentice-Hall, Inc., Englewood Cliffs, New Jersey, 240 p.

23. DOE/EIA, 1995, "Longwall Mining," Department of Energy, Energy Information Administration, TR-0588, Distribution Category UC-950, pp. 39.

24. Farmer, I., 1983, *Engineering Behavior of Rocks*, Chapman and Hall, 2nd ed.

25. Gauna, M., Price, K. R., and Martin, E., 1985, "Yield Pillar Usage in Longwall Mining at deep, No. 4 Mine, Brookwood, Alabama," Proceedings of 26th US Symposium on Rock Mechanics, Rapid City, SD, June 26-28, pp. 695-702.

26. Hansen, J. B., 1965, "Some Stress-Strain Relationships for Soils," Proceedings of the 6th International Conference of Soil Mechanics and Foundation Engineering, Montreal, Vol. 1, pp. 231-234.

27. Haramy, K, Hanna, K., McDonnell, 1985, "Investigations of Underground Coal Mine Bursts," Proceedings of the 4th International Conference on Ground Control in Mining, WVU, Morgantown, WV, pp. 127-134.

28. Haramy, K., and Chen, G., 1988, "Computer Modeling of Yield Pillar Behavior using Post-Failure Criteria," Proceedings of the 7th International Conference on Ground Control in Mining WVU, Morgantown, WV, pp. 116-124.

29. Heasley, K. A., 1992, *Numerical Modeling of Coal Mines with Laminated Displacement Discontinuity Code*, Ph.D. Dissertation, Colorado School of Mines.

30. Heasley, K., 1999, personal communications.

31. Heerden, W. L. V., 1975, "In Situ Complete Stress-Strain Characteristics of Large Coal Specimens," *Journal of South African Institute of Mining and Metallurgy*, March, pp. 202-217.

32. Holland, C. T. and Thomas, E., 1954, "Coal Mine Bumps: Some Aspects of Occurrence, Cause and Control," USBM, Bull. 535, 1954.

33. Holland, C. T., 1941, "Physical Properties of Coal and Associated Rock as Related to Causes of Bumps in Coal Mines," *A. I. M. E., New York meeting*, pp. 75-93.

34. Holland, C. T., 1964, "The Strength of Coal in Mine Pillars," Proceedings of the 6th Symposium on Rock Mechanics. University of MO, Rolla, Mo, pp. 450-466.

35. Holland, C. T., and Gaddy, F. L., 1957, "Some Aspects of Permanent Support of Overburden on Coal Beds," Proceedings of West Virginia Coal Mining Institute, pp. 43-66.

36. Hsiung, S., 1984, *Structural design guidelines for longwall panel layout*, Ph.D. Dissertation, WVU, Morgantown, WV.

37. Hustrulid, W. A.,1976, "A Review of Coal Pillar Strength Formula," *Rock Mechanics,* vol. 8, pp. 115-145

38. Iannacchione, A. T., 1990, "The Effects of Roof and Floor Interface Slip on Coal Pillar Behavior," Proceedings of the 31st U.S. Sym. on Rock Mechanics, pp. 153-160.

39. Innacchione, A. T. and Zelanko, J. C., 1995, "Occurrence and Remediation of Coal Mine Bumps: A Historical Review," Proceedings in mechanics and mitigation of violent failure in coal and hard-rock mines, USBM Special Publication. 01-95, pp. 27-67.

40. JMP 4 software, 2000.

41. Karabin, G. J., and Evanto, M. A.,"Experience with The Boundary-Element Method of Numerical Modeling to Resolve Complex Ground Control Problems," Proceedings of the 2nd International Workshop on Coal Pillar Mech. and Design, NIOSH, IC 9448, 1999, pp. 89-113.

42. Khair, A. W., 1968, *Effect of Coefficient of Friction on the Compressive Strength of Model Coal Pillars*, M. Sc. Thesis, WVU, Morgantown, WV.

43. Kidybinski, A., 1981, "Bursting Liability Indices of Coal," *Int. J. Rock Mech. Min. Sci..*, vol. 18, pp. 295-304.

44. Ko, H., and Gerstle K. H., 1978, "Creep of Coal," Chapter in *Creep of Engineering Materials*, ed. by Pomeroy, C. D., Mechanical Engineering Publication Ltd., London, pp. 39-46.

45. Koehler, J. R. and DeMarco, M. J., 1995, "Comparative Case Study of Yielding and Critical Coal Pillar Design in Bump-Prone Strata," Proceedings of the 14th International Conference on Ground Control in Mining, WVU, Morgantown, WV, pp. 104-115.

46. Koehler, J. R., 1994, "The History of Gateroad Performance at The Sunnyside Mines: Summary of U.S. Bureau of Mines Field Notes," U.S. Bureau of Mines Information Circulation 9393, 43 pp.

47. Koehler, J. R., 1996, "Performance Evaluation 0f a Cable Bolted Yield-Abutment Gateroad System at The Crandall Canyon No.1, Genwall Resources, Inc., Huntington, UT.," 15th International Conference on Ground Control in Mining, CSM, Golden, CO

48. Maier, G. and Hueckel, T., 1979, "Nonassociated and Coupled Flow Rules of Elastoplasticity for Rock-like Materials," *Int. J. of Rock Mech. and Mining Sci.,* Vol. 16, pp. 77-92.

49. Maleki, H, Zahl, E. G., and Donford, P., 1999, "A Hybird Statistical-Analytical Method for Assessing Violent Failure in U.S. Coal Mines," Proceedings of 2nd International Workshop on Coal Pillar Mechanics and Design, NIOSH, IC 9448, pp. 181-192.

50. Maleki, H., 1995, "Analysis of Violent Failure in U.S. Coal mines: Case Studies," Proceedings in Mechanics and Mitigation of Violent Failure in Coal and Hard-Rock Mines, USBM special Publication 01-95, pp. 5-25.

51. Mark, C. and Barton, T., 1988, " Field Evaluation of Yield Pillar Systems at Kentucky Longwall Headgate," Proceedings of the 7th International Conference on Ground Control in Mining, WVU, Morgantown, WV, pp. 1-9

52. Mark, C., 1990, "Pillar Design Methods for Longwall Mining (ALPS)," US Bureau of Mines, IC 9247, pp. 1-53.

53. Martin, E., Carr, F., and Hendon G., 1988, "Strata Control at Jim Walter Resources, Mining Division," Proceedings of the 7th International Conference on Ground Control in Mining. WV U, Morgantown, WV, pp. 66-75.

54. Medhurst, T. P. and Brown, E. T., 1998, "A study of The Mechanical Behavior of Coal for Pillar Design," *International Journal of Rock Mechanics and Mining Science,* Vol. 35, No. 8, pp. 1087-1105.

55. Mogi, K., 1971, "Fracture and Flow of Rocks Under High Triaxial Compression," *J. of Geophysical Research,* Vol. 76, No. 5, pp. 1255-1269.

56. Montgomery, D., 1997, "Design and analysis of experiments," 5th edition

57. Mucho, T. P., 1986, "Roof Control Problems on Development and Longwall Gateroads at A Southwestern PA Coal Mine," Proceedings of the 5th International Conference on Ground Control in Mining WVU, Morgantown, WV, pp. 278-282.

58. Netter, K., Kutener, M., H., Nachtsheim, C., J., Wasserman, W., 1996, *Applied Linear Regression Models,* Richard D. Irwin, Inc., 3rd edition, 347 p.

59. Obert, L. and Duvall, W. I., 1967, *Rock Mechanics and The Design of Structures in Rock*, Wiley, New York, 542-545 p.

60. Oyanguren, P. R., "Simultaneous Extraction of Two Potash Beds in Close Proximity," Chapter 32 in Proceedings of the 5th International Strata Control conference, 1972, pp.5.

61. Ozbay, M. U., 1989, "The Stability and Design of Yield Pillars Located at Shallow and Moderate Depths," *Journal of South African Institute of Mining and Metallurgy*, March, pp. 73-79.

62. Pappas, D.M. and Mark, C., 1993, "Behavior of Simulated Longwall Gob Material," Bureau of Mines, RI 9458.

63. Patrick, W. C., 1982, "Direct shear strength of Appalachian coal", M. Sc. Thesis, WVU, Morgantown, WV.

64. Pen, Y. and Barron, K., 1994, "The Role of Local Mine Stiffness in Pillar Bump Prediction, " Proceedings of the 1st North American Rock Mechanics Symposium, University of Texas, Austin, pp. 1017-1025.

65. Pen, Y., 1994, *Chain Pillar Design in Longwall Mining for Bump-Prone Strata*, Ph.D. Dissertation, Edmonton, Alberta, Canada.

66. Peng, S., 1986, *Coal Mine Ground Control*, New York, NY, John Wiley & Sons, 14 pp.

67. Peng, S., Matsuki, K., and Su, W., 1980, "3-D Structural Analysis of Longwall Panels," Proceedings 21st U.S. Symp. On Rock Mech., University of Missouri Rolla, pp. 44-56.

68. Ray, R. E., Jr, 1987, "Determining The Optimum Number of Entries for Longwall Development Panels in Deep, Gassy Mines," Min. Eng., Littleton, CO., v. 39, No. 10, pp. 942-946.

69. Rice, G.S., 1934, "Bumps in Coal Mines of The Cumberland Field, Kentucky, Virginia – Causes and Remedy," USBM, Invest. 3267, 36 pp.

70. Ryder, J. A., and Wagner, H., 1978, "2D Analysis of Backfill as Means of Reducing Energy Release Rates at Depth," *Chamber of Mines of South Africa, Research Organization,* Research Report No. 47/78, pp. 22.

71. Salamon, M. D. G., 1990, "Mechanism of caving in longwall coal mining," Rock Mechanics Contributions and Challenges: Proceedings of the 31st U.S. Symp. of Rock Mechanics, Golden, Colorado, pp. 161-168.

72. Salamon, M. D. G., and Munro, A. H., 1967, "A Study of the Strength of Coal Pillars," *Journal of South African Institute of Mining and Metallurgy*, Vol. 68, pp. 55-67.

73. Salamon, M.D.G., 1970, "Stability, Instability and Design of Pillar Workings," *Int. J. Rock Mech. Min. Sci.,* vol.7, 1970, pp 613-631.

74. Salamon, M.D.G., 1974, "Rock Mechanics of Underground Excavations," Proceedings 3rd Congress of the International of Rock Mechanics, Denver, Colorado.

75. Serata, S., and Nakamura, T., 1985, "Finite Element Analysis of Stress Control Method," Proceedings of the 26th U.S. Symposium on Rock Mech., Rapid City, SD, vol. 26, pp. 659-666.

76. Skelly, W. A., Wolgamott, J., and Wang, F., 1977, "Coal Mine Pillar Strength and Deformation Prediction through Laboratory Sample Testing," Proceedings 18th Symposium on Rock Mechanics, Keystone, CO, Paper 2B5-1, 5 pp.

77. Starfield, A. M. and Fairhurst, C., 1968, "How High-Speed Computers Advance Design of Practical Mine Pillar Systems," Engineering & Mining Journal, vol. 169, pp. 78-84.

78. Starfield, A.M., and Wawersik, W. R., 1968, "Pillars as Structural Components in Room-and-Pillar Mine Design," Proceedings of 10th U.S. Symp. on rock mech., Rice Univ., AIME, New York, pp. 793-809.

79. Sun, G. C. and Peng, S. S., 1993, "Rock Mechanics Property Data Bank for Coal Measure Strata," Proceedings of 12th International Conference on Ground Control in Mining, Morgantown, WV, pp. 330-341.

80. Tadolini, S. C., and Haramy, K. Y., 1992, "Gateroads with Yield Pillars for Stress Control," 4th Conference on Ground Control for Midwestern U.S. coal mines, Southern Illinois University, IL, November, pp. 179-194

81. Trueman R., 1990, "A finite Element Analysis for the Establishment of Stress Development in Coal Mine Caved Waste," *Mining Sci. and Tech.,* No. 10, pp. 247-252

82. Tsang, P. and Peng, S., 1993, "A New Method For Longwall Pillar Design," Proceedings of the 12th International Conference on Ground Control in Mining, WVU, Morgantown, WV, pp. 261-273.

83. Tsang, P., 1992, "Yield Pillar Design for U.S. Longwall Mining," Ph. D. Dissertation, WV U, Morgantown, WV.

84. Unrug, K. and Szwilski, T., 1982, "Methods of Roof Cavability Prediction," Chapter 3 in State-of-the-Art of Ground Control in Longwall Mining and Mining Subsidence, SME, AIME, pp. 13.

85. Van Dillen, D. E., 1978, "Three-Dimensional Finite Element Analysis of Single– and-Double Entry Portions of Sunnyside Mine No. 1," Report No. R-7638-4534, submitted to U.S. Bureau of Mines, El Segundo, Ca, pp. 275.

86. Varley, F. D., 1986, "Outburst Control in Underground Coal Mines," Proceedings of the 5th International Conference on Ground Control in Mining, WVU, Morgantown, WV, pp. 249-256.

87. Wagner, H., 1974, "Determination of the Complete Load-Deformation Characteristics of Coal Pillars," Proceedings of the 3rd International Congress on Rock Mechanics, ISRM, Denver, CO, pp. 1076-1081.

88. Whittaker, B. N., 1974, "An Appraisal of Strata Control Practice," *Mining Engineer*, Vol. 134, pp. 9-24.

89. Whittaker, B.N. and Singh, R.N., 1979, "Evaluation of the Design Requirements and Performance of Gate Roadways," *Mining Engineer*, February, pp. 541-556.

90. Wilson, A. H. and Car, F., 1982, "A New Approach to the Design of Multi-Entry Developments for Retreat Longwall Mining," Proceedings of the 2nd International Conference on Ground Control in Mining. WVU, Morgantown, WV, pp. 1-21.

91. Wilson, A. H., 1977 "The effect of yield zone on the control of ground," 6th International Strata Control Conference, September, Banff Spring, Canada

92. Zingano, A., 2001, Personal communications.